THERMODYNAMIC PROPERTIES OF TRANSVERSE FIELD QUANTUM ISING MODEL USING TENSOR NETWORK FORMALISM

PANG SIN YANG

FACULTY OF SCIENCE
UNIVERSITI MALAYA
KUALA LUMPUR

2020

THERMODYNAMIC PROPERTIES OF TRANSVERSE FIELD QUANTUM ISING MODEL USING TENSOR NETWORK FORMALISM

PANG SIN YANG

DISSERTATION SUBMITTED IN FULFILMENT OF THE REQUIREMENTS FOR THE DEGREE OF MASTER OF SCIENCE

DEPARTMENT OF PHYSICS
FACULTY OF SCIENCE
UNIVERSITI MALAYA
KUALA LUMPUR

2020

UNIVERSITI MALAYA

ORIGINAL LITERARY WORK DECLARATION

Name of Candidate: **PANG SIN YANG**

Matric No: **SMA170043 (17013851/2)**

Name of Degree: **MASTER OF SCIENCE**

Title of Project Paper/Research Report/Dissertation/Thesis ("this Work"):

THERMODYNAMIC PROPERTIES OF TRANSVERSE FIELD QUANTUM ISING MODEL USING TENSOR NETWORK FORMALISM

Field of Study: **THEORETICAL PHYSICS**

I do solemnly and sincerely declare that:

(1) I am the sole author/writer of this Work;
(2) This Work is original;
(3) Any use of any work in which copyright exists was done by way of fair dealing and for permitted purposes and any excerpt or extract from, or reference to or reproduction of any copyright work has been disclosed expressly and sufficiently and the title of the Work and its authorship have been acknowledged in this Work;
(4) I do not have any actual knowledge nor do I ought reasonably to know that the making of this work constitutes an infringement of any copyright work;
(5) I hereby assign all and every rights in the copyright to this Work to the University of Malaya ("UM"), who henceforth shall be owner of the copyright in this Work and that any reproduction or use in any form or by any means whatsoever is prohibited without the written consent of UM having been first had and obtained;
(6) I am fully aware that if in the course of making this Work I have infringed any copyright whether intentionally or otherwise, I may be subject to legal action or any other action as may be determined by UM.

Candidate's Signature Date: 14 May 2020

Subscribed and solemnly declared before,

Witness's Signature Date: 14 May 2020

Name:

Designation:

THERMODYNAMIC PROPERTIES OF TRANSVERSE FIELD QUANTUM ISING MODEL USING TENSOR NETWORK FORMALISM

ABSTRACT

Ising model has been successful in describing ferromagnetism and its phase transition to paramagnet. At the critical point, the free energy density function and its derivatives diverge. Their behaviour near the critical point are described by power-laws with associated critical exponents. In many cases, the critical exponents can be determined from analytic solutions via conventional renormalization groups methods or from Monte Carlo simulations. However, for quantum many-body systems, very few are tractable to analytical solutions. The quantum many-body wavefunction belongs to large dimensional Hilbert space that increases exponentially with system size. If the Hamiltonian is gapped and only local interaction is considered, then the wavefunction can be efficiently truncated. Tensor Network formalism provides a scheme to truncate the less important degrees of freedom via Singular Value Decomposition (SVD) of the density matrix. In this study, we investigated the thermodynamic properties and phase transition of one-dimensional transverse-field quantum Ising model (1D-tQIM) under the finite-size effect and random coupling strength. Starting with Matrix Product States (MPS) as a wavefunction ansatz, the Density Matrix Renormalization Group algorithm is applied to the MPS. The variational algorithm, which iteratively performs SVDs and truncation at each bond, approximates the ground state MPS wavefunction. All quantum observables are calculated from the contraction of the resultant ground state MPS. Although theoretically, divergence at critical points only happen in an infinite system, one can obtain the critical exponents through simulation of finite-size 1D-tQIM. Using the analytic solution as a benchmark, we compared the finite-size effects of the system using finite-size scaling analysis and MPS methods. The critical exponents of 1D-tQIM are independently calculated and compared with the analytical results. Thermodynamic

quantities such as magnetization, susceptibility and correlation function are calculated for system sizes of 20, 40, 60, 80, 100 and 120 spins. We determined the respective critical exponents: $\beta/\nu = 0.1235(1)$, $\gamma/\nu = 1.7351(2)$, and $\eta = 0.249(1)$ and these agreed well with the theoretical values from analytical solutions and satisfied the hyperscaling relation. Next, we studied the effect of fluctuation on critical dynamics by introducing random coupling strength with uniform distribution (mean zero and amplitude ζ) as to mimic disordered quantum Ising model. Averages of thermodynamic quantities of 100 spins are calculated from 100 realizations for each transverse field reading. It is found that for fluctuation amplitude of $\zeta < 1$, the phase transition is initiated faster in comparison to the standard 1D-tQIM with uniform coupling strength. This feature is lost for $\zeta > 1$, and the system showed highly fluctuating behaviour similar to quantum spin glass. In conclusion, we showed that one-dimensional Tensor Network formalism in the form of Matrix Product States serves as useful approach to characterize critical dynamics and thermodynamic properties of quantum many-body systems with some constraints, such as finite-size and disordered 1D-tQIM. The numerical procedures described here can be extended to higher-dimensional tQIM and thus serve as theoretical models for understanding quantum many-body systems.

Keywords: Quantum Ising model, critical dynamics, Matrix Product States, finite-size scaling, noisy coupling

SIFAT-SIFAT TERMODINAMIK MODEL ISING KUANTUM MEDAN MELINTANG MENGGUNAKAN FORMALISME RANGKAIAN TENSOR

ABSTRAK

Ising model telah berjaya menjelaskan ferromagnetisme dan peralihan fasanya ke paramagnet. Pada titik kritikal, fungsi ketumpatan tenaga bebas dan hasil terbitannya mencapah. Tabiat mereka berhampiran titik kritikal diterangkan oleh hukum kuasa dan eksponen kritikal yang berkaitan. Dalam banyak kes, eksponen kritikal boleh ditentukan dari penyelesaian analitik melalui kaedah kumpulan renormalisasi konvensional atau dari simulasi Monte Carlo. Walau bagaimanapun, untuk sistem kuantum banyak jasad, sangat sedikit sistem yang boleh dikendalikan oleh penyelesaian analitik. Fungsi gelombang kuantum banyak jasad mempunyai dimensi ruang Hilbert besar yang membesar secara eksponen dengan saiz sistem. Sekiranya Hamiltonian mempunyai jurang dan hanya interaksi tempatan yang dipertimbangkan, maka fungsi gelombang dapat dikurangkan dengan cekap. Formalisme Rangkaian Tensor menyediakan skema untuk memangkas darjah kebebasan yang kurang penting melalui Penguraian Nilai Singular (SVD) bagi matriks ketumpatan. Dalam kajian ini, kita menyiasat sifat-sifat termodinamik dan fasa peralihan model Ising kuantum dengan medan melintang satu dimensi (1D-tQIM) di bawah kesan saiz terhingga dan kekuatan gandingan rawak. Bermula dengan Keadaan Produk Matriks (MPS) sebagai fungsi gelombang ansatz, algoritma Kumpulan Renormalisasi Matriks Ketumpatan digunakan ke atas MPS. Algoritma variasi, yang melakukan SVD secara berulang kali dan pemangkasan pada setiap ikatan, menghampiri keadaan asas bagi fungsi gelombang MPS. Semua kuantiti pemerhatian kuantum dikira dari penguncupan MPS keadaan asas yang dihasilkan. Walaupun secara teorinya, pencapahan di titik kritikal hanya berlaku dalam sistem tak terhingga, seseorang boleh memperolehi eksponen kritikal melalui simulasi saiz terhingga 1D-tQIM. Menggunakan penyelesaian analitik sebagai penanda aras, kami membandingkan kesan bersaiz

terhingga sistem dengan menggunakan analisis berskala saiz terhingga dan kaedah MPS. Eksponen kritikal 1D-tQIM dikira secara berasingan dan dibandingkan dengan hasil penyelesaian analitik. Kuantiti termodinamik seperti magnetisasi, kecenderungan magnet dan fungsi korelasi dikira untuk system bersaiz 20, 40, 60, 80, 100 dan 120 spin. Kami menentukan eksponen kritikal masing-masing: $\beta/\nu = 0.1235(1)$, $\gamma/\nu = 1.7351(2)$, dan $\eta = 0.249(1)$ dan nilai-nilai ini bersetuju dengan baik dengan nilai teori daripada penyelesaian analitik dan memenuhi hubungan hiperskaling. Seterusnya, kita mengkaji kesan turun naik dinamik kritikal dengan memperkenalkan kekuatan gandingan rawak dengan pengagihan seragam (min sifar dan amplitude ζ) untuk meniru model Ising kuantum yang tidak teratur. Purata kuantiti termodinamik sebanyak 100 spin dikira daripada 100 realisasi bagi setiap bacaan medan melintang. Bagi amplitud turun naik $\zeta < 1$, didapati peralihan fasa berlaku lebih cepat berbanding dengan 1D-tQIM yang standard dengan kekuatan gandingan seragam. Ciri ini hilang untuk $\zeta > 1$, dan sistem menunjukkan tingkah laku yang sangat tidak stabil, setara dengan sistem kaca spin kuantum. Sebagai kesimpulan, kami menunjukkan bahawa formalisme Rangkaian Tensor satu dimensi dalam bentuk Keadaan Produk Matriks berfungsi sebagai pendekatan yang berguna untuk mencirikan sifat dinamik kritikal dan termodinamik sistem kuantum banyak jasad dengan beberapa kekangan, seperti saiz terhingga dan 1D-tQIM yang tidak teratur. Prosedur berangka yang diterangkan di sini juga boleh diperluaskan kepada tQIM dimensi yang lebih tinggi dan dengan itu berfungsi sebagai model teori untuk memahami sistem kuantum banyak jasad.

Kata kunci: Model Ising kuantum, dinamik kritikal, Keadaan Produk Matriks, penskalaan saiz terhingga, gandingan rawak

ACKNOWLEDGEMENTS

First and foremost, I would like to thank my first supervisor Prof. Dr. Sithi Vinayakam Muniandy who introduced to me the wonderful field of tensor networks and the supervision of this Master project.

Next, I would like to thank my second supervisor, Dr. Mohd Zahurin bin Mohamed Kamali who has always by my side, accompanying me throughout my studies. Thank you very much for the advices given and "minum dan bincang" sessions we had together.

I would like to thank my dear senior Cik Nur Izzati binti Ishak for the guidance and support whose experience proves to be invaluable in avoiding potholes on my journey of master's degree.

Also, in utmost respect and solemnity, I express my sincerest gratitude to the President of Soka Gakkai International, Mr. Daisaku Ikeda for his guidance and encouragements through the New Human Revolution novel series that empowered me throughout the stagnant stages of my life.

In addition, I would also like to thank my friends from other fields of research within the Department of Physics for their warm support and companionship. They are Chong Wen Sin, Gan Soon Xin, Chew Jing Wen and Ng Kok Bin from the Photonics Research Center, Lee Hong Chun and Lau Yen Theng from the Plasma Technology Research Center, and Ng Zhan Hao from the cosmology research group. Also, special thanks to anyone who had lent their ears for my complains and grumbling, sharing my concerns throughout my postgraduate studies.

I am grateful to the Malaysian Ministry of Higher Education (MOHE) for the Skim Biasiswa MyBrainSc scholarship to enable me to pursue postgraduate research in the field of Statistical Physics and Quantum Dynamics at the Center for Theoretical and

Computational Physics, supported by MOHE's Fundamental Research Grant Scheme (FP031-2017A) and the University of Malaya Frontier Research Grant (FG032-17AFR).

Last but most importantly, my parents Pang Yat Huah and Loo Youk Looi, without whom I will not be able to pursue my master without worry. Finally, I would like to express my gratitude to everyone who has directly or indirectly lent their hands in this endeavour.

TABLE OF CONTENTS

LIST OF FIGURES

LIST OF TABLES

LIST OF SYMBOLS & ABBREVIATIONS

J	:	Coupling strength of nearest neighbour interaction
B_z	:	Longitudinal magnetic field
h	:	Transverse magnetic field
ϵ	:	Reduced transverse magnetic field
h_c	:	Critical transverse field
T	:	Temperature
t	:	Reduced temperature
T_c	:	Critical temperature
C	:	Specific heat
S	:	Boltzmann entropy
M	:	Spontaneous magnetization
χ	:	Magnetic susceptibility
Q	:	Partition function
k_B	:	Boltzmann constant
G	:	Two-point correlation function
ξ	:	Correlation length
d	:	Dimension of the system
α	:	Specific heat critical exponent
β	:	Magnetization critical exponent
γ	:	Magnetic susceptibility critical exponent
ν	:	Correlation length critical exponent
η	:	Anomalous critical exponent
δ	:	Critical isotherm critical exponent
z	:	Dynamical critical exponent

S^z	:	Classical spin-z variable
S^x	:	Classical spin-x variable
$\hat{S}^z$	:	Quantum spin-z operator
$\hat{S}^x$	:	Quantum spin-x operator
$\hbar$	:	Reduced Planck's constant
p	:	Dimension of local state space
χ	:	Dimension of singular value matrix $\mathbf{\Lambda}$
D	:	Bond dimension
λ_i	:	Schmidt coefficient / singular value
S_{vN}	:	Von Neumann entropy
m	:	Number of eigenstates kept
L	:	Size of the system (number of spins)
σ_i	:	Site index of site i
a_i	:	Bond index of Matrix Product States between site i and $i+1$
b_i	:	Bond index of Matrix Product Operator between site i and $i+1$
ρ_L	:	Density matrix of system size L
H	:	Hamiltonian
E_0	:	Ground state energy
U_L	:	Binder's cumulant
ε_i	:	Fluctuation of coupling strength at site i
ζ	:	Noise amplitude
q	:	Edward-Anderson order parameter
ϑ	:	Degree of homogeneity
DMRG	:	Density Matrix Renormalization Group
FSS	:	Finite Size Scaling

iDMRG	:	Infinite Density Matrix Renormalization Group
MPS	:	Matrix Product States
MPO	:	Matrix Product Operator
MERA	:	Multiscale Entanglement Renormalization Ansatz
NRG	:	Numerical Renormalization Group
OBC	:	Open boundary condition
PBC	:	Periodic boundary condition
PEPS	:	Projected Entangled Pair States
r.m.s.	:	Root-mean-square
SVD	:	Singular Value Decomposition
tQIM	:	Transverse-field Quantum Ising Model
TTN	:	Tree Tensor Network

LIST OF APPENDICES

CHAPTER 1: INTRODUCTION

1.1 Quantum Many-body Systems

The advances of quantum physics allow us to study materials beyond the ordinary phases of matter, which are the solid, liquid and gas phases. These ordinary phases exist in a thermal environment, while near the absolute zero, other phases of matter such as the Bose-Einstein condensates, superfluids, quantum spin liquids, and superconducting phase can exist. The Bose-Einstein condensates (BEC) are formed by cooling gas of Bosons until it achieves highly condensed states near the absolute zero (Demokritov et. al., 2006; Klaers et. al., 2010). It is a generic phase of matter which serves as a crucial mechanism to explain other quantum phenomena such as superfluidity and superconductivity. The superfluid, which consists of Helium isotopes such as He-3 or He-4, is a phase with zero viscosity. This enables the fluid to flow without any loss of kinetic energy. It is an example of Bose-Einstein condensates where the isotopes form fermionic condensates (Cooper pair from two He-3 atoms) to achieve the superfluidity phase (Bogoliubov, 1947; Leggett, 1999). Similarly, for a superconductor, the electron Cooper pairs form within the conductor below a critical temperature and result in a conductor with null resistance (Bardeen et. al., 1957; Li et. al., 2014; Linder & Robinson, 2015). Quantum spin liquids, on the other hand, consists of quantum spins with frustrated interactions, form "liquid" of disordered spins with long-range entanglements and topological order (Wen, 2004; Misguich, 2005; Savary & Balents, 2017). These phases of matter do not break any symmetry and cannot be characterized by a fixed order parameter. In addition, there is the deconfined quantum criticality (Senthil et. al, 2004a; Senthil et. al, 2004b), such that phases separated by the quantum critical points has fundamentally different symmetries. For these ultracold systems, the quantum effects are dominant and the rules of quantum mechanics must be fully applied. The studies of these systems are collectively known as the quantum many-body systems.

The main challenge to study these phases of matter is that they cannot be understood within the Landau's paradigm of phase transitions where a single order parameter characterizes the phase transition of the system. To truly study these quantum many-body problems, the quantum entanglement must be fully accounted for. White proposed the Density Matrix Renormalization Group (DMRG) algorithm (White 1992; White, 1993) which is the first numerical approach that selects the most optimally entangled eigenstates with respect to the ground state of one-dimensional quantum lattice model. The DMRG produces wavefunction in the form of product of matrices known as the Matrix Product States (MPS), which makes the correlation or equivalently the quantum entanglement between the spins explicit. For short-ranged systems, the MPS is described by a number of parameters that scale with its system size only, contrary to exponentially large Hilbert space in generic wavefunction. The generalization of the DMRG and MPS to higher dimension extends the methods into the tensor network formalism. Whenever the system's interactions are sufficiently short-ranged and has a gap between its ground state and first excited state, the quantum wavefunction can be represented as a tensor network, whose number of parameters scales only polynomially with system size, and efficiently truncate less entangled eigenstates that are insignificant to the ground state. The tensor network has slowly evolved to become a standard formalism in the study of all quantum phenomena, even as a possible new framework for quantum field theory by generalizing the discrete tensors into continuous parameters (Verstraete & Cirac, 2010; Jennings, et. al., 2015; Haegeman, et. al., 2013).

The tQIM and its variants such as the spin-1 Blume-Capel model, the mixed-spin Ising model or the anisotropic next-nearest-neighbour Ising (ANNNI) model are an important class of solvable and well-understood models in the quantum many-body problems (Strecka & Jascur, 2015; Suzuki et. al., 2012). Besides as a benchmark for various numerical approach for quantum lattice systems and as a framework for various

optimization problems (Fischer & Hertz, 1993), they have wide applications. Especially with the recent advances in optical and magnetic traps (Gross & Bloch, 2017; Dreon, 2017; La Rooij, 2019), the theoretical insights of these lattice models are directly testable and applied to the Ising machines (Inagaki et. al., 2016; McMahon et. al., 2016) for combinatorial optimization problems such as travelling salesman problem, quantum computation and quantum information processing (Farhi et. al, 2000; Farhi et. al., 2001), and many other quantum optimizations and machine learning problems (Inoue, 2001; Venturelli et. al., 2015). In the advent of quantum computing and algorithms, the tQIM also becomes a standard model to study dynamical quantum processes such as quantum quenches (Sengupta et. al., 2004; Calabrese & Cardy, 2006; Rossini et. al., 2009), quantum annealing (Kadowaki & Nishimori, 1998; de Falco & Tamascelli, 2011) and quantum error correction codes (Jouzdani et. al., 2014).

1.2 Motivation of Study

The one-dimensional tQIM is chosen as the system of study because it is exactly solvable (Pfeuty, 1970) and at the same time a generic framework for optimizations and quantum information processing. As the tensor network formalism is becoming increasingly prominent, we are interested to apply it to the 1D tQIM to compare its properties with the analytic solutions. If the tensor network techniques agree well with the analytical solutions, one can confidently apply the said techniques to investigate the effect of fluctuations, which is the fundamental obstacles of implementing quantum algorithms and computation, on the phase transition and thermodynamic properties of tQIM.

1.3 Objectives

In this numerical study, the 1D tensor network, the Matrix Product States (MPS) formalism will be used to study some interesting thermodynamics properties of the 1D tQIM under different generalizations. The objectives of this study are

i. to benchmark the Matrix Product States formalism with the analytic solution of quantum Ising model.
ii. to study the finite-size effects and obtain the critical exponents of the quantum Ising model using the Matrix Product States formalism and finite-size scaling analysis.
iii. to determine the effect of fluctuations on the thermodynamic parameters and order-disorder phase transition of the quantum Ising model.

1.4 Thesis Layout

Following the introduction in Chapter 1, the phase transitions and critical phenomena of the Ising model are briefly reviewed in Chapter 2. The general tensor network formalism, examples of tensor networks and recent developments are introduced. In Chapter 3, we introduce the MPS formalism, the DMRG, its traditional and modern algorithms, and the finite-size scaling theory as the methodology of study. In Chapter 4 the results of numerical calculations of 1D tQIM are presented and compared with the analytic solution. The critical exponents are determined from finite-size scaling analysis. The effect of fluctuations on the thermodynamic parameters and phase transition of 1D tQIM is reported and discussed. Lastly the conclusion and suggestions for future work are given in Chapter 5. An interesting application of the study on water-ice phase transition of single-file water in nanopores is proposed.

CHAPTER 2: LITERATURE REVIEW

In this chapter, we briefly review the concepts of phase transition and critical phenomena based on the classical Ising model, before introducing the quantum Ising model and its one-dimensional analytic solution. The tensor network formalism for quantum wavefunction approximation and calculations are described as the main theoretical formalism. Examples including the Matrix Product States (MPS), a 1D tensor network, the Projected Entangled Pair States (PEPS), a 2D version of MPS, and other recent developments of the formalism are introduced.

2.1 Phase Transition and the Ising Model

Matters exist in various phases characterized by thermodynamic parameters such as the vapour pressure for the liquid-gas phase or the spontaneous magnetization for magnetic materials. A statistical quantity called the order parameter summarizes the aggregate behaviour of the system and serves as an indicator of the phase. For example, the magnetic phase transition from paramagnetic to ferromagnetic phase, the order parameter is the zero-field magnetization M. In the absence of an external field, magnetic spins in a paramagnet are randomly aligned and thus have zero net magnetization. However, when one lowers the temperature of the material, the neighbouring spins start to align in a certain direction and forming domains, where each has net magnetization in one direction. These "macro" magnetic dipoles sum up their magnetization and form strong resultant magnetic field. The material is said to have undergone phase transition to ferromagnetic phase. To further illustrate the theory of phase transition, let us look at the Ising model, which consists of spins represented as arrows, each has only 2 degrees of freedom (pointing up or down), arranged in a regular lattice. Two neighbouring spins interact with each other via a coupling term in the Hamiltonian. The Hamiltonian of generic Ising model is given as follows:

$$H = -J \sum_{<i,j>} S_i^z S_j^z - B_z \sum_k S_k^z \quad (2.1)$$

where S_i^z is the i-th spin along the z-axis, J is the coupling strength, B_z is the longitudinal magnetic field and $\Sigma_{<i,j>}$ is the sum over all nearest neighbour spins. The coupling strength is dependant on the temperature of the system and by decreasing the temperature, one tunes the spins to align. As the temperature lowers, the system with zero net magnetization will come across a point where the order parameter suddenly increases with a steep gradient and has a non-zero value. This point is called the critical point where many interesting phenomena of phase transition is studied.

For classical many-body systems, the macroscopic quantities such as the specific heat C, entropy S, magnetization M, and magnetic susceptibility χ are derivatives of the partition function $Q(B_z, T)$, a function which encodes the distribution of all possible configurational states of the system. The partition function, which is a function of longitudinal field and temperature for the Ising model, is defined as:

$$Q(B_z, T) = \sum_i \exp\left(-\frac{H_i}{k_B T}\right) \quad (2.2)$$

where the sum is over all possible configurations and k_B is the Boltzmann constant. The specific heat of a ferromagnet is given by:

$$C(B_z, T) = k_B \tau^2 \frac{\partial^2}{\partial \tau^2} [\ln Q(B_z, T)] \quad (2.3)$$

where $\tau = 1/k_B T$. The magnetization is given by:

$$M(B_z, T) = \frac{\partial}{\partial B_z} [\ln Q(B_z, T)] \quad (2.4)$$

The 1D Ising model is shown to have no phase transition to an ordered ferromagnetic phase (Ising, 1925). However, it is incorrectly concluded that the model has no phase transition for higher dimensions. Bragg and Williams further improved the model by introducing a mean-field approximation to account for the collective magnetic effect on one spin by all other spins (Bragg & Williams, 1934; Williams, 1935). Bethe improved

Bragg & Williams approximation by including the thermal fluctuation. While the result of no phase transition for 1D is obtained, Bethe showed that there are phase transitions for 2D and 3D (Bethe, 1935). Around the same time, Peierls showed 2D and 3D Ising model has a phase transition at low temperature (Peierls, 1936). In 1941, Kramers and Wannier obtain the Curie temperature for the 2D Ising model and showed that the partition function Q is related to the largest eigenvalue of a certain matrix (Kramers & Wannier, 1941). In 1942, Lars Onsager successfully solved the 2D Ising model in zero magnetic field analytically (Onsager, 1944). The partition function is obtained as follows:

$$\lim_{N\to\infty} \ln Q(B_z = 0, T) = \ln 2 \cosh(2\beta J) + \int_0^{\pi} d\phi \left[\ln \tfrac{1}{2}\left(1 + \sqrt{1 - \kappa^2 \sin^2\phi}\right)\right] \tag{2.5}$$

where $\kappa \equiv 2\sinh(2\beta J)/\cosh^2(2\beta J)$. Kaufman (Kaufman, 1949) and Newell and Montroll (Newell & Montroll, 1953) further simplified Onsager's method with ideas from spinors theory and Lie algebra respectively. Newell and Montroll obtained the partition function for any $n \times m$ rectangular lattice in the form:

$$\lim_{n,m\to\infty} \frac{\ln Q(B_z=0,T)}{mn} = \ln 2 + \int_0^{\pi} d\omega \int_0^{\pi} d\omega' \left[\ln(\cosh 2K \cosh 2K' - \sinh 2K \cos\omega - \sinh 2K' \cos\omega')\right] \tag{2.6}$$

where $K = J/k_B T$ and $K' = J'/k_B T$ while J and J' are interactions of vertical and horizontal interactions. In principle, knowing the partition function all properties of the systems can be determined.

At the critical point, the order parameter changes from zero to non-zero at an infinitely steep gradient, which corresponds to diverging response functions of the system. Although the phase transition is characterized by a macroscopic order parameter, the critical phenomenon is explained by the microscopic correlation function between its

constituents. The two-point spin-spin correlation function is defined as the statistical correlation between the spins in sites i and j:

$$G(\vec{r}_i, \vec{r}_j) = \langle (S_i - \langle S_i \rangle)(S_j - \langle S_j \rangle) \rangle \tag{2.7}$$

where $\vec{r}_i$ is the position vector of site i and $\langle S_i \rangle$ denotes the thermal average of spin at site i. In general, the correlation function decays exponentially to zero with distance and obeys the following relationship from the Ornstein-Zernike theory (Ornstein & Zernike, 1914):

$$G(\vec{r}) \sim r^{-\tau} \exp(-r/\xi) \tag{2.8}$$

where ξ is the correlation length of the system. However, close to the critical temperature, the correlation length diverges following an inverse-power law and is infinite at the critical point:

$$\xi \sim |t|^{-\nu} \tag{2.9}$$

where ν is the correlation length critical exponent and $t = \frac{T - T_c}{T_c}$ is the normalized temperature from the critical temperature. (2.8) is then reduce to a simple power law.

$$G(\vec{r}) \sim r^{-\tau} \tag{2.10}$$

with $\tau = d - 2 + \eta$ and η, also known as the anomalous critical exponent, is the Fisher's correction (Fisher, 1964) to Ornstein-Zernike theory. The correlation function is also proportional to the response function via the following relation:

$$\chi \sim N \int G(r) r^{d-1} dr \tag{2.11}$$

Therefore, all observed divergence of thermodynamic response function at the critical point is related to the diverging correlation length. Near the critical point, these response functions scale with a power law, each with a unique critical exponent (see Table 2.1).

Table 2.1: Type of critical exponents, definitions and theoretical values for 2D classical Ising model.

Type of Critical Exponents	Definition	Condition	Theoretical Value
Zero-field specific heat, α	$C_H \sim \lvert t\rvert^{-\alpha}$	$T \to T_c, B_z = 0$	0
Zero-field magnetization, β	$M_z \sim (-t)^{\beta}$	$T \to T_c^-, B_z = 0$	1/8
Zero-field isothermal susceptibility, γ	$\chi_T \sim \lvert t\rvert^{-\gamma}$	$T \to T_c, B_z = 0$	7/4
Correlation length, ν	$\xi \sim \lvert t\rvert^{-\nu}$	$T \to T_c, B_z = 0$	1
Two-point correlation function at CP, η	$G(\vec{r}) \sim 1/r^{d-2+\eta}$	$T \to T_c, B_z = 0$	1/4
Critical Isotherm, δ	$B_z \sim \lvert M_z\rvert^{\delta} sign(M_z)$	$T = T_c, B_z \to 0$	15

These critical exponents are not independent and related by exponent equalities (see Appendix A). The equalities, especially the hyperscaling relation, serves as a guideline for any numerical calculation of the critical exponents.

2.2 The Transverse-field Quantum Ising Model

While the classical Ising model consists of spins represented as an arrow in a 3-dimensional space but only pointing along one axis, the transverse field quantum Ising model (tQIM) has quantum operators replacing classical spins, with respective eigenvalues and eigenstates. Instead of limiting the spins along a single axis, the non-commutativity of the quantum operators allows non-zero magnetizations along all three axes through quantum observable averages, contrary to the classical Ising model. The Hamiltonian operator of the quantum Ising model is defined as follows:

$$\hat{H} = -J \sum_{<i,j>} \hat{S}_i^z \hat{S}_j^z - h \sum_k \hat{S}_k^x - B_z \sum_k \hat{S}_k^z \qquad (2.12)$$

where $\hat{S}_i^z = \frac{1}{2}\begin{pmatrix} 1 & 0 \\ 0 & -1 \end{pmatrix}$ and $\hat{S}_i^x = \frac{1}{2}\begin{pmatrix} 0 & 1 \\ 1 & 0 \end{pmatrix}$ are the z and x-spin operators respectively. While B_z and h are respectively the longitudinal and transverse fields. The reduced Planck's constant, $\hbar$ in the prefactor of the matrices are absorbed and effectively set to unity. The non-commutativity between the $\hat{S}_i^z$ and $\hat{S}_i^x$ operators introduces quantum fluctuations into the system, tuneable by the transverse field h. Without exactly solving the system, we can deduce in the limit $h \to \infty$ the ground state is paramagnetic state while

in the limit $h \to 0$, long-range order is established and the system is in the ferromagnetic state (Sachdev, 2011).

2.2.1 Exact Diagonalization

The naïve approach to solving a quantum many-body system and finding the ground state is by exact diagonalization of its Hamiltonian matrix $\boldsymbol{H}$ whose elements are defined by

$$H_{ij} = \langle i|\hat{H}|j\rangle \tag{2.13}$$

where $|i\rangle$ is one of the 2^L eigenstates corresponding to one classical configuration of the system. The Hamiltonian matrix is then diagonalized via methods such as the Lanczos (Lanczos, 1950; Paige, 1971; Paige 1972) or the Davidson algorithms (Davidson, 1975). However, the size of the matrix ($2^L \times 2^L$) is exponentially large and becomes impractical for a system size of order 2 and above, even for the Hamiltonian matrix in block diagonal form after considering parity conservation of Hamiltonian operator on the eigenvector basis. Finding the ground state eigenstate (the lowest eigenvalue and respective eigenvector), the thermodynamic quantities such as the specific heat, longitudinal magnetization, and its susceptibility, the two-point correlation length can be calculated by inner product multiplication between the ground state eigenvector $|\mathrm{GS}\rangle$ and quantum operator matrix $\hat{O}$:

$$\langle\hat{O}\rangle = \langle \mathrm{GS}|\hat{O}|\mathrm{GS}\rangle \tag{2.14}$$

where the elements, O_{ij} of the operator matrix is similarly defined as in (2.13).

2.2.2 Analytic Solution

For the one-dimensional tQIM, the analytical solution is found by mapping spin operators to fermionic variables using the Jordan-Wigner transformation and solve by exact diagonalization (Pfeuty, 1970; Elliott et. al., 1970). To transform the spin operators

to Jordan-Wigner fermions, periodic boundary condition (PBC) is imposed on the Hamiltonian (2.12). Therefore, Hamiltonian of 1D tQIM without longitudinal field is given by

$$\hat{H} = -J\sum_{j=1}^{L}\hat{S}_j^z\hat{S}_{j+1}^z - h\sum_{k=1}^{L}\hat{S}_k^x \tag{2.15}$$

where $\hat{S}_{L+1}^z = \hat{S}_1^z$. The detailed derivation of the analytical solution is given in Appendix B. After solving the Hamiltonian, the ground state energy of 1D tQIM is given by

$$E_0 = -\frac{Lh}{2\pi}\int_0^{\pi}\omega_q dq \tag{2.16}$$

Other thermodynamic quantities such as the magnetizations can be calculated using the Wick's Theorem to evaluate the vacuum expectation value of fermion operators. Therefore, the longitudinal magnetization M_z and transverse magnetization M_x is given by

$$M_x = \frac{1}{2}\cdot\frac{1}{\pi}\int_0^{\pi}\frac{1+\frac{J}{2h}\cos(q)}{\omega_q}dq \tag{2.17}$$

$$M_z = \frac{1}{2}\left(1-\frac{4h^2}{J^2}\right)^{1/8} \tag{2.18}$$

where $\omega_q = \sqrt{1+\frac{J^2}{4h^2}+\frac{J}{h}\cos(q)}$ and the one-half prefactor for M_z and M_x is due to the convention of S_i^z and S_i^x in (2.15).

2.3 Tensor Networks Formalism

The analytical solutions for quantum many-body systems are rare and numerical simulations to obtain the quantum wavefunction face difficulties in the exponentially large Hilbert space dimension with system sizes. However, from insights of quantum information studies (Srednicki, 1993; Eisert et. al., 2010), it is found that for system with local interactions and gapped Hamiltonian (non-zero gap between the ground state and first excitation state), the wavefunction is highly constrained. The wavefunction obeys the Area Law of entanglement entropy which states the quantum entanglement shared

between two parts of a bipartite system scales with the boundary between the parts instead of the volume. This enforces the locality of entanglement where eigenstates that encode long-range entanglement have less or insignificant weightage. This indicates that the wavefunction in complete Hilbert space can be approximated accurately within a subspace instead. The tensor network formalism, which splits the large coefficient tensor of the wavefunction into a network of smaller tensors mirroring the lattice of the physical system, allows efficient search and truncation of the redundant eigenstates (Orús, 2014). It reduces the computational complexity from order of exponential with system size $O(\exp(L))$ to only polynomial with system size $O(\text{poly}(L))$. Next, we start with graphical representation of tensors and their mathematical operations to understanding the utility of tensor networks.

2.3.1 Tensor Network Theory

Let us first introduce mathematical notions of tensors, which are the fundamental building blocks of a tensor network. A tensor is a multidimensional array of complex numbers. The rank of a tensor is the number of indices or the "dimension" of the array. For example, a vector (v_α) has only one index so it's a rank-1 tensor. A matrix ($M_{\alpha\beta}$) has two indices so it's a rank-2 tensor. A scalar has no index so it is a rank-0 tensor. A tensor can be represented diagrammatically as a graph, with vertex and its indices as the edges as shown in Figure 2.1:

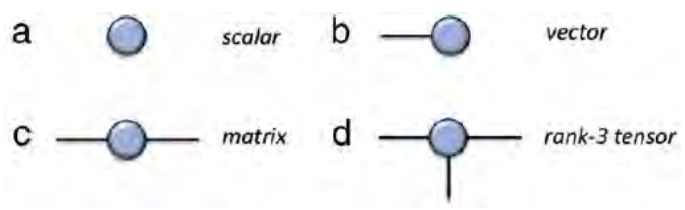

Figure 2.1: (a) scalar, (b) vector, (c) matrix and (d) rank-3 tensor. Image retrieved from (Orús, 2014).

A scalar is just a vertex while a vector is a vertex with an open edge. In general, a rank-N tensor has N open edges.

Various mathematical operations can be done between tensors to form a new tensor. For example, by contracting two tensors of their common indices one obtains a scalar:

$$\sum_{i=1}^{D} A_i B_i = C \tag{2.19}$$

where the index i is summed over its D possible values and C, in general, is a complex number. One can also obtain a new tensor by only contracting a subset of all indices:

$$\sum_j A_{ij} B_{jk} = C_{ik} \tag{2.20}$$

In this case, the index j is called the bond index while indices i and k are called open indices. If one multiplies different tensors without contracting any index, a higher rank tensor is produced:

$$A_i B_j = C_{ij} \tag{2.21}$$

In general, any tensor can be formed through the combination of contraction of indices and multiplications

$$\sum_{m,n} D_{im} E_{kn} F_{jmn} G_h = C_{ijkh} \tag{2.22}$$

The diagrammatic summary of the contractions and multiplications mentioned above are summarized in Figure 2.2

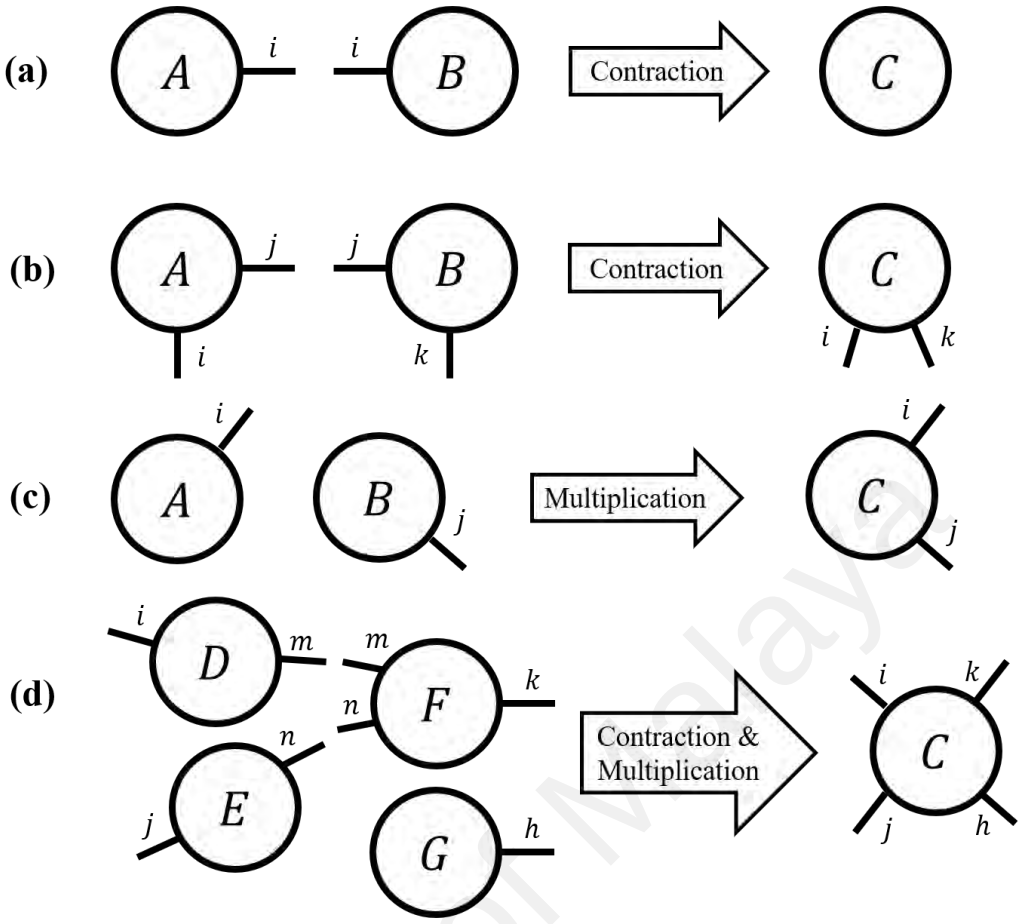

Figure 2.2: Summary of tensors manipulations from (2.19) to (2.22): (a) Scalar by Contraction (b) Tensor by Contraction (c) Tensor by Multiplication (d) All combinations of (a), (b), and (c).

A generic L spins quantum wavefunction in the Hilbert space formalism is given by:

$$|\Psi_L\rangle = \sum_{\{\sigma_i\}} C^{\sigma_1\sigma_2\ldots\sigma_L}|\sigma_1\sigma_2\ldots\sigma_L\rangle \tag{2.23}$$

where $\sigma_i = S_i^z$ is the z-spin eigenstate of the i-th spin and $\Sigma_{\{\sigma_i\}}$ is the sum over all possible combinations of eigenstates. For spins each with p eigenstates $C^{\sigma_1\sigma_2\ldots\sigma_L}$ is a rank L tensor with p^L components. In (2.20) tensors are contracted to form lower rank tensor. However, the reverse is also true and $C^{\sigma_1\sigma_2\ldots\sigma_L}$ can be split into contractions of many tensors along with the increase of many extra bond indices. The D possible values of the bond indices can be truncated due to the Area Law. This is the essence of the utility of the tensor network states. The process of splitting a higher rank tensor to a network of lower rank tensors is done via the Singular Value Decomposition (SVD) or alternatively known as the Schmidt Decomposition. The SVD will be explained in Chapter 3.

2.3.2 Matrix Product States

As mentioned earlier, the tensor network takes into account the entanglement structure of the system of interest. The entanglement structure, in turn, follows from the geometry of the system. For one-dimensional or pseudo-one-dimensional systems, the tensor network is known as the Matrix Product States (MPS). It resembles a connected one-dimensional array of tensors mirroring the one-dimensional geometry of spins. For open boundary conditions (OBC), the MPS is

$$|\mathrm{MPS}\rangle = \sum_{\{\sigma_i\},\{a_i\}} A^{\sigma_1}_{a_1} A^{\sigma_2}_{a_1 a_2} \dots A^{\sigma_L}_{a_{L-1}} |\sigma_1 \sigma_2 \dots \sigma_L\rangle \tag{2.24}$$

For periodic boundary condition (PBC),

$$|\mathrm{MPS}\rangle = \sum_{\{\sigma_i\},\{a_i\}} A^{\sigma_1}_{a_L a_1} A^{\sigma_2}_{a_1 a_2} \dots A^{\sigma_L}_{a_{L-1} a_L} |\sigma_1 \sigma_2 \dots \sigma_L\rangle \tag{2.25}$$

Notice that for the open boundary condition, the first and last matrix has only 2 indices. However, for periodic boundary conditions, they have 3 indices because they are connected by an extra common edge to impose the periodic boundary condition. The MPSs for both boundary conditions are shown diagrammatically below:

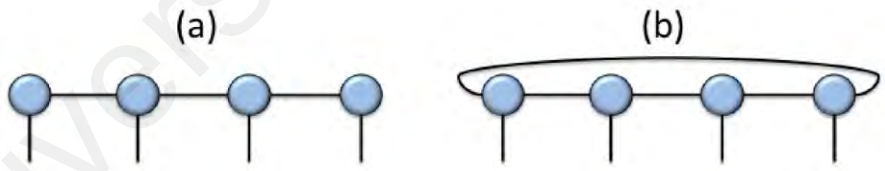

Figure 2.3: (a) MPS for OBC (b) MPS for PBC. Image retrieved from (Orús, 2014).

Note that the rank-L tensor $C^{\sigma_1 \sigma_2 \dots \sigma_L}$ is split into products of matrices. Hence the name Matrix Product State.

The MPS has the following basic properties. First, it is not translational invariant because all tensors in a finite-size MPS can be different. However, one may impose translational invariance by choosing some fundamental unit cell of tensors that is repeated indefinitely. For instance, if the unit cell consists of one tensor, the MPS will be

translational invariant over a one-site shift. For unit cells of two tensors, it is translational invariant by two-site shifts and so on. Next, by increasing the value of D, MPS can represent any quantum state in many-body Hilbert space. Therefore, we say that MPS are "dense". To cover all the states D needs to be exponentially large in the system size. However, it is known that the low energy states of local and gapped 1D Hamiltonians can be approximated very well by an MPS with just finite value of D (Verstraete & Cirac, 2006). For 1D critical systems, D tends to scale polynomially with the system size (Srednicki, 1993; Vidal et. al., 2003). The restriction of growth of D, in turn, explains the accuracy of MPS-based algorithms such as the Density Matrix Renormalization Group (DMRG). The MPS also satisfies the one-dimensional Area Law of entanglement entropy. The entanglement entropy is given by the following expression:

$$S(L) = -tr(\rho_L \log \rho_L) = O(\log D) \tag{2.26}$$

where ρ_L is the reduced density matrix of the block size L. The entanglement entropy is restricted by the rank D of the bond cut. For 1D critical systems with a polynomial scaling of D with the system size mentioned above, the entanglement entropy also scales with $S(L) \propto \log(L)$. This shows that MPS can also approximate the critical states very well. To calculate the expectation values, one contract two MPSs (Bra and Ket MPS) sandwiching an operator tensor (see Figure 2.4). This calculation can always be done exactly in time $O(LpD^3)$ for open boundary condition and $O(LpD^5)$ for periodic boundary condition. The calculation for PBC is less efficient but it is expected because more tensor indices are carried at each calculation step. For an infinite MPS, the calculation can be done in a shorter time of $O(pD^3)$. More details of derivation and calculations involving MPS will be described in Chapter 3.

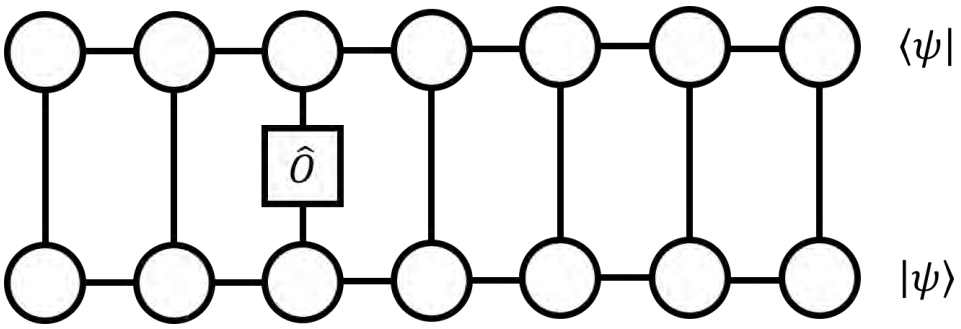

Figure 2.4: Diagrammatic representation of the expectation value of a local operator $\hat{O}$.

Despite the simplicity of the MPS, many non-trivial quantum states can be represented by MPS using only a very small bond dimension D. The first example being the GHZ state. An L spins-$1/2$ GHZ state is given by

$$|\mathrm{GHZ}\rangle = \frac{1}{\sqrt{2}}\left(|0\rangle^{\otimes L} + |1\rangle^{\otimes L}\right) \tag{2.27}$$

where $|0\rangle$ and $|1\rangle$ are spin-up and spin-down eigenstates of Pauli spin operator. The GHZ state is highly entangled and violates certain N-partite Bell inequalities. However, it can be represented exactly by an MPS with bond dimension $D = 2$ and periodic boundary conditions. Next, the ground state of the one-dimensional AKLT model (Affleck, et. al., 1987), which is a spin-1 quantum chain, is given by the Hamiltonian

$$H = \sum_i \left(\vec{S}^{[i]}\vec{S}^{[i+1]} + \frac{1}{3}\left(\vec{S}^{[i]}\vec{S}^{[i+1]}\right)^2\right) \tag{2.28}$$

where $\vec{S}^{[i]}$ is the vector of a spin-1 operator at site i. The AKLT model is a very important system which satisfies the Haldane's conjecture: it has Heisenberg-like interactions but, at the same time, it also has a non-vanishing gap in the thermodynamic limit. Therefore, it has potential for quantum information processing. It has an interesting connection to the MPS because its ground state can be constructed by splitting entangled spin-$1/2$ pairs and arrange each at two neighbouring sites. The two spins from different entangled pairs are at a single site and projected into spin-1 subspaces to form a spin-1 quantum chain. This results in an MPS with bond dimension $D = 2$. Finally, the Majumdar-Ghosh model, which is a frustrated spin chain defined by the Hamiltonian

$$H = \sum_i \left(\vec{S}^{[i]} \vec{S}^{[i+1]} + \frac{1}{2} \vec{S}^{[i]} \vec{S}^{[i+2]} \right) \tag{2.29}$$

where $\vec{S}^{[i]}$ is the vector of a spin-$1/2$ operator at site i. Its ground state is given by singlets between nearest-neighbour spins, and the superposition of the ground state and its translation by one lattice site forms an MPS of bond dimension $D = 3$.

2.3.3 Projected Entangled Pair States

The Projected Entangled Pair States (PEPS) is a natural generalization of the MPS to higher spatial dimensions (Cirac et. al., 2011). It can be constructed using the principle of projection to subspace similar to the AKLT model for quantum systems of any dimensions. For simplicity, here we only consider the two-dimensional (2D) case. Although in general, the 2D lattice could be of any shape, for example, the honeycomb lattice, triangular and kagome lattices, here we consider the simplest square lattice case to discuss the properties of PEPS.

For 2D PEPS, the generic wavefunction in Hilbert space formalism is no different from (2.23). However, when the rank L tensor $C^{\sigma_1 \sigma_2 \cdots \sigma_L}$ is split into a 2D tensor network, the resultant tensor network states consist of tensors each with a single-site index but with a different number of bond indices. For example, 4 bond indices for square lattice and 3 for the honeycomb lattice. For square lattice under open boundary condition, the edge and corner tensors will have 3 and 2 bond indices respectively, while for periodic boundary condition, all tensors have 4 bond indices (see Figure 2.5).

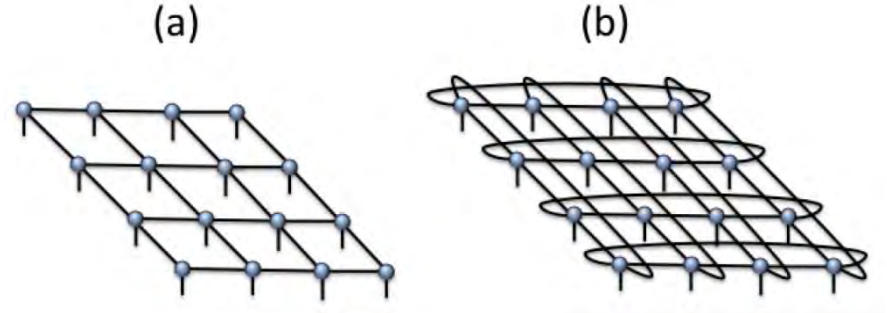

Figure 2.5: 4×4 PEPS (a) Open boundary conditions (b) Periodic boundary conditions. Image retrieved from (Orús, 2014).

Like the MPS, the PEPS need not be translational invariant because each tensor can be different. However, one may impose translational invariance by choosing a fundamental unit cell of tensors to be repeated indefinitely. For higher dimensional systems, this needs to be done to all spatial directions of the lattice to impose translational invariance. Next, the PEPS are also "dense" such that given sufficiently large bond dimension D, PEPS can represent any quantum state. As was the case for MPS, the bond dimension must be exponentially large in the system size to cover the whole Hilbert space. However, to apply the PEPS on interesting 2D quantum models, one expects reasonably small and finite bond dimension D for lower energy states. In fact, PEPS can handle polynomial decaying correlations, which is in stark contrast with MPS. In fact, it is well known with only $D = 2$ is sufficient to handle power-law correlation and hence critical states (Verstraete, et. al., 2006). Naturally, PEPS also satisfy the two-dimensional Area Law of entanglement entropy. In general, the entanglement entropy of a subsystem with boundary length l of a PEPS with bond dimension D is given as:

$$S(l) = O(l \log D) \tag{2.30}$$

Despite the advantage of PEPS to simulate critical states, the exact contraction of two PEPS is an exponentially hard problem. Exact contraction of two PEPS of L sites will always take a time $O(\exp(L))$, no matter the order in which we choose to contract the different tensors. Referring to computational complexity theory, the calculation belongs to the problem of complexity class #P-Hard (Schuch, et. al., 2007). However, the approximation of this contraction can be done accurately, at least for 2D PEPS of ground states of local, gapped Hamiltonian. The trick is to reduce the original 2D problem to a series of 1D problems, which in turn borrow the approximation advantages of MPS. The boundary rows of tensors are MPS while the inner rows are Matrix Product Operators (MPO), the quantum operator version of MPS. Contraction of two PEPS is done row by row and compression for each row, by bond dimension truncation, is done on the resulting

MPS and MPO to limit the complexity at each step. By this procedure, the contraction time is polynomial instead of exponential with system size. Another disadvantage of PEPS is that it has no exact canonical form. Unlike MPS with open boundary conditions, which a bond "cut" can split it into two separate parts, tensors in PEPS form closed loops. Therefore, one cannot define an orthonormal basis to the left and right part of a given bond index. Nevertheless, an approximate quasi-canonical form can be found for non-critical PEPS using "simple update" approach involving Suzuki-Trotter decomposition (Jiang, et. al., 2008).

Again, like the MPS, there are quantum states of 2D lattices that can be represented exactly using the PEPS. The first example being the Toric Code model, proposed by Kitaev (Kitaev, 2003). It is a spin-$1/2$ model on the links of a 2D square lattice, which is the simplest known model whose ground state displays topological order. The Hamiltonian is defined as follows:

$$H = -J_a \sum_s A_s - J_b \sum_p B_p \tag{2.31}$$

where $A_s = \prod_{\vec{r} \in s} \sigma_x^{[\vec{r}]}$ and $B_p = \prod_{\vec{r} \in p} \sigma_z^{[\vec{r}]}$ are star and plaquette operators respectively. In other words, A_s is product of σ_x operators around a star, and B_p is product of σ_z operators around a plaquette (see Figure 2.6). The ground state of an infinite 2D lattice Toric Code model can be represented with a PEPS with just $D = 2$ bond dimensions (Verstrate, et. al., 2006). Another example is the 2D AKLT model on a honeycomb lattice, given by the Hamiltonian:

$$H = \sum_{\langle \vec{r}, \vec{r}\prime \rangle} \left(\vec{S}^{[\vec{r}]} \vec{S}^{[\vec{r}\prime]} + \frac{116}{243} (\vec{S}^{[\vec{r}]} \vec{S}^{[\vec{r}\prime]})^2 + \frac{16}{243} (\vec{S}^{[\vec{r}]} \vec{S}^{[\vec{r}\prime]})^3 \right) \tag{2.32}$$

where $\vec{S}^{[\vec{r}]}$ is the vector of spin-$3/2$ operator at site $\vec{r}$, $\langle \vec{r}, \vec{r}' \rangle$ refers to the nearest neighbour spin pair. As one may suspect, the spin-$3/2$ at each site is constructed from 3 spin-$1/2$ singlet pairs and projected to symmetric spin-$3/2$ subspace. This resultant PEPS only requires bond dimension $D = 2$. Finally, the 2D resonating valence bond

(RVB) state proposed to explain the mechanism of high-T_c superconductivity (Anderson, 1987) can be represented with a PEPS with just $D = 3$ bond dimensions. The RVB state corresponds to equal superpositions of all possible nearest neighbour dimer covering the 2D lattice, where each dimer is an SU(2) singlet:

$$|\Phi\rangle = \frac{1}{\sqrt{2}}(|0\rangle\otimes|1\rangle - |1\rangle\otimes|0\rangle) \tag{2.33}$$

This state is important as it is the archetypical example of a quantum spin liquid.

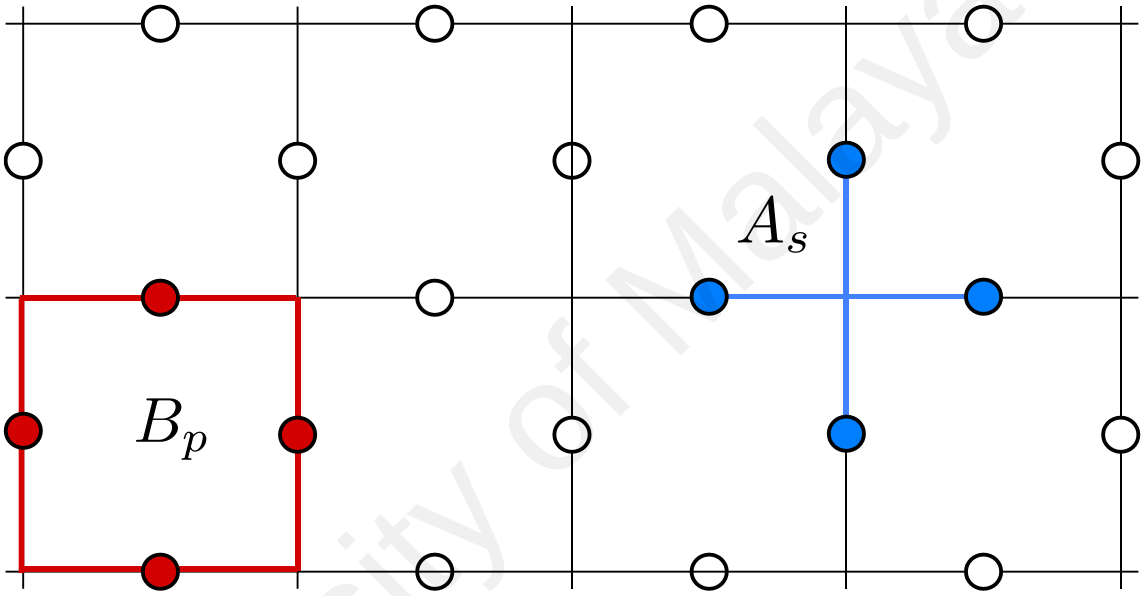

Figure 2.6: The star (A_s) and plaquette (B_p) operators of the Toric code. Image retrieved on December 1, 2020 from URL https://topocondmat.org/w12_manybody/topoorder.html.

2.3.4 Other Tensor Networks & Recent Developments

MPS and PEPS are actually special cases of tensor networks without extra dimensions. In order to study renormalization procedures on the systems, extra dimensions are needed to encode the system at different scales of observation. These extra dimensions offer a built-in structure of the tensor networks to accommodate renormalization procedures. Examples of tensor networks with extra dimensions are the Tree Tensor Network (TTN) (Shi, et. al., 2006) and the Multiscale Entanglement Renormalization Ansatz (MERA) (Vidal, 2007). The TTN has tree-like structures starting with a "root" tensor and branches

off with a fixed number of tensors. By construction, the TTN is made up of isometric tensors, has finite correlation length and on average satisfies the 1D Area Law of entanglement entropy. Besides well suited for gapped 1D systems, it is also used on 1D critical systems (Silvi, et. al., 2010) and 2D systems (Tagliacozzo, et. al., 2009). Since TTN is loop-free, it has a canonical form like MPS and the computation of expectation value of an observable is exact. MERA, on the other hand, is essentially a TTN but with extra unitary "disentangler" tensors in between each layer, which account for entanglement between neighbouring sites. Therefore, it can handle the entanglement entropy of 1D critical systems (Evenbly & Vidal, 2013). Additionally, MERA has an extra holographic dimension that allows "entanglement renormalization" and is believed to be related to AdS/CFT correspondence in quantum gravity (Swingle, 2012). Lastly, MERA tensors form loops and thus have no canonical form. However, the computation of an observable's expectation value is exact.

Finally, to establish tensor network formalism as an alternative formalism for quantum field theories, the structures discussed above allow a continuum limit. Continuous tensor networks such as continuous MPS (cMPS) (Verstraete & Cirac, 2010), continuous PEPS (cPEPS) (Jennings, et. al., 2015), continuous MERA (cMERA) (Haegeman, et. al., 2013) are proposed.

CHAPTER 3: METHODOLOGY

In this chapter, we will introduce in detail the Matrix Product States (MPS) formalism as the numerical technique to approximate the wavefunction in the form of a one-dimensional tensor network and associated techniques to efficiently calculate the expectation values of quantum observables. Next, the Density Matrix Renormalization Group (DMRG), which is the ground state search algorithm that results in the ground state wavefunction in MPS form, is presented. The background of DMRG is briefly reviewed along with its traditional and modern variants. Finally, the finite-size scaling (FSS) theory that allows one to calculate the critical exponents from finite-size simulations is introduced.

3.1 Matrix Product States Formalism

As mentioned in expression (2.23) in Chapter 2, the many-body quantum wavefunction can be equivalently described by a rank-L tensor $C^{\sigma_1\sigma_2\cdots\sigma_L}$ where the L is the system size. For spin-$1/2$ system, the tensor has 2^L components. This large tensor can be split into a network of connected tensors of smaller ranks through the method known as the Singular Value Decomposition (SVD). The SVD is the general case of eigenvalue decomposition which requires the matrix to be a square matrix. SVD, on the other hand, can be done on a matrix of any shape, from 2D rectangular matrices to multidimensional arrays. For simplicity, we introduce the SVD with a generic $m \times n$ rectangular matrix.

3.1.1 Singular Value Decomposition

For an arbitrary rectangular $m \times n$ matrix $\boldsymbol{M}$ it can be decomposed into a product of three matrices:

$$\boldsymbol{M} = \boldsymbol{U}\boldsymbol{\Lambda}\boldsymbol{V}^{\dagger} \tag{3.1}$$

where $\boldsymbol{U}$ is an $m \times m$ unitary matrix whose columns are orthonormal singular vectors, i.e. $\boldsymbol{U}^{\dagger}\boldsymbol{U} = \boldsymbol{I}$. $\boldsymbol{\Lambda}$ is an $m \times n$ matrix with diagonal entries of non-negative real numbers. $\boldsymbol{V}$ is an $n \times n$ unitary matrix who rows are orthonormal singular vectors, i.e. $\boldsymbol{V}\boldsymbol{V}^{\dagger} = \boldsymbol{I}$. The entries in $\boldsymbol{\Lambda}$ are called the singular values λ where each λ_i corresponds to the left and right singular vector ($\vec{u}_i$ and $\vec{v}_i$) in columns and rows of $\boldsymbol{U}$ and $\boldsymbol{V}$ respectively. The total number of non-zero singular values $\chi = \min(m, n)$ and we say that matrix $\boldsymbol{M}$ has rank χ. In descending order, the singular values and corresponding singular vectors signify the decrease in importance of certain components of the transformation matrix $\boldsymbol{M}$. By only keeping $D < \chi$ number of singular values, we can optimally approximate matrix $\boldsymbol{M}$ with another matrix of lower rank $\boldsymbol{M'}$.

Although the SVD is an algorithm for the optimal approximation of an arbitrary matrix, it is closely related to the entanglement between bipartite quantum system. For a composite quantum system in a pure state $|\psi\rangle$, we can partition the system into two parts of A and B and determine the bipartite entanglement between them. There exist orthonormal states $|i_A\rangle$ and $|i_B\rangle$ for system A and B, respectively, such that

$$|\psi\rangle = \sum_{i=1}^{\chi} \lambda_i |i_A\rangle |i_B\rangle \tag{3.2}$$

Notice the similar notation of λ_i and χ with the explanation of SVD. (3.2) is known as the Schmidt decomposition of a quantum state and λ_i, which satisfies the relation

$$\sum_i \lambda_i^2 = 1 \tag{3.3}$$

is known as the Schmidt coefficients. For a quantum system with arbitrary partition A and B, let the orthonormal bases be $|j\rangle$ and $|k\rangle$ respectively. Then the quantum state of the composite system is written as

$$|\psi\rangle = \sum_{j,k} a_{jk} |j\rangle |k\rangle \tag{3.4}$$

for some matrix $\boldsymbol{A}$ with complex element a_{jk}. By doing SVD on a_{jk}, (3.4) can be expressed as

$$|\psi\rangle = \sum_{i,j,k} u_{ji} d_{ii} v_{ik} |j\rangle|k\rangle \quad (3.5)$$

By defining $|i_A\rangle \equiv \sum_j u_{ji}|j\rangle$, $|i_B\rangle \equiv \sum_k v_{ik}|k\rangle$ and $\lambda_i \equiv d_{ii}$ we retrieve (3.2). Note that $|i_A\rangle$ and $|i_B\rangle$ are orthonormal bases due to unitary of matrix $\boldsymbol{U}$ and $\boldsymbol{V}$. For a composite quantum system AB with quantum state $|\psi\rangle$, the density matrix is given by

$$\rho = |\psi\rangle\langle\psi| = \sum_i \lambda_i^2 \, |i_A\rangle\langle i_A| \otimes |i_B\rangle\langle i_B| \quad (3.6)$$

By performing a partial trace on ρ the density matrix of partition A and B is obtained:

$$\rho_A = Tr_B \, \rho = \sum_i \lambda_i^2 \, |i_A\rangle\langle i_A| \quad (3.7)$$

$$\rho_B = Tr_A \, \rho = \sum_i \lambda_i^2 \, |i_B\rangle\langle i_B| \quad (3.8)$$

The Von Neumann entanglement entropy S_{vN} between partition A and B is given by

$$S_{vN} = -\sum_{i=1}^{\chi} \lambda_i^2 \log \lambda_i^2 \quad (3.9)$$

The constraint given by (3.3) enforces λ_i to follow a decaying spectrum for short-range interacting systems. Therefore, if λ_i decays exponentially, keeping just a few largest values of λ_i accurately approximates the quantum state (Schollwöck, 2005; Verstraete & Cirac, 2006).

3.1.2 Derivation of Matrix Product States

A generic quantum wavefunction of one-dimensional spin chain with L sites and local state space $\{|\sigma_i\rangle\}$ of dimension p can be written as

$$|\Psi\rangle = \sum_{\{\boldsymbol{\sigma}\}} C^{\boldsymbol{\sigma}} |\boldsymbol{\sigma}\rangle \quad (3.10)$$

where $|\boldsymbol{\sigma}\rangle = |\sigma_1 \sigma_2 \ldots \sigma_L\rangle$ and $\Sigma_{\{\boldsymbol{\sigma}\}}$ is the sum over all combinations of local states. The rank-L tensor $C^{\boldsymbol{\sigma}}$ can be split into smaller tensors iteratively by SVDs. Although conventionally coefficients representing a vector in Hilbert space are contravariant tensors with superscript indices, at the end of this section we will be allocating subscript and superscript indices to differentiate the bond indices and site indices respectively. First, we will conform to the subscript index notation of SVD used in Section 3.1.1. The

multidimensional tensor C^{σ} is reshaped into a two-dimensional rectangular matrix of dimension $(p \times p^{L-1})$:

$$C_{\sigma_1\sigma_2\ldots\sigma_L} = C_{\sigma_1,(\sigma_2\ldots\sigma_L)} \tag{3.11}$$

After performing SVD on (3.11) the tensor is decomposed into the form:

$$C_{\sigma_1,(\sigma_2\ldots\sigma_L)} = \sum_{a_1} U_{\sigma_1,a_1}\Lambda_{a_1}V^{\dagger}_{a_1,(\sigma_2\ldots\sigma_L)} \tag{3.12}$$

where a_1 is the bond indices connecting site 1 and 2 and the matrix U_{σ_1,a_1} has a dimension of $p \times p$ because $\chi = \min(p, p^{L-1})$. This operation can be diagrammatically represented as the figure below:

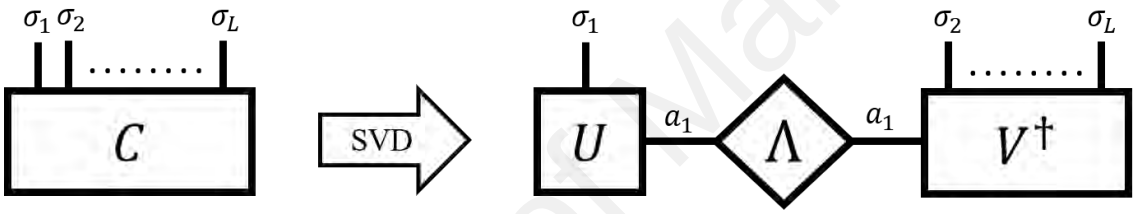

Figure 3.1: Diagrammatic representation of tensor decomposition by SVD.

Next, we multiply $\Lambda_{a_1}V^{\dagger}_{a_1,(\sigma_2\ldots\sigma_L)}$ and reshape it into a new tensor of rank $L-1$, $C_{(a_1\sigma_2),(\sigma_3\ldots\sigma_L)}$ with dimension $(p^2 \times p^{L-2})$. By performing SVD again we obtain:

$$C_{(a_1\sigma_2),(\sigma_3\ldots\sigma_L)} = \sum_{a_2} U_{(a_1\sigma_2),a_2}\Lambda_{a_2}V^{\dagger}_{a_2,(\sigma_3\ldots\sigma_L)} \tag{3.13}$$

where a_2 is the bond indices connecting site 2 and 3 and with the matrix $U_{(a_1\sigma_2),a_2}$ has a dimension of $(p^2 \times p^2)$. By repeating this procedure until the last site of the chain, we transform (3.10) into a product of sequences of U matrices:

$$|\Psi\rangle = \sum_{\{\sigma\}}\sum_{a_1,\ldots,a_{L-1}} U_{\sigma_1,a_1}U_{(a_1\sigma_2),a_2}\ldots U_{(a_{L-2}\sigma_{L-1}),a_{L-1}}U_{(a_{L-1}\sigma_L),1}|\boldsymbol{\sigma}\rangle \tag{3.14}$$

The matrices beginning from site 1 to site L has the following dimensions: $(1 \times p)$, $(p \times p^2)$, …, $(p^{L/2-1} \times p^{L/2})$, $(p^{L/2} \times p^{L/2-1})$, …, $(p^2 \times p)$, $(p \times 1)$. Here, a new tensor A with a different rearrangement of indices is introduced to differentiate between bond and site indices with subscript and superscript respectively. Then (3.14) becomes:

$$|\mathrm{MPS}\rangle_{\mathrm{left}} = \sum_{\{\sigma\}} \sum_{a_1,\ldots,a_{L-1}} A^{\sigma_1}_{a_1} A^{\sigma_2}_{a_1 a_2} \ldots A^{\sigma_{L-1}}_{a_{L-2} a_{L-1}} A^{\sigma_L}_{a_{L-1}} |\boldsymbol{\sigma}\rangle \tag{3.15}$$

The diagrammatic representation of MPS is shown in Figure 3.2:

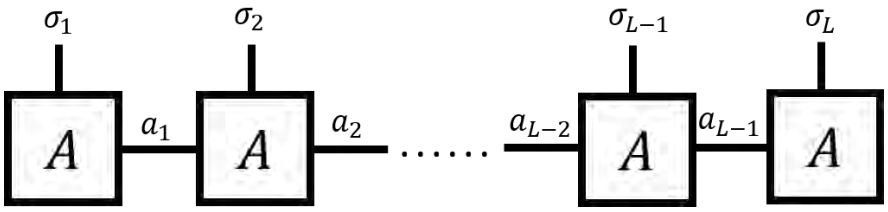

Figure 3.2: Diagrammatic representation of Matrix Product States.

The subscript "left" of (3.15) represents the left-canonical form of MPS by splitting the tensor from the left of the spin chain. Canonical forms greatly simplify computations of local expectation values as we shall see in the subsequent section. When the MPS is formed, regardless it is in full bond dimensions, compression can be done using the SVD. One can contract two tensors, perform the SVD and truncate the singular matrix $\boldsymbol{\Lambda}$ by keeping only m singular values. Alternatively, one can set the truncation error bound and keep a varying number of singular values kept at different bonds.

3.1.3 Canonical Form and Variational Compression of Matrix Product States

The tensor is split from the left of the spin chain from (3.12) to (3.14). At each step the matrix $\boldsymbol{U}$, or in the present notation matrix $\boldsymbol{A}$, is left-normalized, i.e.:

$$\sum_{\sigma_i} A^{\sigma_i \dagger} A^{\sigma_i} = I \tag{3.16}$$

where the bond indices are implicit. Diagrammatically (3.16) can be represented as:

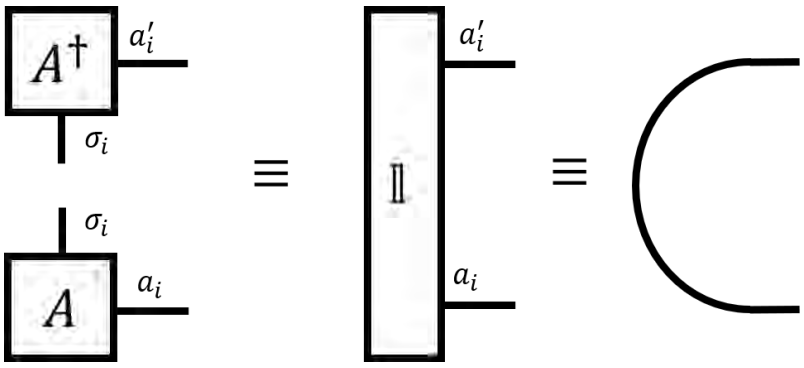

Figure 3.3: Diagrammatic representation of left-normalized tensor contraction.

Therefore, (3.15) is called the left-canonical form. However, if the tensor is split from the right of the spin chain, then (3.12) would instead be:

$$C_{(\sigma_1 \dots \sigma_{L-1}),\sigma_L} = \sum_{a_{L-1}} U_{(\sigma_1 \dots \sigma_{L-1}),a_{L-1}} \Lambda_{a_{L-1}} V^{\dagger}_{a_{L-1},\sigma_L} \tag{3.17}$$

By repeating SVDs one site at a time one obtains a right-canonical form:

$$|\mathrm{MPS}\rangle_{\mathrm{right}} = \sum_{\{\boldsymbol{\sigma}\}} \sum_{a_1,\dots,a_{L-1}} B^{\sigma_1}_{a_1} B^{\sigma_2}_{a_1 a_2} \dots B^{\sigma_{L-1}}_{a_{L-2} a_{L-1}} B^{\sigma_L}_{a_{L-1}} |\boldsymbol{\sigma}\rangle \tag{3.18}$$

where $\boldsymbol{B}$ is right-normalized matrix:

$$\sum_{\sigma_i} B^{\sigma_i} B^{\sigma_i \dagger} = I \tag{3.19}$$

with the bond indices implicit. Similarly, (3.19) can be diagrammatically represented as:

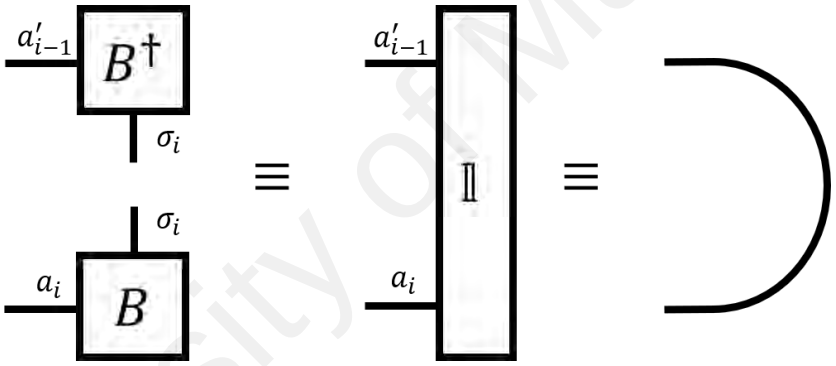

Figure 3.4: Diagrammatic representation of right-normalized tensor contraction.

The advantage of the canonical form is obvious when the mix-canonical form is introduced. By splitting the tensor from both left and right of the spin chain until a site j, the MPS has the mix-canonical form:

$$|\mathrm{MPS}\rangle_{\mathrm{mix}} = \sum_{\{\boldsymbol{\sigma}\}} \sum_{a_1,\dots,a_{L-1}} A^{\sigma_1}_{a_1} \dots A^{\sigma_{j-1}}_{a_{j-2} a_{j-1}} \Psi^{\sigma_j}_{a_{j-1} a_j} B^{\sigma_{j+1}}_{a_j a_{j+1}} \dots B^{\sigma_L}_{a_{L-1}} |\boldsymbol{\sigma}\rangle \tag{3.20}$$

where the site j is called the orthogonality center. To compute the expectation value of a single site operator at site j, one only needs to contract three tensors due to (3.16) and (3.19):

$$\langle \mathrm{MPS}|\hat{O}_j|\mathrm{MPS}\rangle = \sum_{a_{j-1},a_j,\sigma_j,\sigma_j'} \Psi^{\sigma_j}_{a_{j-1}a_j} \hat{O}^{\sigma_j,\sigma_j'} \Psi^{\sigma_j'\,\dagger}_{a_{j-1}a_j} \tag{3.21}$$

This greatly simplifies the computation cost which is just p^2D^2 without scaling with system size. The canonical forms are actually special cases of gauge freedom. The MPS is invariant under gauge transformation by treating a bond as an identity tensor and split it into two invertible matrices:

$$\mathbb{I} = \boldsymbol{X}\boldsymbol{X}^{-1} \tag{3.22}$$

The gauge transformation between tensor at site i and $i+1$ is:

$$A^{\sigma_i} \to A^{\sigma_i}X \qquad A^{\sigma_{i+1}} \to X^{-1}A^{\sigma_{i+1}} \tag{3.23}$$

The gauge degree of freedom can simplify manipulations drastically, setting the orthogonality center as we wish without starting from C^{σ} through the procedures in (3.11) to (3.15). This is especially important after we obtain the ground state wavefunction in MPS because all computations using (3.21) require MPS in mixed canonical form. Manipulation methods to set the orthogonality center is needed without reverting back to large tensor C^{σ}.

Now that the canonical forms are introduced, the MPS can also be compressed with the variational method, which is the basis of modern DMRG as a variational ground state search algorithm. Let's say we want to compress an MPS wavefunction $|\psi\rangle$ with bond dimension D into a new MPS $|\tilde{\psi}\rangle$ with smaller bond dimension $\widetilde{D}$, minimizing the square of two-norm $\||\psi\rangle - |\tilde{\psi}\rangle\|_2^2$. This means that we want to minimize the two-norm squared with respect to all the tensors of the new MPS:

$$\min_{\tilde{\psi}}\{ \left(\langle\psi| - \langle\tilde{\psi}|\right)\left(|\psi\rangle - |\tilde{\psi}\rangle\right) \} = \min_{\tilde{\psi}}\left(\langle\psi|\psi\rangle - \langle\tilde{\psi}|\psi\rangle - \langle\psi|\tilde{\psi}\rangle + \langle\tilde{\psi}|\tilde{\psi}\rangle\right) \tag{3.24}$$

However, this is a highly nonlinear optimization problem. A more feasible way is to find the gradient of the two-norm squared with respect to one tensor only, equate the gradient to be zero in order to evaluate the optimum single tensor and repeat for all sites. This is

done by finding the new $\tilde{A}^{\sigma_i}$ via extremizing with respect to $\tilde{A}^{\sigma_i *}_{a_{i-1}a_i}$, the i-th tensor in ⟨MPS|, which only shows up in $-\langle\tilde{\psi}|\psi\rangle + \langle\tilde{\psi}|\tilde{\psi}\rangle$ (Schollwöck, 2011). Explicitly, the expression is as follows:

$$\frac{\partial}{\partial \tilde{A}^{\sigma_i *}_{a_{i-1}a_i}}\left(\langle\tilde{\psi}|\tilde{\psi}\rangle - \langle\tilde{\psi}|\psi\rangle\right) =$$

$$\sum_{\boldsymbol{\sigma}^*}\left(\tilde{A}^{\sigma_1 *} \dots \tilde{A}^{\sigma_{i-1} *}\right)_{1,a_{i-1}}\left(\tilde{A}^{\sigma_{i+1} *} \dots \tilde{A}^{\sigma_L *}\right)_{a_i,L}\tilde{A}^{\sigma_1} \dots \tilde{A}^{\sigma_i} \dots \tilde{A}^{\sigma_L} - \tag{3.25}$$

$$\sum_{\boldsymbol{\sigma}^*}\left(\tilde{A}^{\sigma_1 *} \dots \tilde{A}^{\sigma_{i-1} *}\right)_{1,a_{i-1}}\left(\tilde{A}^{\sigma_{i+1} *} \dots \tilde{A}^{\sigma_L *}\right)_{a_i,L}A^{\sigma_1} \dots A^{\sigma_i} \dots A^{\sigma_L} = 0$$

where $\boldsymbol{\sigma}^*$ refers to sum over all indices except those connected to $\tilde{A}^{\sigma_i *}_{a_{i-1}a_i}$. While the algebraic expression is explicit, the diagrammatic representation is more intuitive (see Figure 3.5).

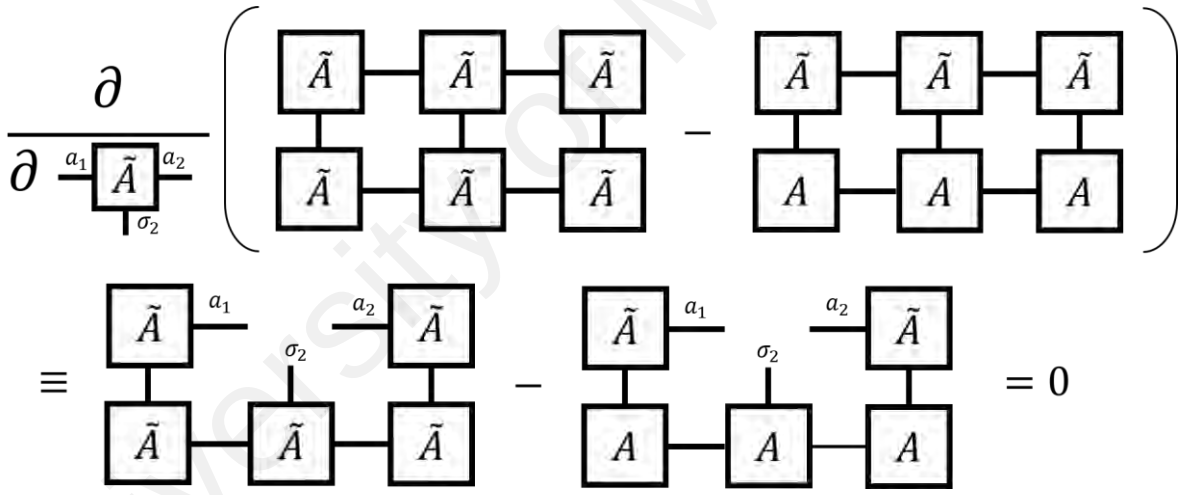

Figure 3.5: Diagrammatic representation of finding the gradient of a 3-site tensor network contraction with respect to the 2nd site.

Expression (3.25) can be simplified by grouping all other tensors except $\tilde{A}^{\sigma_i}$ as large tensor:

$$\sum_{a'_{i-1},a'_i} \tilde{O}_{a_{i-1}a_i a'_{i-1}a'_i}\tilde{A}^{\sigma_i}_{a'_{i-1}a'_i} = O^{\sigma_i}_{a_{i-1}a_i} \tag{3.26}$$

By reshaping $\tilde{A}^{\sigma_i}$ as a vector $\vec{v}$, $\tilde{O}$ as a matrix $\boldsymbol{P}$ and O^{σ_i} as a vector $\vec{b}$ we get

$$\boldsymbol{P}\vec{v} = \vec{b} \tag{3.27}$$

Therefore, the variational compression is reduced to a problem of solving a system of linear equations, which can be efficiently solved by methods of linear algebra.

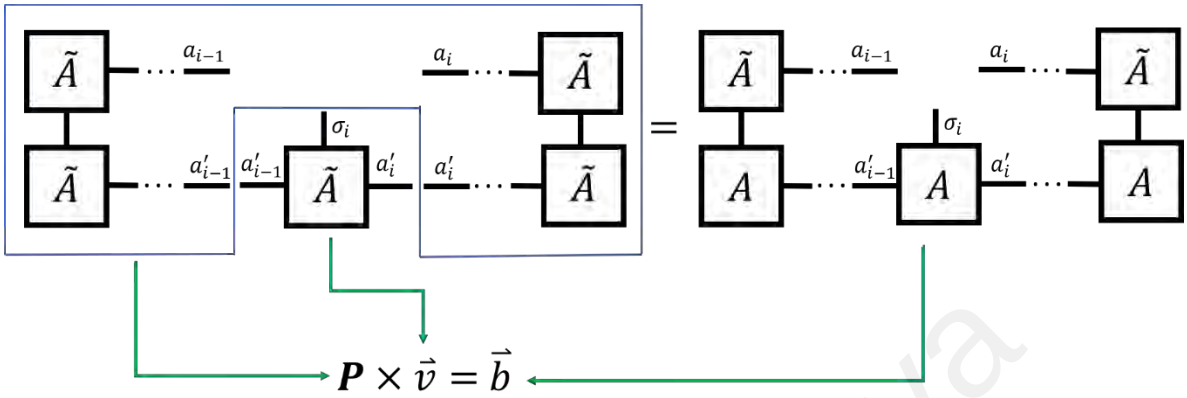

Figure 3.6: Diagrammatic representation of expression (3.26) and (3.27).

Note that if the MPS is in the mix-canonical form with orthogonal center at site i, the reshaped matrix $\boldsymbol{P}$ becomes an identity matrix. Therefore, (3.27) is further reduced to

$$\vec{v} = \vec{b} \tag{3.28}$$

The procedures described above for variational compression are done iteratively on all the sites, sweeping across the 1D tensor networks. Multiple sweeps can be done until the tensors converge.

3.1.4 Quantum Operator as Matrix Product Operator

Similarly, a generic quantum observable operator is also rank-$2L$ tensor defined as follows:

$$\hat{O} = \sum_{\{\boldsymbol{\sigma}\},\{\boldsymbol{\sigma}'\}} O^{\boldsymbol{\sigma}}_{\boldsymbol{\sigma}'} |\boldsymbol{\sigma}\rangle\langle\boldsymbol{\sigma}'| \tag{3.29}$$

where $O^{\boldsymbol{\sigma}}_{\boldsymbol{\sigma}'}$ is explicitly $O^{\sigma_1\sigma_2\ldots\sigma_L}_{\sigma'_1\sigma'_2\ldots\sigma'_L}$. (3.29) can be represented diagrammatically as shown in Figure 3.7:

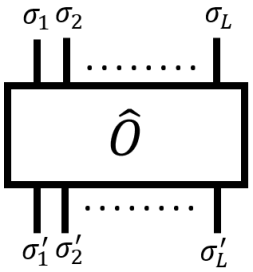

Figure 3.7: Diagrammatic representation of generic quantum observable operator.

Next, by repeatedly performing SVD on $O^{\sigma_1\sigma_2\ldots\sigma_L}_{\sigma_1'\sigma_2'\ldots\sigma_L'}$, one obtains the Matrix Product Operator (MPO):

$$\text{MPO} = \sum_{\{\sigma_i\},\{\sigma_i'\},\{b_i\}} W_{b_1}^{\sigma_1\sigma_1'} W_{b_1 b_2}^{\sigma_2\sigma_2'} \ldots W_{b_{L-1}}^{\sigma_L\sigma_L'} |\boldsymbol{\sigma}\rangle\langle\boldsymbol{\sigma}'| \tag{3.30}$$

where b_i is the bond indices of the MPO. The singular value tensors for (3.30) are absorbed by neighbouring site tensors. The MPO can be diagrammatically represented as shown in Figure 3.8:

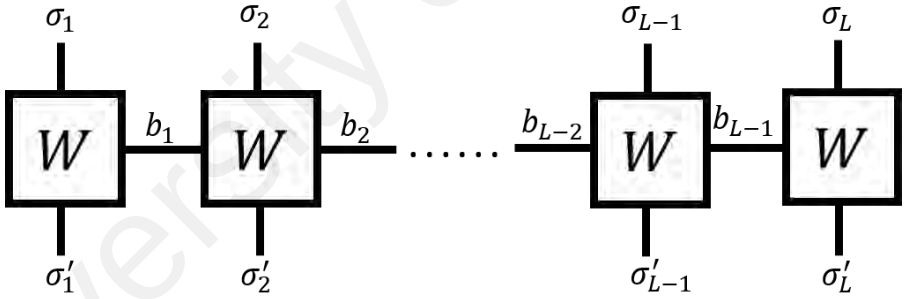

Figure 3.8: Diagrammatic representation of a Matrix Product Operator.

The advantage of expressing a quantum operator as MPO is the form invariance of applying the MPO to an MPS (see Figure 3.9):

$$\begin{aligned}
\text{MPO}|\text{MPS}\rangle &= \sum_{\{\sigma_i\},\{\sigma_i'\}} \left(W^{\sigma_1\sigma_1'} W^{\sigma_2\sigma_2'} \ldots\right)\left(A^{\sigma_1'} A^{\sigma_2'} \ldots\right)|\boldsymbol{\sigma}\rangle \\
&= \sum_{\{\sigma_i\},\{\sigma_i'\}} \sum_{\{a_i\},\{b_i\}} \left(W_{b_1}^{\sigma_1\sigma_1'} W_{b_1 b_2}^{\sigma_2\sigma_2'} \ldots\right)\left(A_{a_1}^{\sigma_1'} A_{a_1 a_2}^{\sigma_2'} \ldots\right)|\boldsymbol{\sigma}\rangle \\
&= \sum_{\{\sigma_i\},\{\sigma_i'\}} \sum_{\{a_i\},\{b_i\}} \left(W_{b_1}^{\sigma_1\sigma_1'} A_{a_1}^{\sigma_1'}\right)\left(W_{b_1 b_2}^{\sigma_2\sigma_2'} A_{a_1 a_2}^{\sigma_2'}\right) \ldots |\boldsymbol{\sigma}\rangle \\
&= \sum_{\{\sigma_i\}} N^{\sigma_1} N^{\sigma_2} \ldots |\boldsymbol{\sigma}\rangle
\end{aligned} \tag{3.31}$$

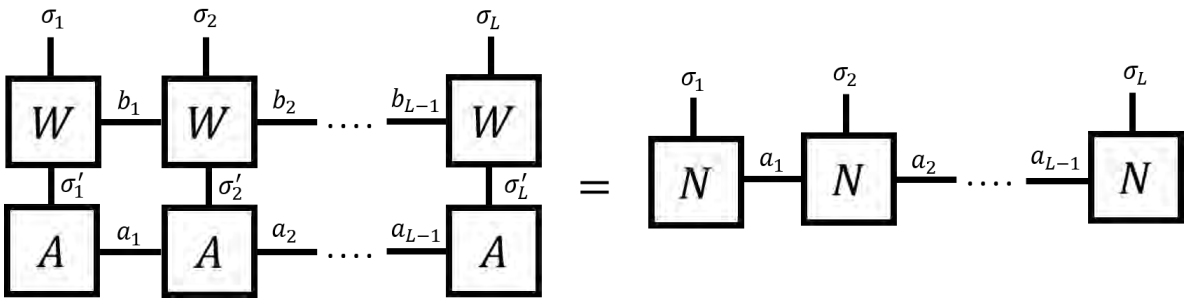

Figure 3.9: Diagrammatic representation of applying an MPO to an MPS.

The new MPS has bond dimensions $D = a_i b_i$, which can be compressed to lower dimensions. This allows one to time-evolve an MPS by expressing the time evolution operator as an MPO and repeatedly apply it to the MPS. The form invariance ensures the quantum state remains as MPS, which has polynomial complexity, at each time step. Next, an MPO can also be compressed like an MPS, either via SVDs or variational compression by treating two site indices (σ_i, σ_i') as one, to ensure polynomial complexity. For complicated global operator as in (3.29), one can convert it into MPO, compresses it and compute the expectation value via contracting the $\langle \mathrm{MPS}|\mathrm{MPO}|\mathrm{MPS}\rangle$ sandwiched tensor network (see Figure 3.10).

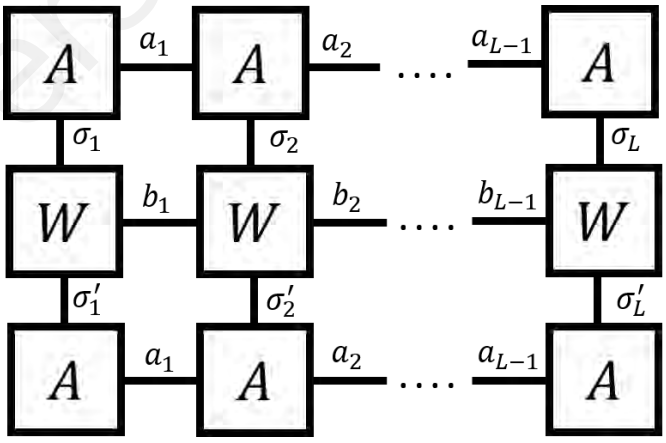

Figure 3.10: Diagrammatic representation of $\langle \mathrm{MPS}|\mathrm{MPO}|\mathrm{MPS}\rangle$ tensor network contraction.

Again, like an MPS, the MPO can also be converted to left, right or mix-canonical form by splitting the original operator tensor from different directions or via gauge freedom transformation.

3.2 Density Matrix Renormalization Group

In order to study the thermodynamic properties of tQIM in the ground state, the MPS must be representing the ground state wavefunction. The density matrix renormalization group (DMRG) is the numerical method that iteratively finds the ground state wavefunction by selecting and keeping the most important eigenstates that maximize the entanglement entropy and truncate the rest. It is first proposed by White in 1992 (White, 1992; White, 1993) to solve for the one-dimensional quantum spin chain when the previous Numerical Renormalization Group (NRG) method fails.

3.2.1 Wilson's Numerical Renormalization Group

Wilson proposed the Real-Space Numerical Renormalization Group (NRG) to solve the Kondo problem of magnetic impurity (Wilson, 1975). Despite the success of NRG with the Kondo problem, it performs very poorly in other quantum lattice models. In the context of DMRG on the quantum Ising spin system, to study a system in the thermodynamic limit, the infinite system is first described by the Hamiltonian of a subsystem, here defined as a "block". The Hamiltonian matrix defined by a certain basis is formed and diagonalized, and the few lowest eigenstates are kept. The new subsystem is formed with the diagonalized block combined with its own copy to obtain the new subsystem of double the original scale, here defined as the "superblock". The formation of the superblock is represented diagrammatically in Figure 3.11.

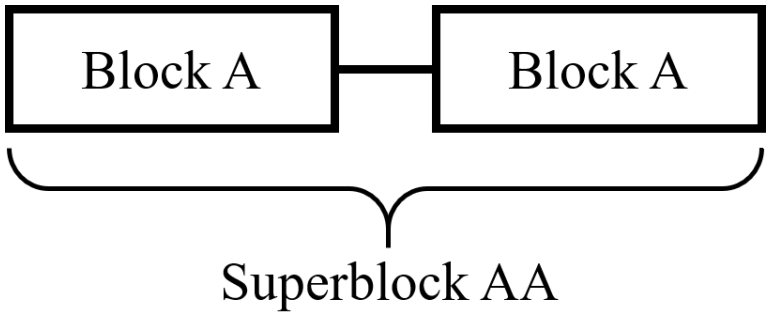

Figure 3.11: Two blocks A combined to form a superblock AA of twice the size.

The new Hamiltonian of the enlarged system is

$$\hat{H}_{\mathrm{AA}} = \hat{H}_{\mathrm{A}}^{\mathrm{left}} \otimes \mathbb{I}^{\mathrm{right}} + \mathbb{I}^{\mathrm{left}} \otimes \hat{H}_{\mathrm{A}}^{\mathrm{right}} + (\text{interaction between blocks}) \qquad (3.32)$$

where $\otimes$ is the tensor product of the Hilbert spaces and $\mathbb{I}$ is the identity matrix with dimension matching the size of the block. Naturally, the Hilbert space dimension of the system also increases after each iteration. In fact, it increases exponentially with each iteration. To solve this problem, truncated diagonalization is proposed where before each iteration, Hamiltonian is diagonalized and only a fixed number of low-lying energy eigenstates is kept. The Hamiltonian is truncated and all the quantum operators are updated with the new truncated basis before the next iteration:

$$\hat{O}_{\mathrm{new}} = \hat{T}^{\dagger} \hat{O}_{\mathrm{old}} \hat{T} \qquad (3.33)$$

where $\hat{T}$ is the truncation matrix whose columns are the kept eigenvectors. This way, the system is studied by iteratively increasing the scale of observation, starting from a block consists of just a single site, giving a renormalization framework. However, the seemingly logical proposition performs poorly for the quantum lattice system in general for two reasons. Firstly, higher energy eigenstates are not necessarily unimportant and may play a role in describing other quantum properties of the ground state system. Second, the combination of two blocks, each already in their ground states, may not result in the ground state of the superblock. Intuitively, two-particles-in-a-box of length $2L$ has different ground state wavefunction and energy compared to the combination of two connected single-particle-in-a-box of length L in their ground states. When the two blocks are combined, the boundary of the connection is neglected but it imposes the wavefunction to be zero at the boundary. This large boundary errors cannot be solved by imposing certain boundary conditions. White and Noack explicitly demonstrated the problems of the NRG with the 1D tight-binding lattice model (White & Noack, 1992).

3.2.2 Traditional Density Matrix Renormalization Group Algorithm

The two problems stated arise due to the neglect of the multipartite quantum entanglement of the system between its subsystems. The two blocks of the superblock are entangled with each other and the ground states of each block combined do not reflect the entanglement between the two blocks. Therefore, in the DMRG, the density matrix is formed at the beginning of each iteration and the SVD, or equivalently the Schmidt Decomposition, is done to select the eigenstates with the highest Schmidt coefficients. To address the second problem, instead of forming new superblock which doubles the size, the superblock is split into the "system" and the "environment", and the new superblock is grown by increasing only single site per block, for both the "system" and "environment", with each iteration. The diagonalization is done at the "system" block without neglecting the "environment" block. This ensures the ground state of the "system" will contribute to the ground state of the entire superblock. These amendments of the algorithm are called the infinite-DMRG (iDMRG) algorithm. It grows the system by two sites per iteration and stops when the desired quantum state of an infinite system, which is the ground state in our case, is obtained. Assuming the system is reflection symmetric, the steps are described as follows:

The infinite-DMRG algorithm:

1. Start with two blocks, each containing a single site, where the left block is the system block, the right block is the environment block.

2. Form two enlarged blocks by adding a single site to the right and left of the system and environment block, respectively.

3. Form the superblock by connecting the system block to the environment block with the following Hamiltonian transformation:

$$\hat{H}_{\text{super}} = \hat{H}_{\text{sys}} \otimes \mathbb{I}_{\text{env}} + \mathbb{I}_{\text{sys}} \otimes \hat{H}_{\text{env}} + (\text{interaction between blocks})$$

4. Diagonalize the superblock to find the targeted state vector $|\psi\rangle$, which can be any desired state that we want to obtain.

5. Form the density matrix of the superblock $\rho_{\text{super}} = |\psi\rangle\langle\psi|$ and then partial trace over the environment to obtain the reduced density matrix of the enlarged system block $\rho_{\text{sys}} = \text{Tr}_{\text{env}}(\rho_{\text{super}})$.

6. Diagonalize ρ_{sys} and order the eigenvectors in descending weight. Keep only the m eigenvectors with the largest weights.

7. Form the truncation operator $\hat{T}$ from the m eigenvectors and project all operators onto this truncated basis: $\hat{O}_{\text{new}} = \hat{T}^{\dagger}\hat{O}_{\text{old}}\hat{T}$

8. Reflect the new system block to obtain the new environment block.

9. Repeat steps 2 to 8 until the algorithm converges.

The one iteration of the infinite-DMRG algorithm is given in Figure 3.12. The truncation error of the observable's expectation value is

$$\left|\langle\hat{O}\rangle - \langle\hat{O}\rangle_{\text{approx}}\right| \leq c_O(1 - \sum_{\alpha=1}^{N-m}\omega_\alpha) \tag{3.34}$$

where N is the total number of eigenstates and $c_O = \max_\alpha\left(\langle\psi_\alpha|\hat{O}|\psi_\alpha\rangle\right)$ is the maximum expectation value of $\hat{O}$ for one of the truncated eigenstates.

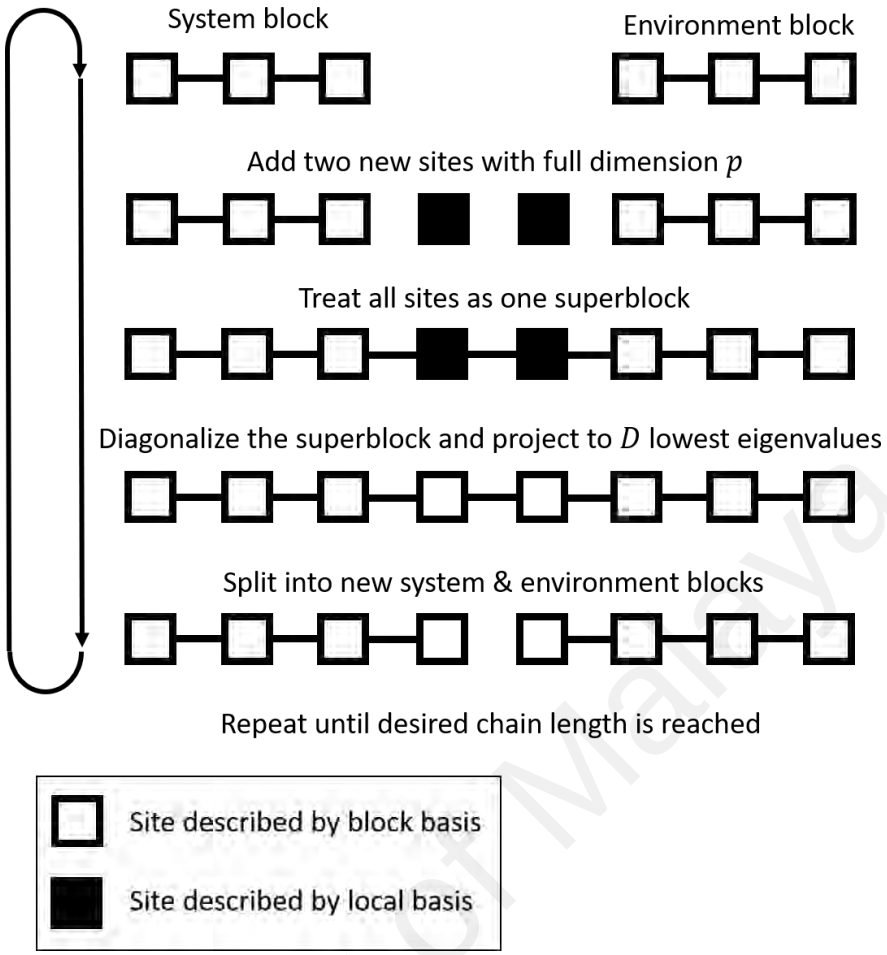

Figure 3.12: Graphical representation of one iteration of the infinite DMRG algorithm.

Next, another variant of the DMRG is the finite-DMRG which sweeps across the spin chain of fixed size to perform the Schmidt Decomposition at every bond. This implies the system block will grow and the environment block shrinks and vice-versa while the size of superblock remains constant. The reason for the sweep is because in iDMRG the superblock is grown from two single-site blocks. The environment block of just a few sites is insufficient to accurately represent the embedding in the final system. Therefore, the finite-DMRG functions to refine the calculation to remove the large "environmental" errors in iDMRG. Assuming the system consists of even number of sites, the finite-DMRG algorithm is described as follows:

The finite-DMRG algorithm:

1. Carry out the steps in iDMRG until the superblock has the desired size L. The system block should have size $l = L/2$ and environment block of size $L - l$. Blocks of all sizes, from $l = 1$ to $l = L/2$, is stored for future use.

2. The sweep begins by growing the system block to size $l + 1$ and retrieve the block of size $L - (l + 2)$ from storage to be reflected to get an environment block. Grow the environment block to size $L - (l + 1)$.

3. Carry out the steps 3 to 7 of the iDMRG algorithm.

4. Store the truncated block as the new block.

5. Set $l = l + 1$.

6. Repeat the steps 2 to 5 until $l = L/2 - 2$. Then, set $l = 1$ and retrieve a block of size 1 as the new system block.

7. Repeat the steps 2 to 5 until $l = L/2$ and this concludes a single "sweep".

8. Repeatedly sweep over the system (steps 2 to 7) until the algorithm converges.

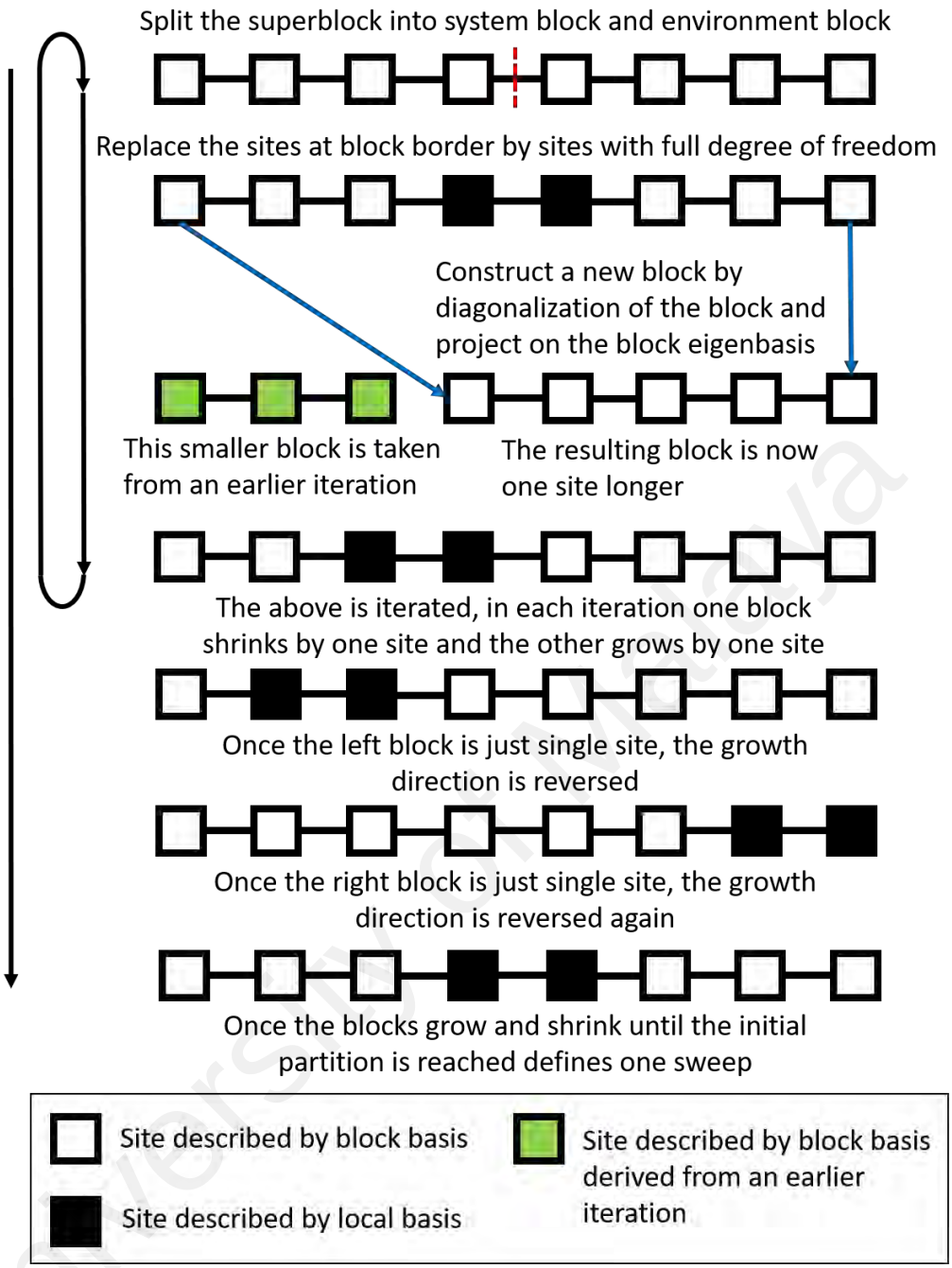

Figure 3.13: Graphical representation of one sweep of the finite DMRG algorithm.

3.2.3 The Modern Density Matrix Renormalization Group Algorithm

The DMRG, which iteratively optimizes the wavefunction one site at a time, will naturally produce wavefunction in the form of MPS. Therefore, conversely, the MPS can be made as a wavefunction ansatz and apply DMRG to it (Schollwöck, 2011). The modern DMRG in the context of MPS is a variational optimization algorithm which is

essentially the method of compression described in Section 3.1.3. The energy of an unnormalized MPS is given by:

$$E = \frac{\langle\psi|\hat{H}|\psi\rangle}{\langle\psi|\psi\rangle} \tag{3.35}$$

Therefore, to find the ground state of the system one needs to minimize (3.35) with respect to the wavefunction:

$$E_0 = \min_{\psi}\left(\langle\psi|\hat{H}|\psi\rangle - E\langle\psi|\psi\rangle\right) \tag{3.36}$$

This is done by setting the gradient of $\langle\psi|\hat{H}|\psi\rangle - E\langle\psi|\psi\rangle$ to zero

$$\begin{aligned}
&\frac{\partial}{\partial A^{\sigma_i *}}\langle\psi|\hat{H}|\psi\rangle - E\langle\psi|\psi\rangle = \\
&\textstyle\sum_{\boldsymbol{\sigma}^*}(A^{\sigma_1 *}\dots A^{\sigma_{i-1} *})_{1,a_{i-1}}\,(A^{\sigma_{i+1} *}\dots A^{\sigma_L *})_{a_i,L}\left(W^{\sigma_1\sigma_1'}\dots W^{\sigma_i\sigma_i'}\dots W^{\sigma_L\sigma_L'}\right)\times \\
&(A^{\sigma_1}\dots A^{\sigma_i}\dots A^{\sigma_L}) - \\
&E\textstyle\sum_{\boldsymbol{\sigma}^*}(A^{\sigma_1 *}\dots A^{\sigma_{i-1} *})_{1,a_{i-1}}(A^{\sigma_{i+1} *}\dots A^{\sigma_L *})_{a_i,L}(A^{\sigma_1}\dots A^{\sigma_i}\dots A^{\sigma_L}) = 0
\end{aligned} \tag{3.37}$$

where $\boldsymbol{\sigma}^*$ refers to sum over all indices except those connected to $A^{\sigma_i *}$. The result of (3.37) is diagrammatically represented in Figure 3.14:

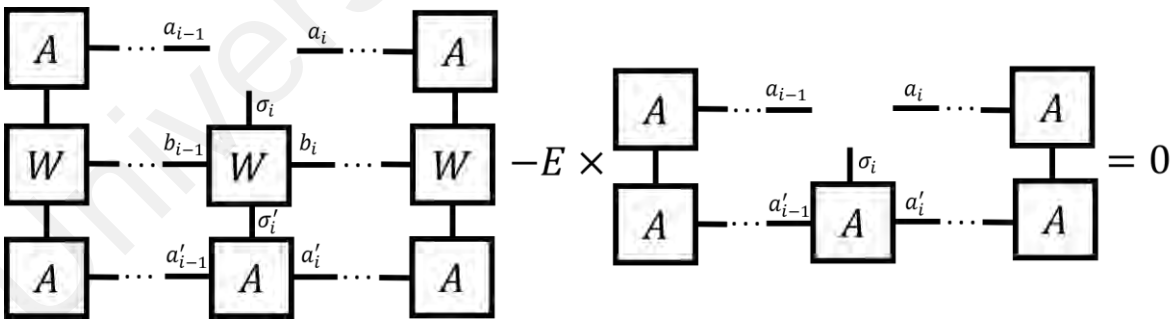

Figure 3.14: Diagrammatic representation of minimizing $\langle\psi|\hat{H}|\psi\rangle - E\langle\psi|\psi\rangle$.

Next, (3.37) can be simplified by grouping all other tensors except A^{σ_i} as large tensor:

$$\textstyle\sum_{\sigma_i',a_{i-1}',a_i'}\tilde{H}^{\sigma_i\sigma_i'}_{a_{i-1}'a_i'a_{i-1}a_i}A^{\sigma_i'}_{a_{i-1}'a_i'} = E\sum_{a_{i-1}',a_i'}\tilde{O}_{a_{i-1}'a_i'a_{i-1}a_i}A^{\sigma_i}_{a_{i-1}'a_i'} \tag{3.38}$$

By reshaping A^{σ_i} as a vector $\vec{v}$, $\tilde{H}$ as a matrix $\boldsymbol{H}$ and $\tilde{O}$ as a matrix $\boldsymbol{P}$, we get

$$\boldsymbol{H}\vec{v} = E\boldsymbol{P}\vec{v} \tag{3.39}$$

which is again a problem that can be solved with linear algebra methods. The conversion of (3.38) to (3.39) is diagrammatically shown in Figure 3.15.

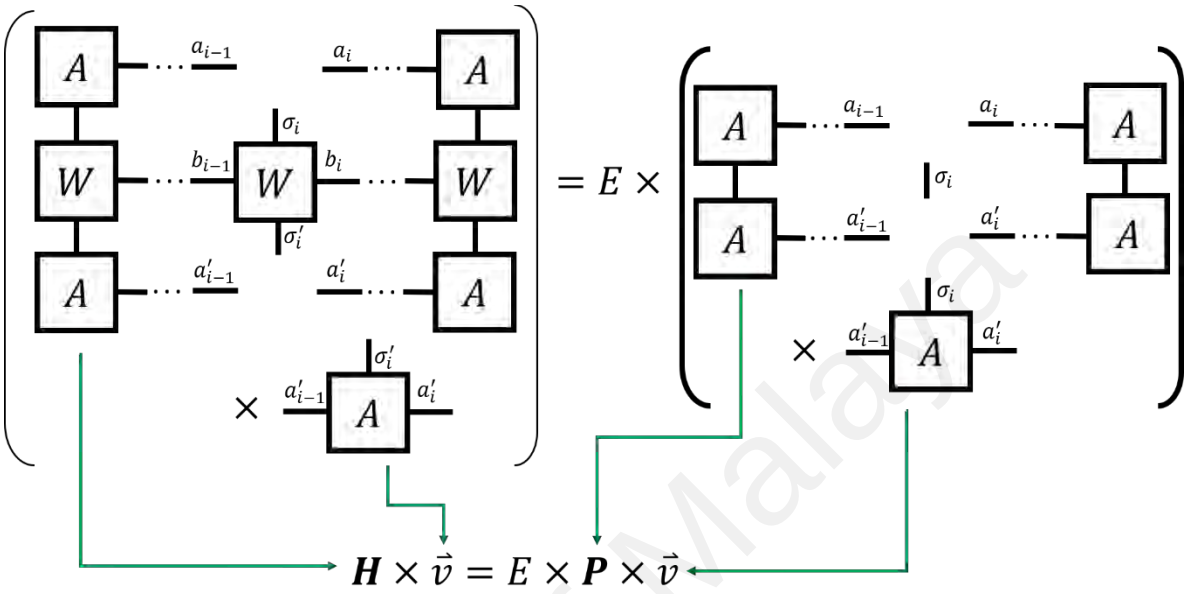

Figure 3.15: Diagrammatic representation of expression (3.38) and (3.39).

Again, if the MPS is in the mix-canonical form with site i as orthogonality center, $\boldsymbol{P}$ becomes an identity matrix, simplifying (3.39) to be an eigenvalue problem:

$$\boldsymbol{H}\vec{v} = E\vec{v} \tag{3.40}$$

Solving for $\vec{v}$, the elements of tensor A^{σ_i} at site i is obtained. After the procedures are repeated for all sites, one "sweep" is said to be completed. Multiple sweeps can be done to improve the result since $\boldsymbol{H}$ depends on the "environment" tensors and they are all re-evaluated after one "sweep".

In conclusion, the modern DMRG essentially treat one tensor as a variational parameter at a time while keeping the "environment" constant, and iteratively compress the MPS with respect to a targeted quantum operator in MPO form. In our case, the quantum operator is the Hamiltonian of the tQIM and the resultant MPS represents the

ground state of the system. The calculations in this thesis are done using the modern DMRG algorithm via the ITensor C++ library package available at itensor.org.

3.3 Finite-Size Scaling Theory

For the phase transition to occur, the system size must be infinite to produce divergence of the response functions, such as magnetization, magnetic susceptibility, and specific heat capacity. However, for numerical simulations without imposing certain boundary conditions one can only study a system of finite sizes. The availability of real finite-size systems due to optical and magnetic traps makes numerical simulations and studies essential. As mentioned in Chapter 2, the phase transition happens at the critical point is essentially due to the divergence of the correlation length. As the transverse field is getting closer to the critical point, the correlation increases without bound and diverges at the critical point. However, for a finite system, the correlation is bounded by the size of the system. Before the critical point, the entire bulk of spins are strongly correlated due to $\xi \approx L$ and undergoes a pseudo-phase transition. It is not a real phase transition because the response functions are not divergent but still the order parameter changes from non-zero to zero and vice versa across the pseudo-critical point. The finite-size scaling (FSS) ansatz proposes that the thermodynamic quantities scale relative to the system size and the correlation length near the critical point.

For an arbitrary thermodynamic quantity Ω near the critical point, it has the following asymptotic behaviour:

$$\Omega \sim |\epsilon|^{-\omega} \tag{3.41}$$

where ω is the critical exponent of quantity Ω and ϵ is the distance from the critical point. By substituting the scaling relation of correlation length from (2.9) into (3.41) Ω diverges with the correlation length ξ following the relation:

$$\Omega \sim \xi^{\omega/\nu} \tag{3.42}$$

The only relevant length scale near the critical point is the correlation length. Since the correlation length is bounded by the system size, the thermodynamic behaviour is restricted by the system size L. The deviation of behaviour from the thermodynamic limit depends on the ratio ξ/L. (3.42) is scaled by a dimensionless scaling function to accommodate this observation:

$$\Omega \sim \xi^{\omega/\nu}\Omega_0(L/\xi) \tag{3.43}$$

where $\Omega_0(x)$ is the scaling function with the following asymptotic properties:

$$\lim_{x\to\infty} \Omega_0(x) = \text{const.} \tag{3.44}$$

and

$$\lim_{x\to 0} \Omega_0(x) \sim x^{\omega/\nu} \tag{3.45}$$

Equation (3.44) and (3.45) represent the limiting behaviour of infinite system size and finite-size effect respectively. When the correlation length is much smaller compared to the system size, (3.43) is preserved. Contrary, when the correlation length outgrows the system size, finite-size scaling occurs and Ω scales with system size L. In principle, (3.43) contains all the information needed to describe finite-size effects. However, in practice, we rarely know the correlation length ξ at temperature T in the infinite system. Therefore, it is convenient, and conventional, to reorganize the equation by defining a new dimensionless function $\widetilde{\Omega}$:

$$\widetilde{\Omega}(x) = x^{-\omega}\Omega_0(x^{\nu}) \tag{3.46}$$

where $\widetilde{\Omega}(x)$ follows similar behaviour to $\Omega_0(x)$. After substitution of (3.46) into (3.43), we get

$$\Omega = L^{\omega/\nu}\widetilde{\Omega}\left(L^{1/\nu}|\epsilon|\right) \tag{3.47}$$

At the critical point, (3.47) reveals the scaling behaviour of Ω with the system size L:

$$\Omega|_{h_c} \sim L^{\omega/\nu} \tag{3.48}$$

For an arbitrary thermodynamic quantity Ω with critical exponent ω, the finite-size scaling allows one to calculate the critical exponent by determining Ω at the critical point for various system sizes.

CHAPTER 4: RESULTS & DISCUSSION

In this chapter, first, the numerical simulation is benchmarked with the known analytical results to demonstrate its validity. Next, we show that the critical point is determined using the Binder's cumulant and each selected critical exponent is calculated from the respective thermodynamic quantity of various system sizes at the critical point. The finite-size effects of the thermodynamic quantities in both open and periodic boundary conditions are also discussed. Finally, the effect of noisy coupling strength on the thermodynamic parameters is shown. Observations such as faster phase transition before the critical point and transition to disordered spin glass phase above certain noise levels are discussed.

4.1 Benchmark of Numerical Simulation with Analytical Results

The analytical solution of the 1D quantum Ising model is well known and serves as a benchmark for many other models which slightly departs from it such as those with next-nearest-neighbour couplings but still short-ranged models. Here we benchmark our numerical simulation of 100 spins in open boundary condition (OBC) with the analytical solutions from equation (2.16), (2.17) and (2.18). Besides, the mean-square longitudinal magnetization and magnetic susceptibility are also calculated. The formulas are explicitly given in Table 4.1:

Table 4.1: Mathematical expressions for thermodynamic quantities.

Ground state energy per spin, $\langle E_0 \rangle$	$\langle E_0 \rangle = \left\langle \psi \middle\vert \left(\frac{1}{L} \sum_i -J \hat{S}_i^z \hat{S}_{i+1}^z - h \hat{S}_i^x \right) \middle\vert \psi \right\rangle$
Longitudinal magnetization, $\langle M_z \rangle$	$\langle M_z \rangle = \left\langle \psi \middle\vert \left(\frac{1}{L} \sum_i \hat{S}_i^z \right) \middle\vert \psi \right\rangle$
Mean-square longitudinal magnetization, $\langle M_z^2 \rangle$	$\langle M_z^2 \rangle = \left\langle \psi \middle\vert \left(\frac{1}{L} \sum_i (\hat{S}_i^z)^2 \right) \middle\vert \psi \right\rangle$
Transverse magnetization, $\langle M_x \rangle$	$\langle M_x \rangle = \left\langle \psi \middle\vert \left(\frac{1}{L} \sum_i \hat{S}_i^x \right) \middle\vert \psi \right\rangle$
Longitudinal magnetic susceptibility, χ_z	$\chi_z \propto L^2 (\langle M_z^2 \rangle - \langle M_z \rangle^2)$

where for a d-dimensional quantum system, the magnetic susceptibility χ_z is defined as:

$$\chi_z \propto L^{(d+z)}(\langle M_z^2 \rangle - \langle M_z \rangle^2) \quad (4.1)$$

The exponent z is the dynamical critical exponent. For the transverse field quantum Ising model, $z = 1$ (Sachdev, 2011). Therefore, (4.1) for 1D quantum Ising model is reduced to

$$\chi_z \propto L^2(\langle M_z^2 \rangle - \langle M_z \rangle^2) \quad (4.2)$$

Note that the wavefunctions and operators in Table 4.1 are in MPS and MPO form respectively. The calculation is the contraction of $\langle \mathrm{MPS}|\mathrm{MPO}|\mathrm{MPS} \rangle$ tensor networks. The benchmarks are plotted in Figure 4.1 to 4.3.

Referring to Figure 4.1, the simulation results obtained for ground state energy conforms reasonably well with the analytic solution. For longitudinal magnetization, the simulation drops to zero sooner than expected, that is, before the critical point, $h_c = 0.5$. This is due to the finite-size effect of 100 spins simulation and it drops to zero at $h = 0.49$, which is the pseudo-critical point of the finite-size system. Lastly, the simulation results for transverse magnetization also fit reasonably well with the analytic solution. However, notice the very small deviation around the pseudo-critical point. This is because at the critical point, the correlation of the system, in the form of entanglement entropy, diverges and the system does not follow the Area Law. As the system approaches the critical point, the entanglement entropy slowly deviates from the Area Law. Since the MPS and DMRG are methods whose advantage lies in the validity of the Area Law, the deviation is reasonable. This also shows that MPS can approximate the wavefunction very well at the critical point, with the fact that the entanglement entropy scales only with the log of system size: $S(L) \sim \log(L)$.

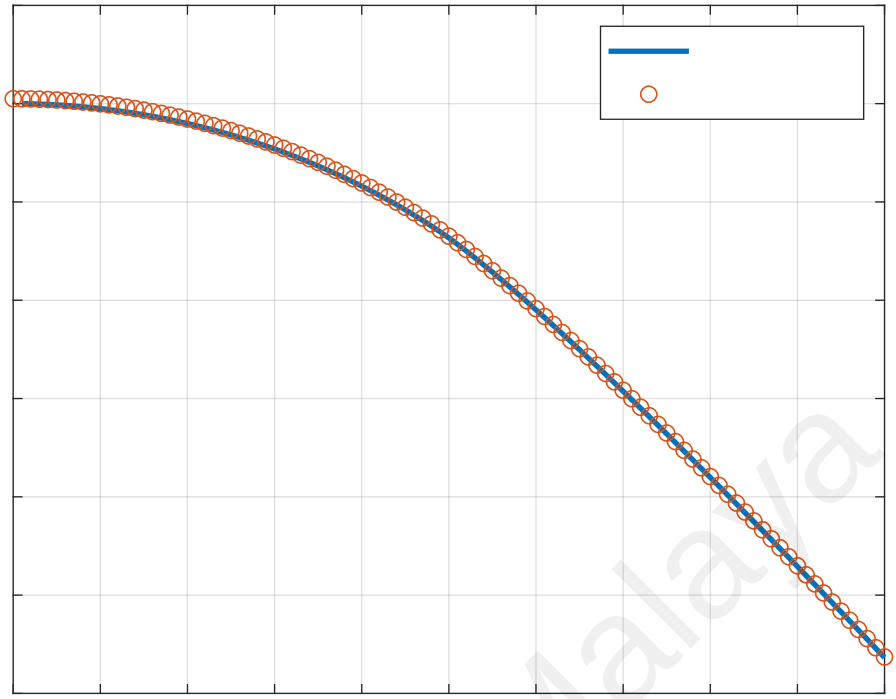

Figure 4.1: Benchmarking simulation results with analytic solution (Pfeuty, 1970) for ground state energy, $\langle E_0 \rangle$.

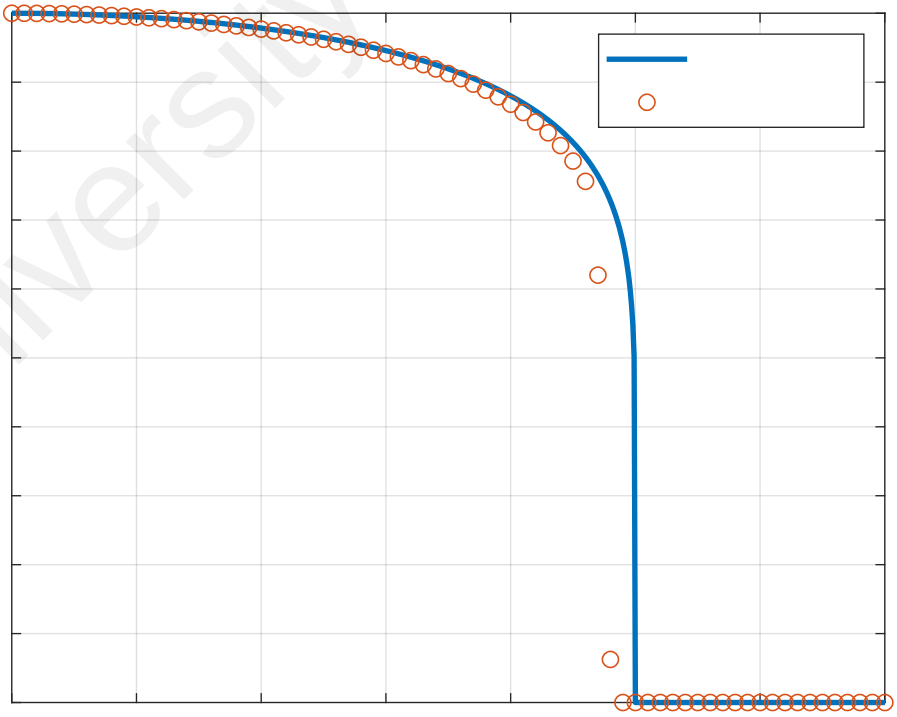

Figure 4.2: Benchmarking simulation results with analytic solution (Pfeuty, 1970) for longitudinal magnetization, $\langle M_z \rangle$.

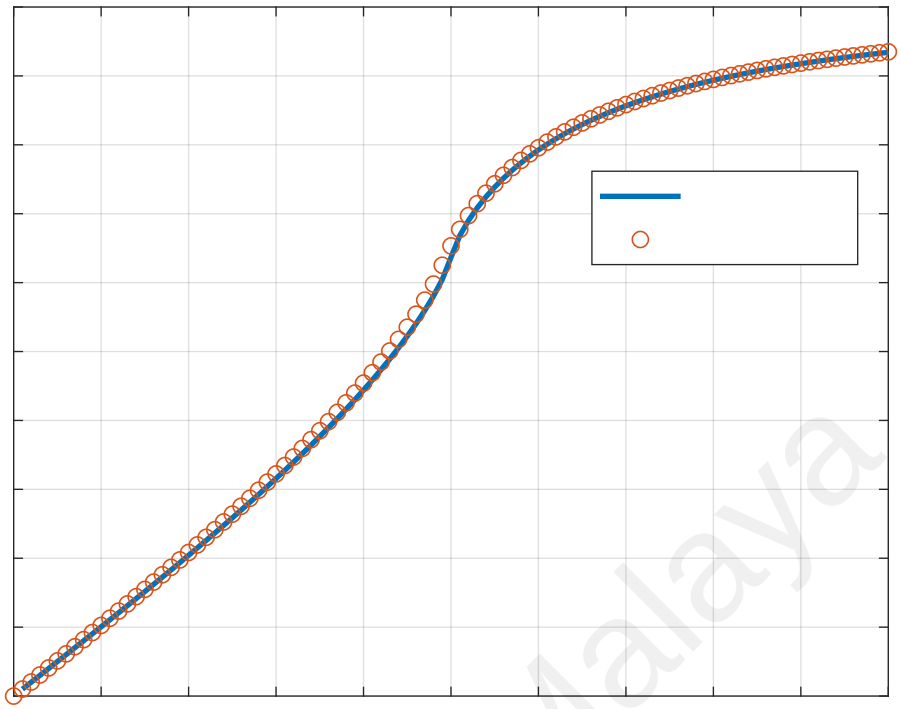

Figure 4.3: Benchmarking simulation results with analytic solution (Pfeuty, 1970) for transverse magnetization, $\langle M_x \rangle$.

4.2 Determination of Critical exponents

The finite-size scaling theory described in Section 3.3 allows one to extract the critical exponent corresponding to its thermodynamic parameter if we know the finite-size values of the parameter at the critical point. With that knowledge, one may plot the log-log graph of thermodynamic quantity at the critical point and system size and obtain the ratio of exponents from the gradient of the plot according to (3.48).

4.2.1 Binder's 4th Order Reduced Cumulant

However, in order to use (3.48) to determine the critical exponents, we need to know the exact location of the critical point. The Binder's 4th order reduced cumulant U_L, defined as follows, is invariant with the system size L (Binder, 1990):

$$U_L = 1 - \frac{\langle \phi^4 \rangle_L}{3\langle \phi^2 \rangle_L^2} \tag{4.3}$$

where $\langle \phi^4 \rangle_L$ and $\langle \phi^2 \rangle_L$ are the 4th and 2nd moments of the order parameter of system size L. For our case, where the longitudinal magnetization M_z is the order parameter, the Binder's cumulant is defined as:

$$U_L = 1 - \frac{\langle M_z^4 \rangle_L}{3\langle M_z^2 \rangle_L^2} \tag{4.4}$$

It follows from the finite-size scaling ansatz that the ratio $\langle M_z^4 \rangle_L / \langle M_z^2 \rangle_L^2$ is not dependent on the system size at the critical point:

$$\frac{\langle M_z^4 \rangle_L|_{h_c}}{\langle M_z^2 \rangle_L^2|_{h_c}} \sim \frac{L^{-4\beta/\nu}}{(L^{-2\beta/\nu})^2} = \text{const.} \tag{4.5}$$

Therefore, determining the crossing of U_L for various system sizes is a very reliable method to determine the critical point (Godoy & Figueiredo, 2002; Merdan & Erdem, 2004; Hasenbusch, 2008).

4.2.2 Finite-size Effects on Thermodynamic Parameters

In this study, the simulations are done for 6 system sizes of 20, 40, 60, 80, 100 and 120 spins for both open boundary condition (OBC) and periodic boundary condition (PBC). The Binder's cumulant and average thermodynamic quantities such as the ground state energy, longitudinal magnetization and its root-mean-square (r.m.s.), transverse magnetization, and the magnetic susceptibility, whose expressions are listed in Table 4.1, are calculated across the whole range of transverse field and plotted in Figure 4.4 to 4.9 respectively. Besides, the two-point correlation at the critical point is also calculated. To determine the thermodynamic critical point, the Binder's cumulant U_L is plotted for various system sizes. By inspecting the intersection of both plots (Figure 4.4), the critical point is uniquely determined to be $h_c = 0.5$. This agrees exactly with the prediction of the analytic solution.

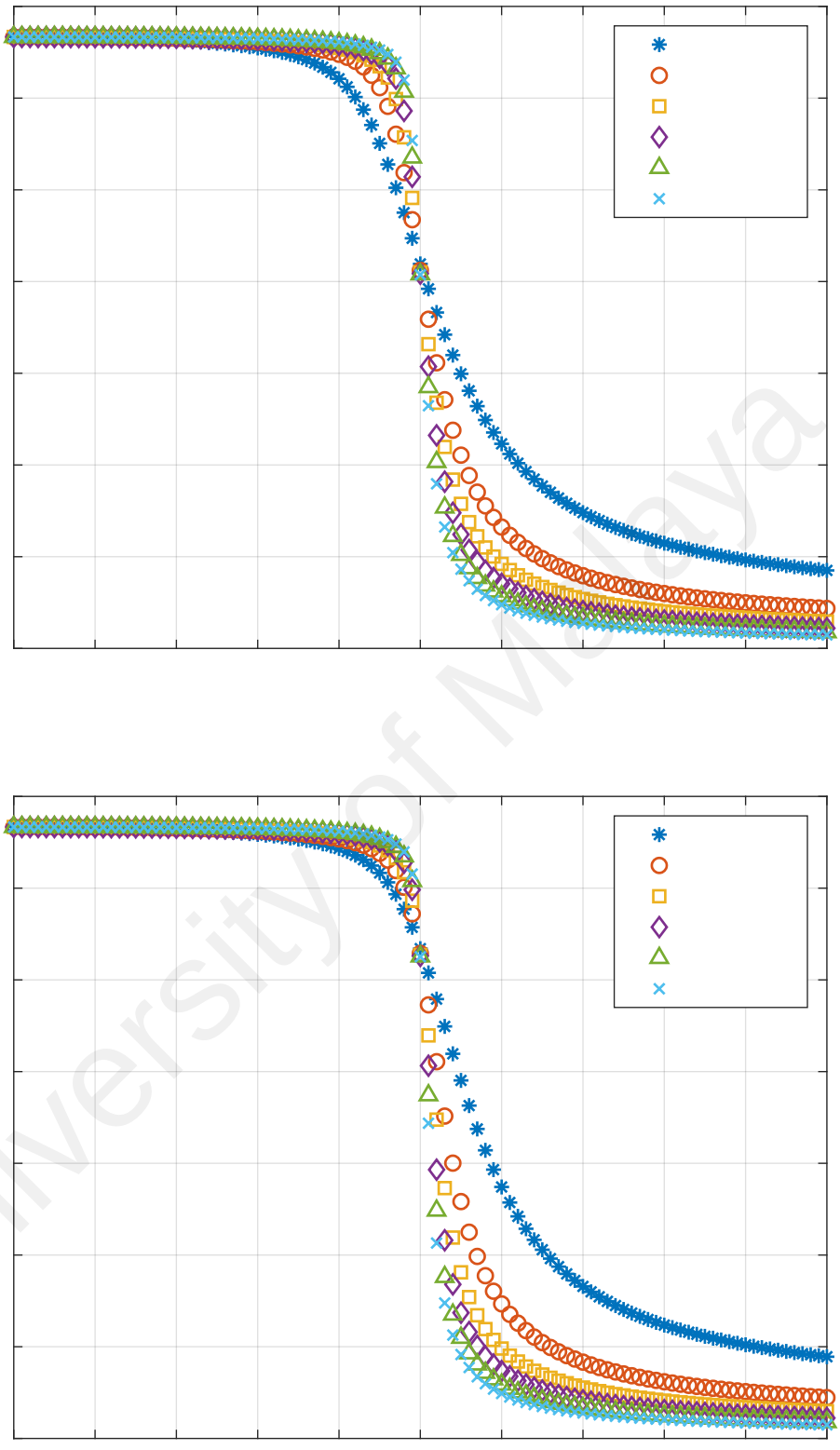

Figure 4.4: Binder's cumulant vs transverse field strength with increasing system size. OBC (top) and PBC (bottom). The intersection happens at $h = 0.5$ for both boundary conditions.

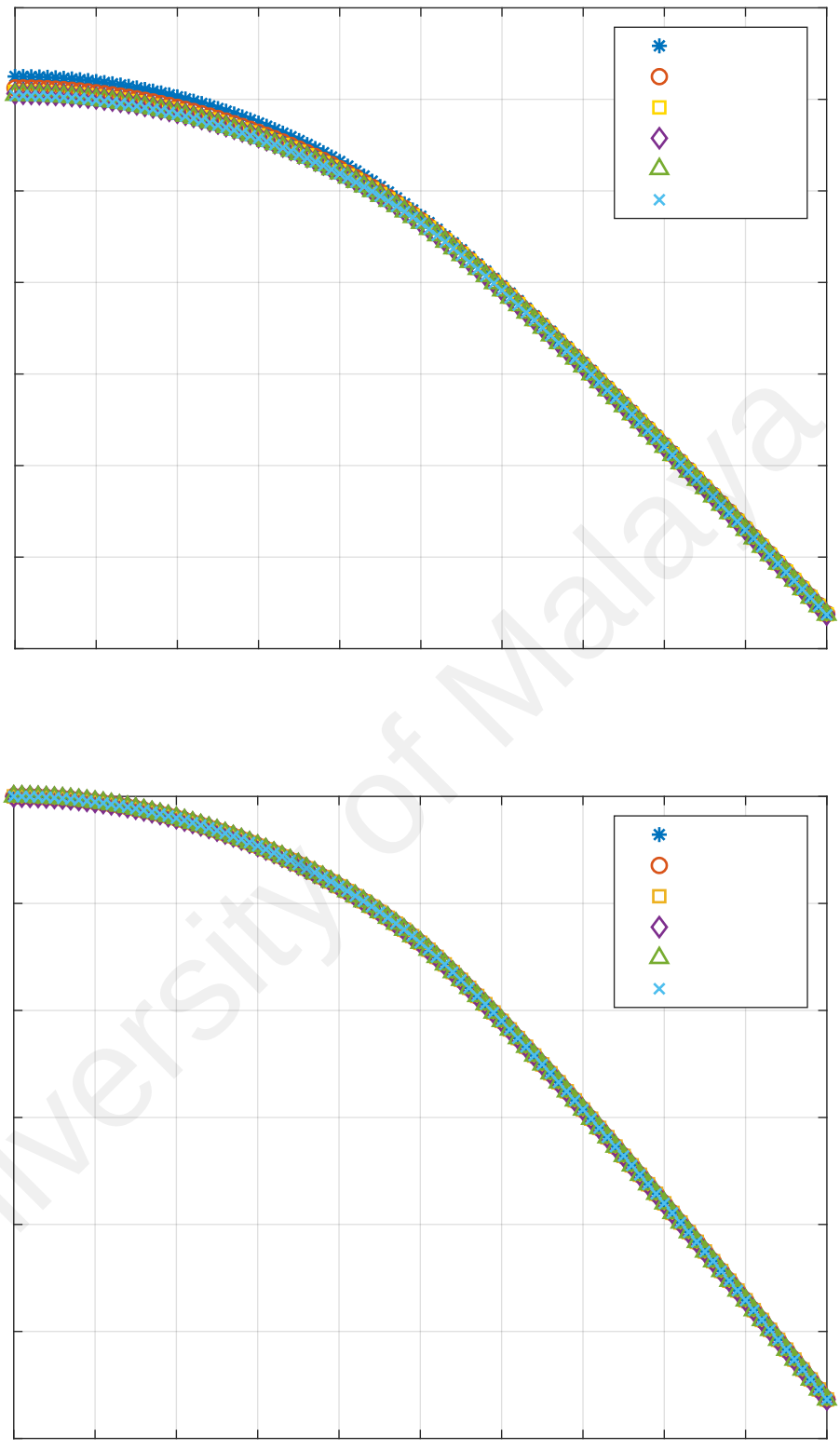

Figure 4.5: Ground state energy vs transverse field strength with increasing system size. OBC (top) and PBC (bottom).

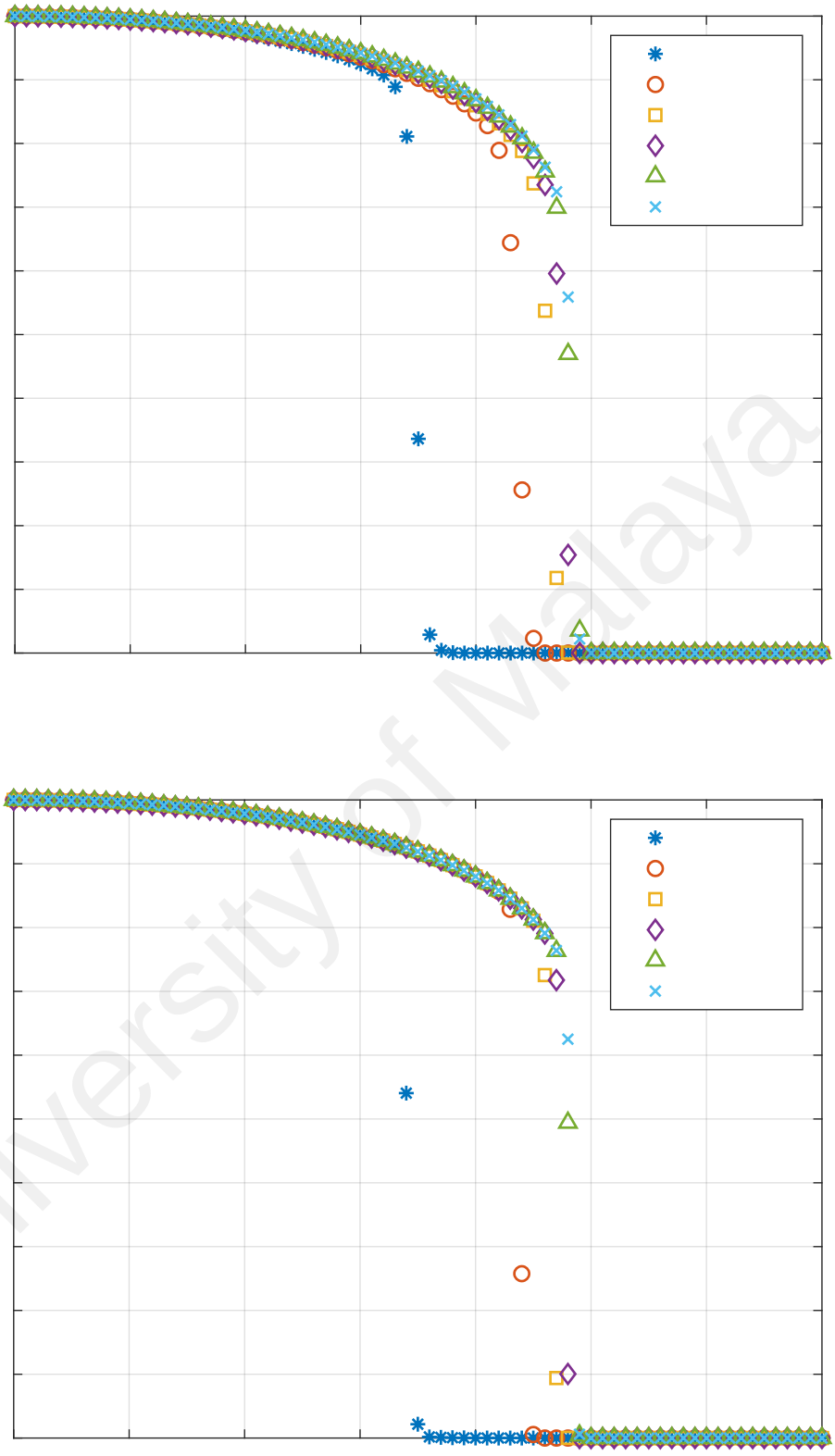

Figure 4.6: Longitudinal magnetization vs transverse field strength for various system sizes. OBC (top) and PBC (bottom).

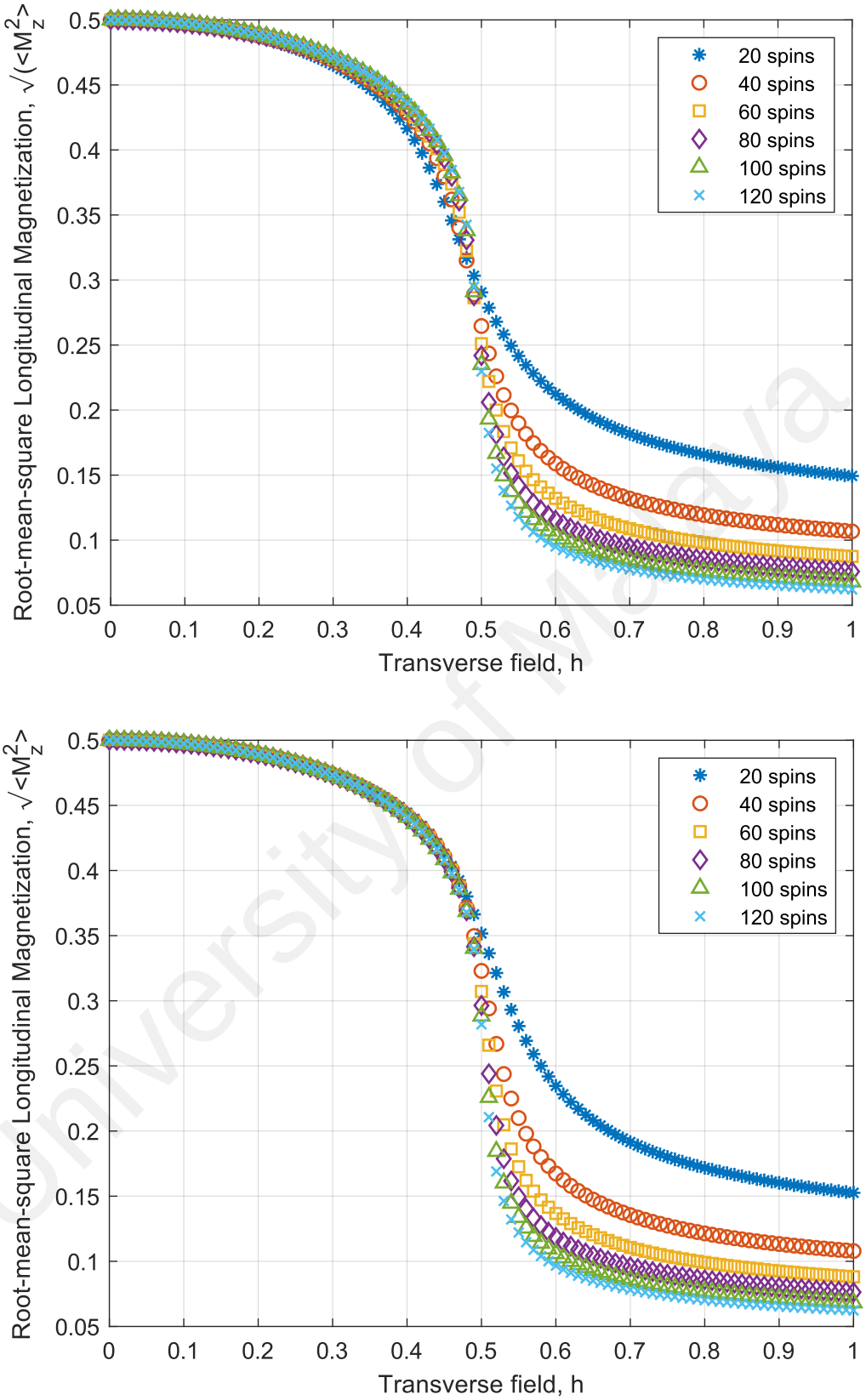

Figure 4.7: Root-mean-square longitudinal magnetization vs transverse field strength for various system sizes. OBC (top) and PBC (bottom).

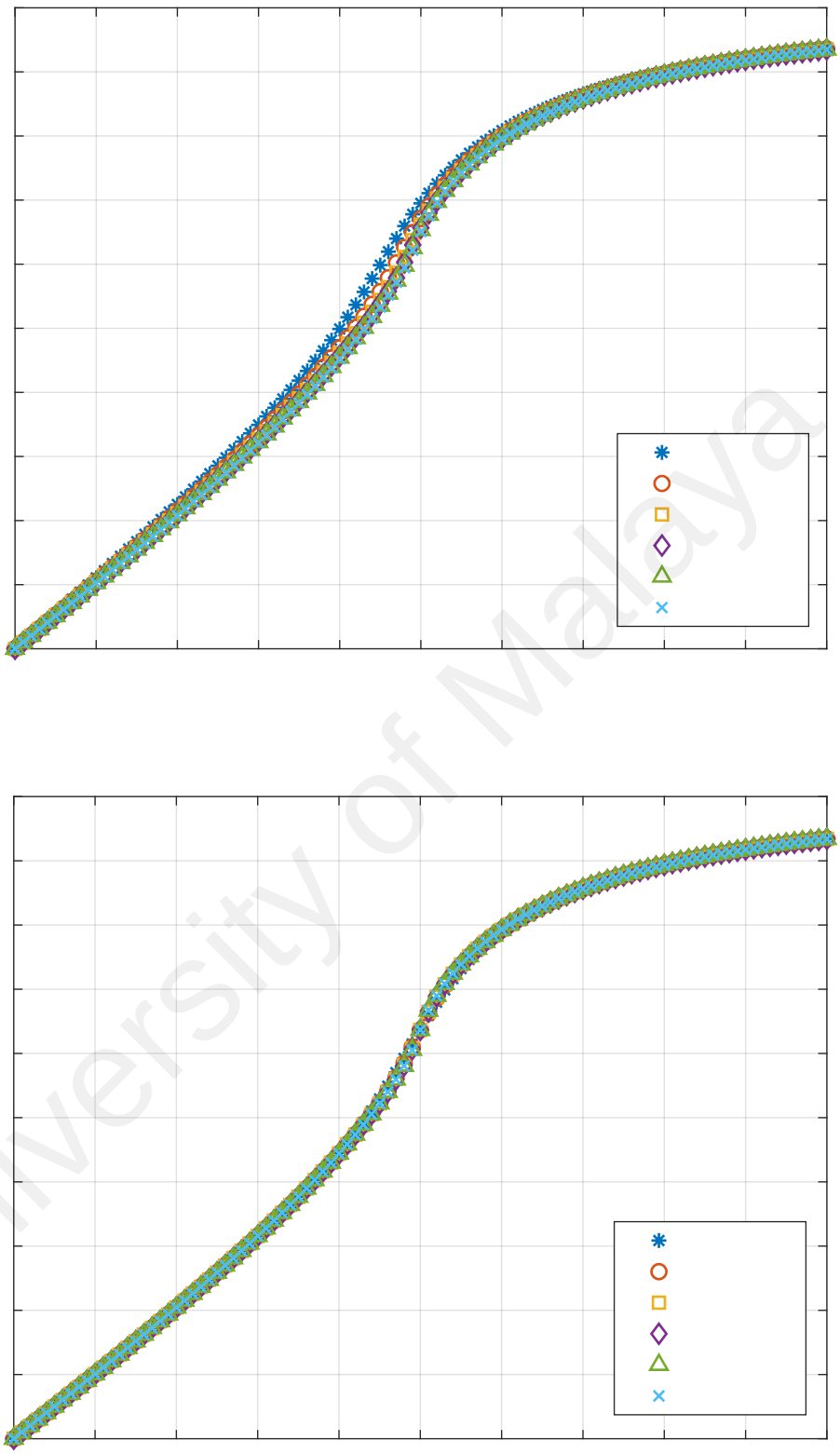

Figure 4.8: Transverse magnetization vs transverse field strength for various system sizes. OBC (top) and PBC (bottom).

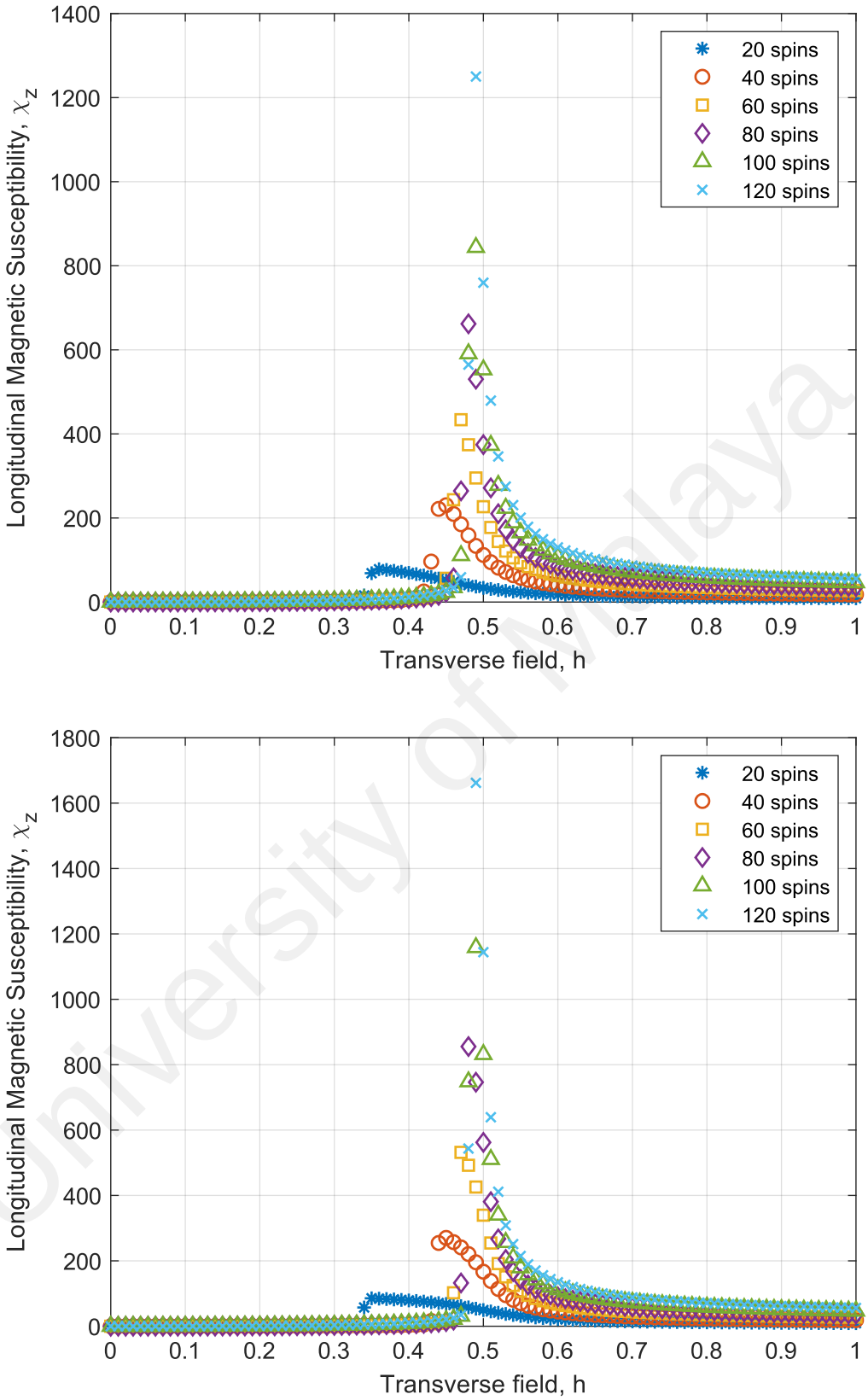

Figure 4.9: Magnetic susceptibility vs transverse field strength for various system sizes. OBC (top) and PBC (bottom).

In general, the differences in thermodynamic quantities between OBC and PBC are due to the difference in correlation of the entire system. For OBC, for the whole system to be correlated, the correlation length must grow to approximately the system size: $\xi \sim L$. While for PBC, $\xi \sim L/2$ because the system forms a chain and, thus, the correlation builds up from both sides. Therefore, the thermodynamic parameters of systems with OBC exhibit deviations near the critical point where systems of different sizes achieve full correlations at different pseudo-critical fields. The average thermodynamic quantities are intensive quantities. For average ground state energy, this is clearly observed in PBC case where the plots all converge into single plot for all sizes. However, at small transverse fields far away from the critical point, the plots for OBC slowly deviates from -0.25 for decreasing system size. The increase in energy or equivalently the decrease in the magnitude of the energy with decreasing system size is due to the lack of $-J\hat{S}_1^z\hat{S}_L^z$ coupling term in the Hamiltonian. As transverse field increases, the weightage of the coupling terms in Hamiltonian gradually loses out to the transverse terms. Therefore, the deviation vanishes for large transverse fields and only obvious for small fields. Besides, the deviation in energy reduces with increasing system size is due to the division of $-J\hat{S}_1^z\hat{S}_L^z$ by an increasingly larger number in the averaging calculation.

From Figure 4.6, the longitudinal magnetization as the order parameter drops to zero, indicating a phase transition at the corresponding critical transverse field. A phase transition occurs when the entire system becomes fully correlated, that is the correlation length is longer than the system size: $\xi > L$, resulting in all spins effectively pointing in the longitudinal directions. Therefore, smaller system achieves full correlation at smaller transverse field and undergoes pseudo-phase transition sooner. In addition, systems in PBC undergo phase transition sooner than in OBC for the same reason of achieving full correlation at lower critical fields than in OBC. The r.m.s. longitudinal magnetizations also showed similar behaviour, but it does not drop to zero after the critical point. This is

because the randomized spins are individually squared before summed up for averaging. Note that the larger system has lower r.m.s. magnetization because the averaged quantity is divided by a greater number of spins. Besides, to obtain the critical exponents using the finite-size scaling theory, non-zero values of thermodynamic parameters at the critical point are required. Thus, the r.m.s. magnetizations are included for future calculation of critical exponent.

Next, the finite-size effects are not that obvious for transverse magnetization. For PBC, there seems to have no finite-size effects on the average quantity. This means at each transverse field, the system's overall correlation is the same for all sizes. For OBC, there is deviation at the point of inflection, also due to the difference in attaining full correlation at different critical fields. From Figure 4.9, we can observe that the peak of longitudinal magnetic susceptibility, whose corresponding transverse field is the pseudo-critical point, gradually shifts to the left with decreasing system size. This is consistent with the previous observation of sooner phase transition for smaller systems from longitudinal magnetization. However, note that the heights of the peaks for PBC is always higher than OBC for every system size. This is due to higher total correlation of the system in PBC.

4.2.3 Critical Exponents

To extract the critical exponents, we use the thermodynamic parameters calculated from periodic boundary conditions (PBC). The advantage of studying an Ising ring is to eliminate the edge effects and solely study the finite-size effects. The critical exponents which are independently calculated are β/ν, γ/ν and η. Since the longitudinal magnetization of small system sizes drops to zero before the critical point, (3.48) cannot be applied. Instead, to obtain the critical exponent β we use the r.m.s. magnetization as the order parameter and it obeys the following relation:

$$\sqrt{\langle M_z^2 \rangle}|_{h_c} \sim L^{-\beta/\nu} \tag{4.6}$$

By plotting log-log graph, we determine the ratio $\beta/\nu = 0.1235(1)$ (see Figure 4.10). This is in good agreement with $\beta = 0.125$ if we assume $\nu = 1$.

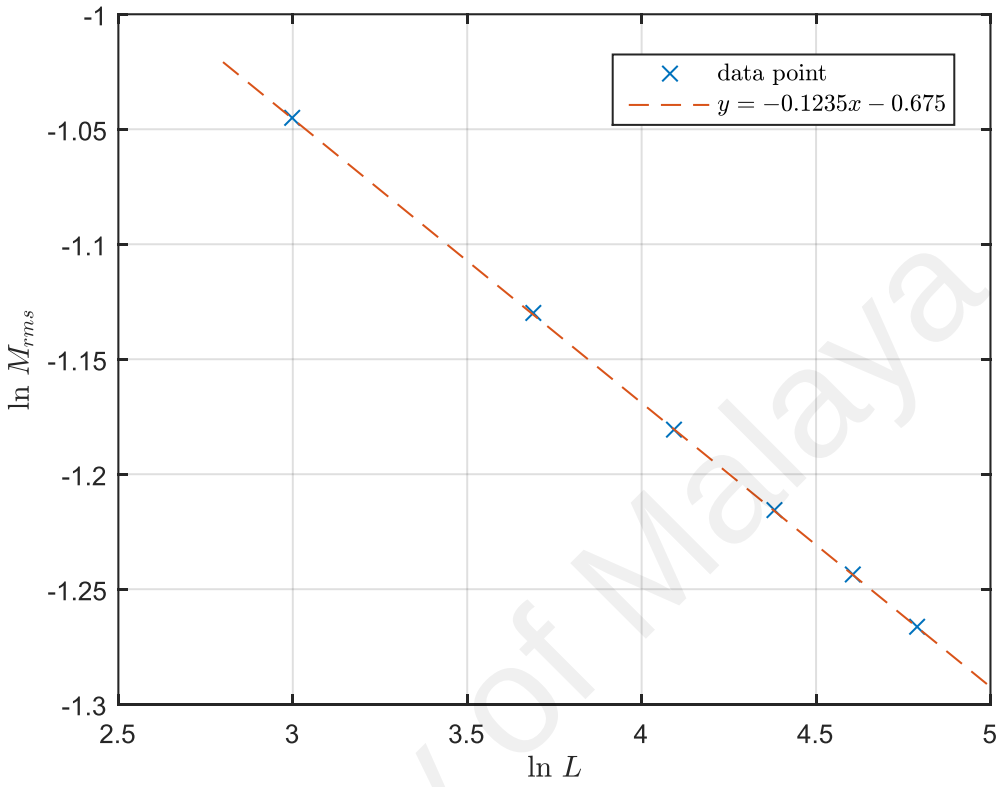

Figure 4.10: Log-log plot of root-mean-square magnetization $\sqrt{\langle M_z^2 \rangle}$ at h_c vs system size L.

Next, the critical exponent γ is obtained from the log-log plot of magnetic susceptibility (see Figure 4.11) because it obeys the following relation:

$$\chi_z|_{h_c} \sim L^{\gamma/\nu} \tag{4.7}$$

The ratio is determined to be $\gamma/\nu = 1.7351(3)$. This is, again, with good agreement with $\gamma = 1.75$ if we assume $\nu = 1$.

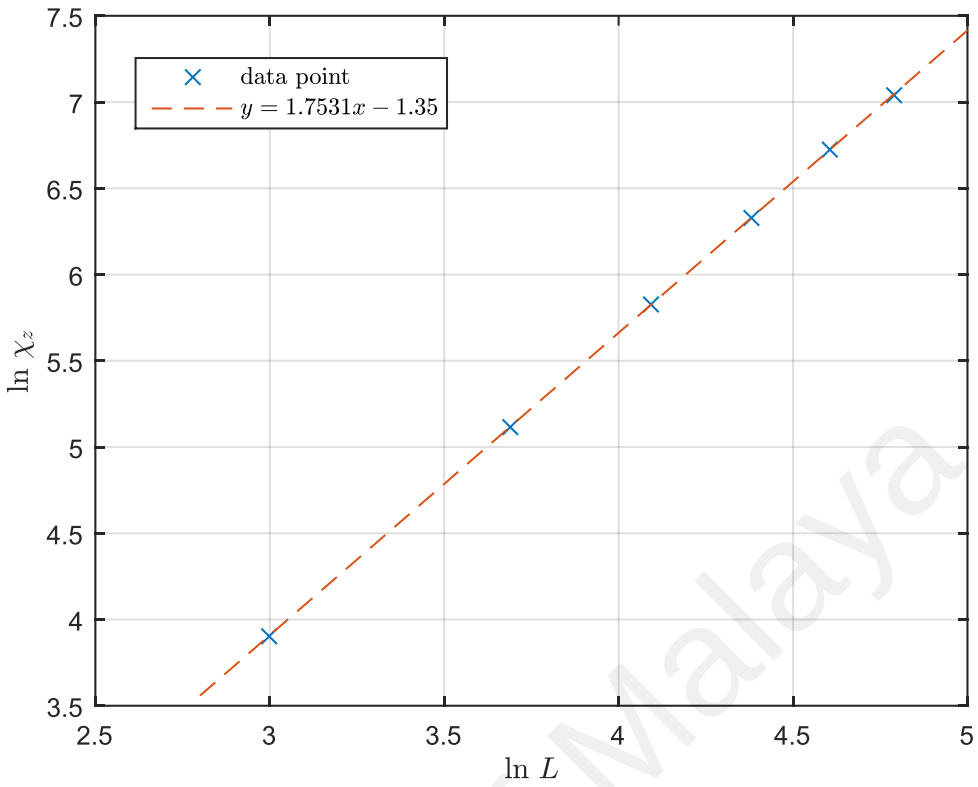

Figure 4.11: Log-log plot of magnetic susceptibility χ_z at h_c vs system size L.

Finally, the critical exponent η cannot be determined by applying (3.48) because η is defined only at the critical point. However, for periodic boundary condition and close to the critical point, the two-point correlation function $G(r)$ at distance r obeys the following expression:

$$G(r,L) \propto \frac{1}{r^{d-2+\eta}} + \frac{1}{(L-r)^{d-2+\eta}} \quad , r \gg 1 \tag{4.8}$$

It is the sum of two terms because the correlation builds up from both sides of the ring. As (4.8) is not a simple power law, one cannot extract the critical exponent η by plotting the log-log graph. However, G obeys the following finite-size scaling ansatz (Zhang et. al., 2018):

$$G(r,\epsilon,L) \propto |r|^{-(d-2+\eta)} \tilde{G}(r/L, \epsilon L^{1/\nu}) \tag{4.9}$$

At the critical point, the scaling function is only a function of the ratio r/L.

$$G(r,L)|r|^{(d-2+\eta)} \propto \tilde{G}(r/L) \tag{4.10}$$

Therefore, by plotting $G(r,L)|r|^{(d-2+\eta)}$ vs r/L with the correct value of η, one expects plots of various sizes to collapse into the same graph. We plotted with multiple guesses of η around $\eta = 0.250$, its theoretical value. Finally, the plots collapse the best for $\eta = 0.249$ as shown in Figure 4.12.

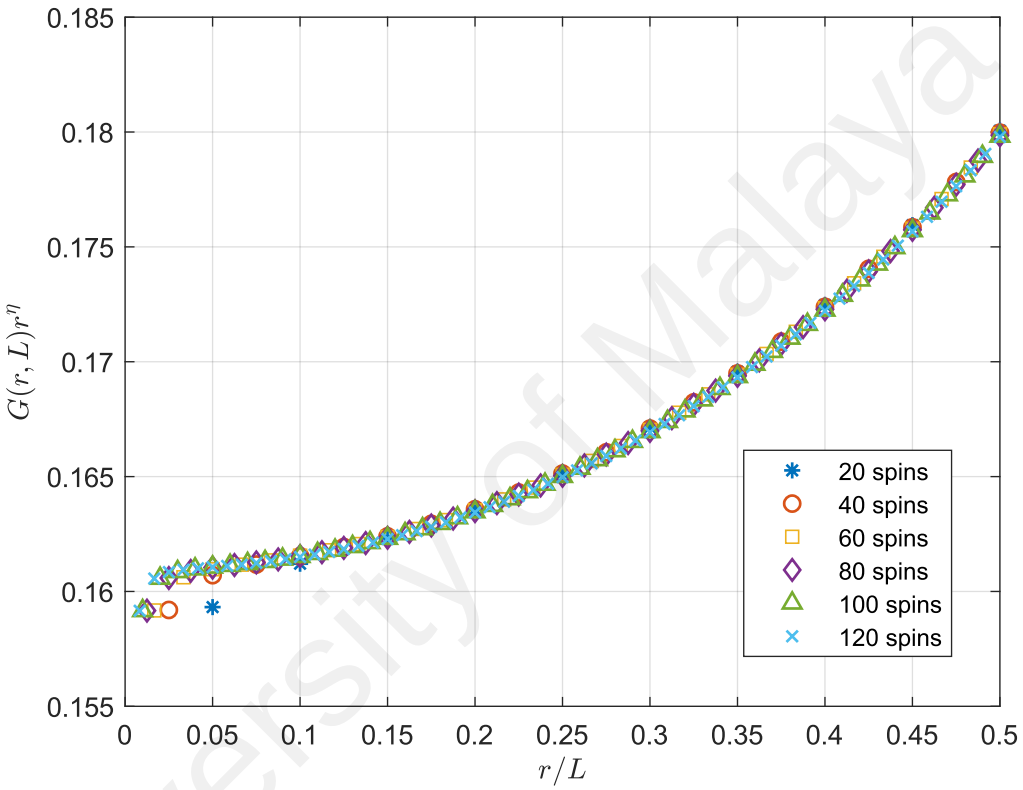

Figure 4.12: Graph of $G(r,L)|r|^{(d-2+\eta)}$ vs r/L for different system sizes with $\eta = 0.249$.

Note that in Figure 4.12 the plots start to deviate from a single graph when r/L is small. For the scaling ansatz (4.10) to be valid, the correlation function must be in power law. However, the power-law is only valid for large r. Therefore, the plots deviate at small distances. In conclusion, we determined that $\eta = 0.249(1)$.

The critical exponents we obtained obey the following scaling relations:

$$\gamma = \nu(2-\eta) \tag{4.11}$$

and

$$2\beta + \gamma = \nu(d + z) \tag{4.12}$$

Relation (4.12) is the hyperscaling relation. It is particularly significant because the correct theory of phase transition below the critical dimension of the mean-field theory must obey (4.12). From our results, we can see the critical exponents calculated conforms with these relations. As the exponents are each found independently, we showed that the finite-size scaling and matrix product states formalism can be used to study the critical dynamics of 1D Ising-like models.

4.3 Effect of Noisy Coupling Strength on Thermodynamic Parameters

The *d*-dimensional quantum Ising model is closely related to the *d+1*-dimensional classical Ising model. In the limit of zero temperature ($T \to 0$), the partition function of *d*-dimensional tQIM can be converted to the partition function of *d+1*-dimensional CIM. Therefore, at the theoretical absolute zero temperature, the *d*-dimensional tQIM is in the same universality class as *d+1*-dimensional CIM. Similar classical-quantum correspondence is also suspected between classical and quantum spin glasses (Sondhi, 1997; Chakrabarti, 1981; Dos Santos, 1985). Kryzhanovsky et. al. (2018) studied 2D classical Ising model with noisy interactions to investigate temperature sensitivity of free energy optimization learning algorithms for different noise levels. They observe qualitative changes to the behaviours of thermodynamic parameters with different noise levels and a regime change after a certain threshold noise level. Knowing the close relationship between *d+1*-dimensional classical systems and corresponding *d*-dimensional quantum systems, we are interested to investigate how adding noise to the couplings of 1D tQIM will affect its thermodynamic behaviour.

The Hamiltonian of 1D tQIM is generalized by introducing site dependant coupling strength J_i, where $J_i = 1 + \varepsilon_i$ and $\varepsilon_i = [-\zeta, \zeta]$ is a uniformly distributed noise with mean zero and amplitude ζ. As a result, the Hamiltonian becomes:

$$H = -\sum_{i=1}^{L-1} J_i S_i^z S_{i+1}^z - h \sum_{j=1}^{L} S_j^x \quad (4.13)$$

Now, the system with random nearest neighbour couplings is quenched disordered for each different realization. For each transverse field h, 100 different realizations are simulated and the disorder averages of thermodynamic quantities are calculated. By increasing ζ, some behavioural change to the averaged thermodynamic quantities is expected.

The thermodynamic quantities such as ground state energy, transverse and longitudinal magnetizations, and the variance of longitudinal magnetization, which corresponds to the magnetic susceptibility, are calculated for noise level $\zeta = 0.0$, 0.5, 1.0, 1.5 and 2.0. In addition, the Edward-Anderson order parameter for spin glass is also calculated. The results are plotted in Figure 4.13 – 4.18. For Figure 4.13 – 4.16, the analytic solution is plotted as a reference for departure from the noiseless case.

The ground state energy of a pure (noiseless) tQIM decreases monotonically with increasing quantum fluctuation (transverse field) and is non-analytic at the critical point ($h_c = 0.5$) (Pfeuty, 1970). The region before and after the critical point exhibit different functional behaviour. For the transverse field greater than the critical point, the energy decreases linearly with increasing transverse field as the spins are all already aligned in the transverse direction. The linear decrease of energy corresponds to the linear increase of the transverse field. When noise is introduced to the coupling, we observe that the energies decrease or equivalently the magnitudes of the energies increase with increasing noise. The plots are still following similar behaviour of pure tQIM except with an additional fluctuation in the plot. However, the plot in general still preserves distinct non-

linear and linear behaviour before and after the critical point, respectively. Note that for $\zeta > 1.0$ and particularly obvious for $\zeta = 2.0$, fluctuations before the critical point is bigger compared to after the critical point. As the fluctuations introduced only affect the z-component of the spin polarization, the observation is reasonable. The dominant eigenstate before the critical point is the ferromagnetic state $|\Phi_z\rangle$ so the ground state energies are more affected by the fluctuation, while $|\Phi_z\rangle$ is less dominant after the critical point so it is less affected.

While the ground state energies show expected behaviour, the transverse magnetizations $\langle M_x \rangle$, however, does not (see Figure 4.14). One expects the behaviour of any thermodynamic quantities to gradually deviate monotonically from pure tQIM as ζ increases. However, we observe that before and after the critical point, $\langle M_x \rangle$ exhibits different behaviours. Zooming into a different region of the plot (see Figure 4.15), we see that after the critical point, $\langle M_x \rangle$ decreases as ζ increases. This is reasonable as the noise disturbs the ordering of the spins in the transverse direction. However, before the critical point, $\langle M_x \rangle$ increases as ζ increases but decreases when $\zeta = 2.0$. The transverse field introduces quantum fluctuations which destroy the long-range order formed by the couplings. However, in this case, ζ also introduces fluctuations which only disturbs the long-range order. It does not align the spins in x-direction but instead assists the transverse field to increase $\langle M_x \rangle$. This in effect amplifies the quantum fluctuations for constant transverse field reading. If the noise is too great the fluctuations do not assist the effect of the transverse field. There is an optimum ζ that maximizes this effect in the range of $1.0 < \zeta < 2.0$.

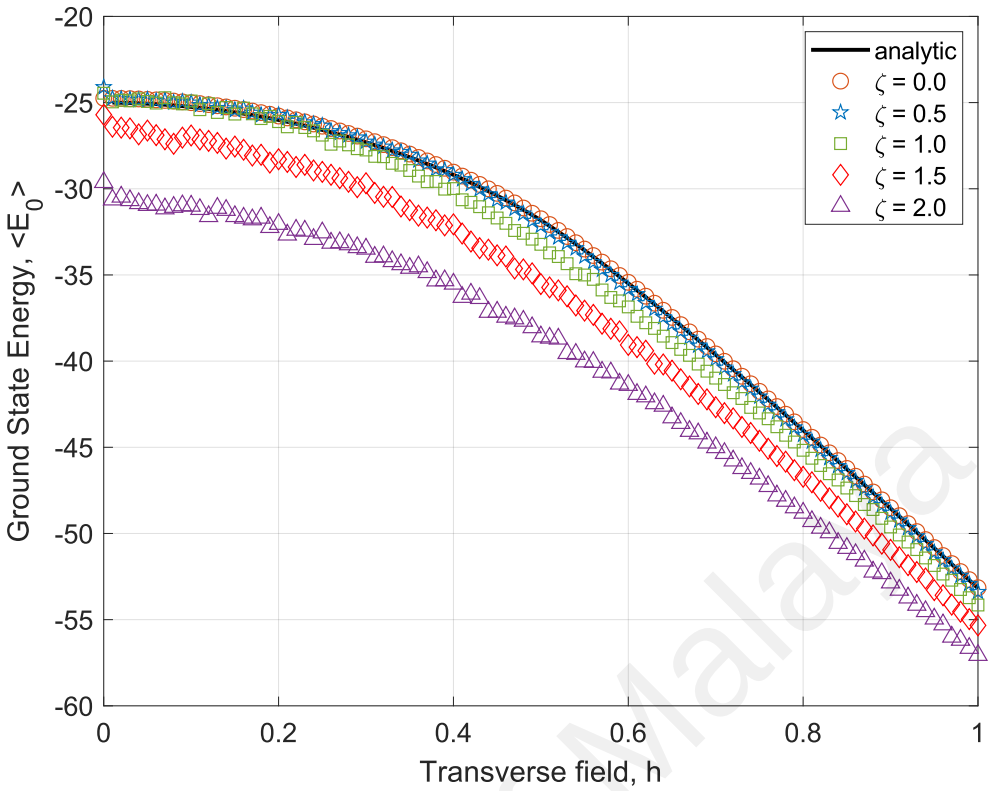

Figure 4.13: Ground state energy, $\langle E_0 \rangle$ vs transverse field, h with increasing noise level.

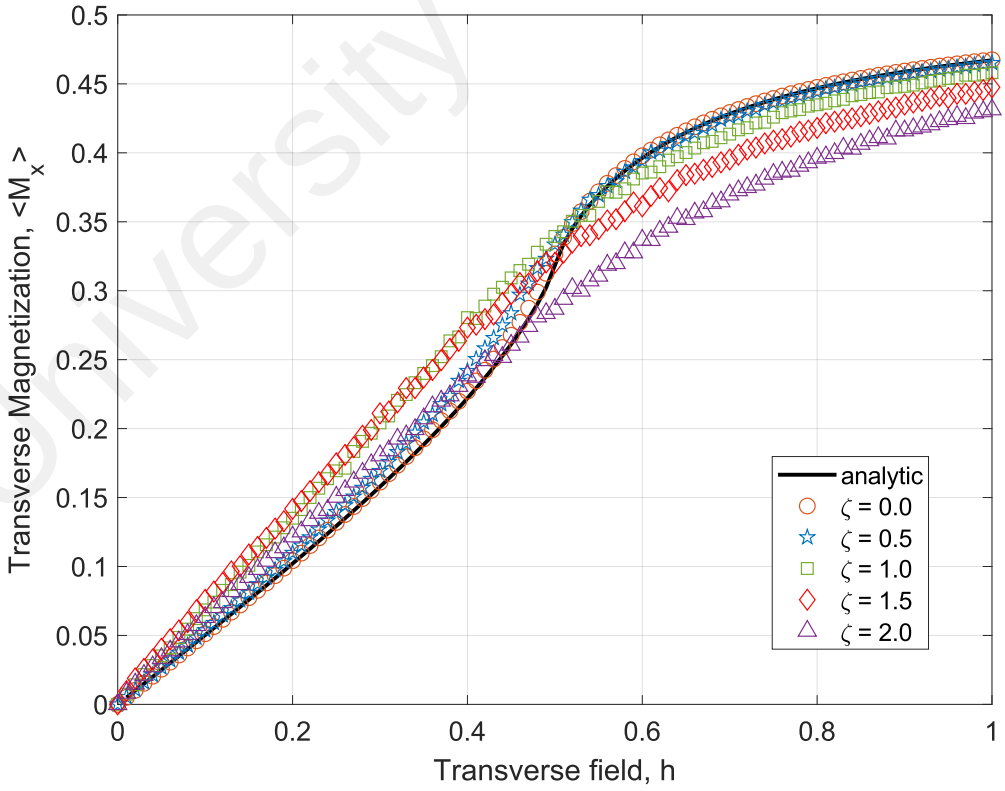

Figure 4.14: Transverse magnetization, $\langle M_x \rangle$ vs transverse field, h with increasing noise level.

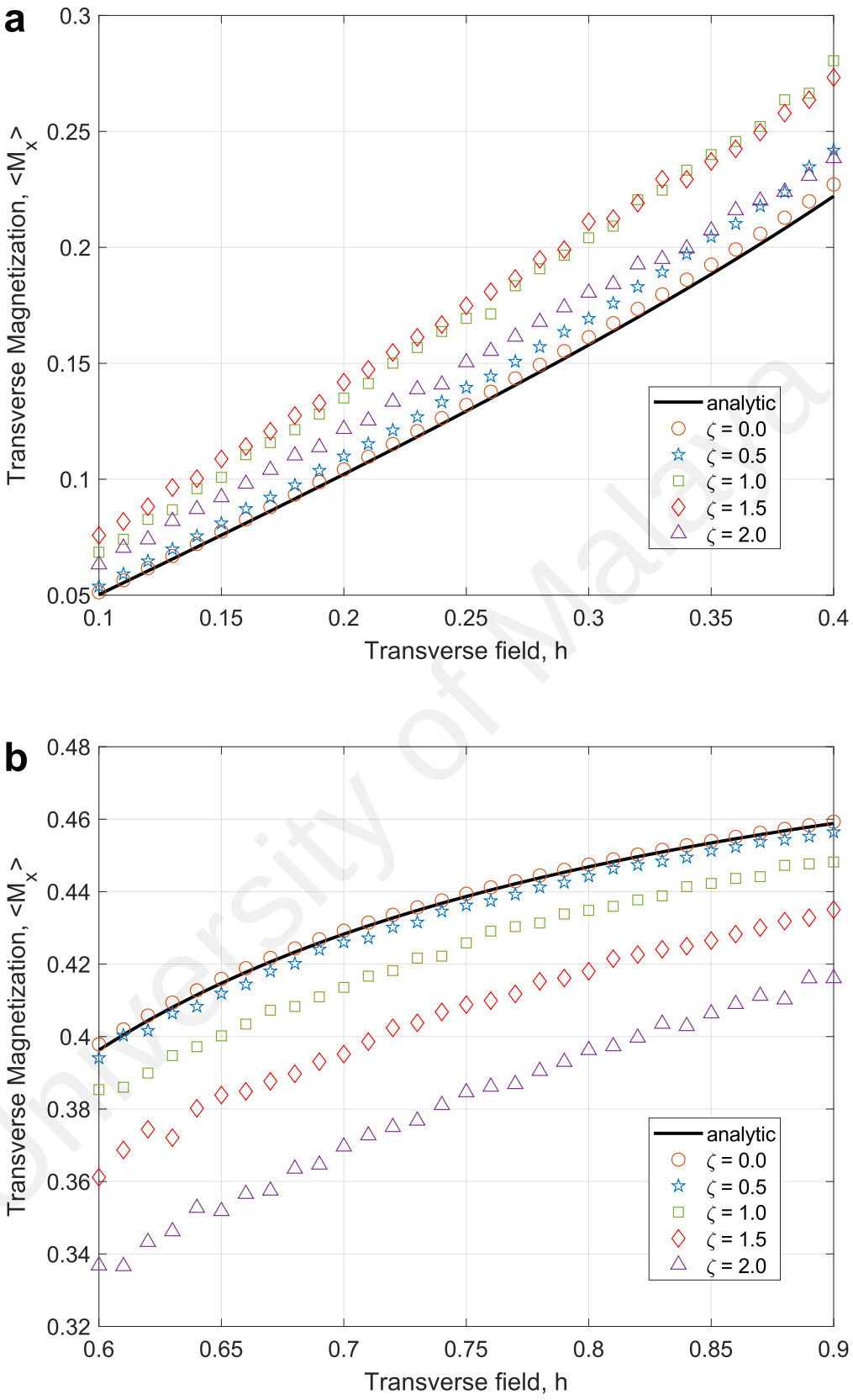

Figure 4.15: Transverse magnetization, $\langle M_x \rangle$ vs transverse field, h with increasing noise level: a) $0.1 < h < 0.4$ b) $0.6 < h < 0.9$.

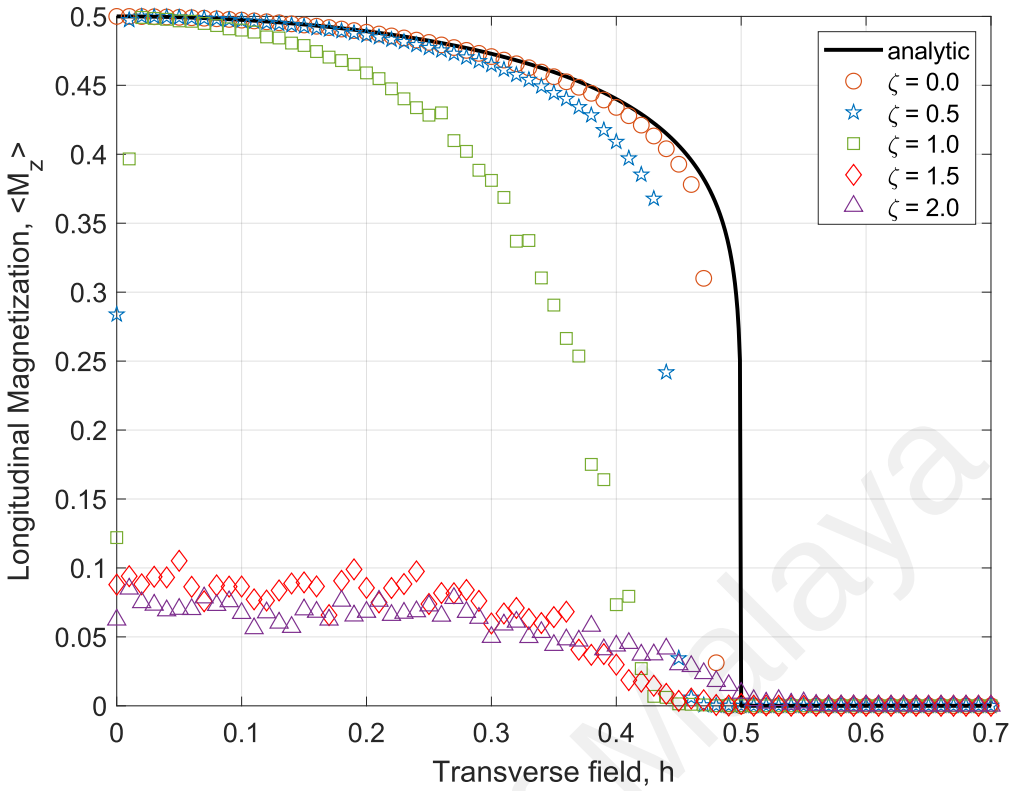

Figure 4.16: Longitudinal magnetization, $\langle M_z \rangle$ vs transverse field, h with increasing noise level. The plot is shown until $h = 0.7$ only because $\langle M_z \rangle = 0$ for $h > 0.7$.

Next, the longitudinal magnetization $\langle M_z \rangle$ which is the order parameter for tQIM. Referring to Figure 4.16, there are two distinct deviations in the region before the critical point. Note that for h close to zero $\langle M_z \rangle$ drops sharply while for h close to the critical point $\langle M_z \rangle$ deviates gradually with increasing noise. Up until $\zeta \sim 1.0$, $\langle M_z \rangle$ has a profile with a peak with a steep decrease at the left and smooth gradual behaviour at the right. When $\zeta > 1.0$, the profile is lost to intense fluctuations ($\zeta = 1.5$ & 2.0) as seen in Figure 4.16. The left deviation is due to competition between the transverse term and fluctuating term. For very small h, the fluctuating term dominates and destroys the order of the system. For h close to the critical point, the fluctuating terms assist the system towards phase transition. Thus $\langle M_z \rangle$ deviates and decreases to zero sooner than pure tQIM. From Figure 4.16 we observe that as ζ increases, $\langle M_z \rangle$ goes to zero at a smaller transverse field. However, when $\zeta = 2.0$ $\langle M_z \rangle$ falls to zero at $h \sim 0.5$ which is close to the critical point.

This supports our speculation that there is an optimum noise level which assists the system towards phase transition. We tried to locate where does the unimodal profile lost to fluctuation occurs and traced it to be roughly at $\zeta \sim 1.05$.

By comparing the average over 10 disordered realizations with 100, we observe that the fluctuations for $\langle E_0 \rangle$, $\langle M_x \rangle$ and $\langle M_z \rangle$ in general, are smaller with a bigger number of realizations. For $\zeta = 1.5$ & 2.0, we observe that the fluctuations of $\langle M_z \rangle$ before the critical point is smaller for 100 realizations as compared to 10 realizations. This agrees with the spin glass theory that $\langle M_z \rangle = 0$ for all transverse fields in the thermodynamic limit. With a larger and increasing number of realizations, we expect the $\langle M_z \rangle$ fluctuations for $\zeta = 1.5$ & 2.0 to subside and $\langle M_z \rangle$ goes to zero. This observation also suggests that $\langle M_z \rangle$ is not a proper order parameter for $\zeta \gg 1.0$.

The variance of longitudinal magnetization, $\mathrm{Var}(M_z)$ is proportional to the magnetic susceptibility per spin:

$$\mathrm{Var}(M_z) \propto \chi / L \tag{4.14}$$

The peak of χ is another parameter used to determine the critical point of the system. From Figure 4.17 we see that 100 spins tQIM has pseudo-critical point at $h_c = 0.49$. As the noise increases, the peak also decreases and shifts to the left. This supports our earlier argument that fluctuation in coupling will assist the spin of the system towards aligning in the transverse direction. This "speeds up" the phase transition with a lower critical field, h_c. However, there seems to have no apparent peak when $\zeta > 1$. This is consistent with the previous observation that for $\zeta \gg 1.0$, $\langle M_z \rangle$ and its moments are not good parameters to study its phase transition.

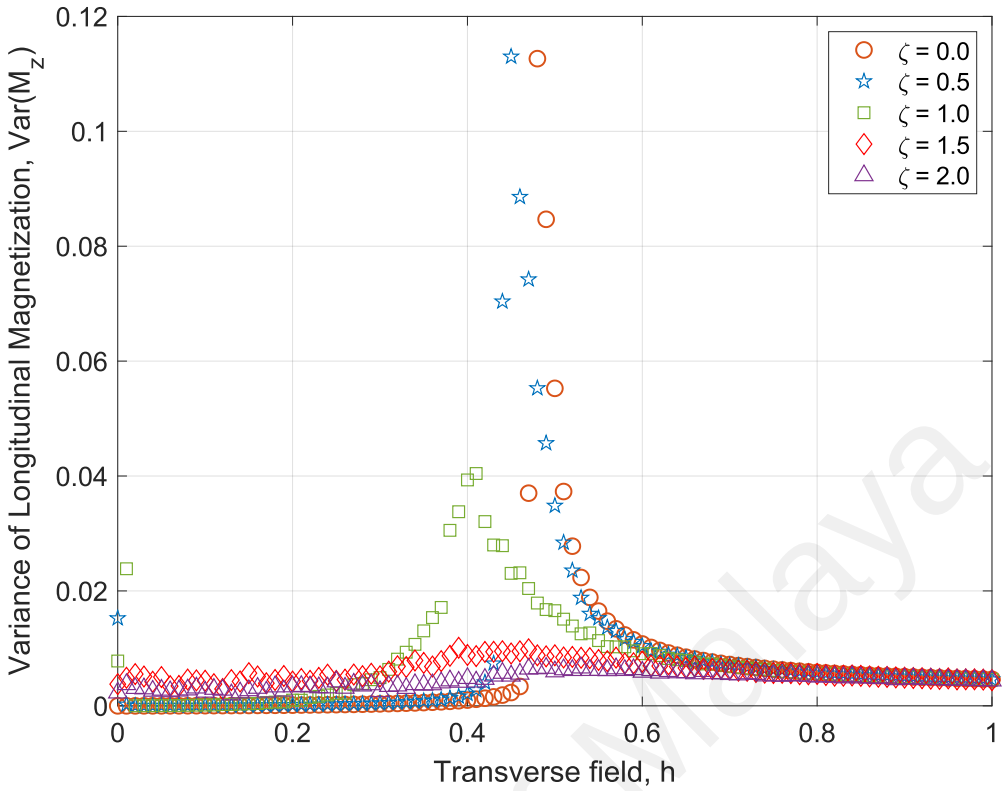

Figure 4.17: Variance of longitudinal magnetization, $\mathrm{Var}(M_z)$ vs transverse field, h with increasing noise level.

We calculated the Edward-Anderson order parameter q, which is defined for spin glass systems (Young, 1990):

$$q = \left[\frac{1}{L}\sum_{i=1}^{L}\langle\sigma_i\rangle^2\right]_{\mathrm{av}} \tag{4.15}$$

where $[\ldots]_{\mathrm{av}}$ is the disordered average over 100 realizations. q has consistent plots for all noise amplitudes and less fluctuations overall (see Figure 4.18). It is a better order parameter compared to $\langle M_z\rangle$. q validates previous observations where increasing ζ assists the phase transition. For $\zeta \leq 1.5$ q drops to zero sooner than the noiseless case. For $\zeta = 2.0$ q, instead, drops to zero later at $h{\sim}0.5$. These observations are consistent with the previous one but with a much less fluctuating order parameter. Systems with a smaller size of 60 spins are simulated to test for finite-size effects of the noise. There is no obvious deviation from the behaviour of 100 spins chain. In addition, we replaced uniformly distributed noise with normally distributed noise. As normal distribution is

more concentrated about the mean and has extreme value beyond the standard deviation, there are observable differences in the functional behaviour of thermodynamic quantities. However, the qualitative behaviour remains the same.

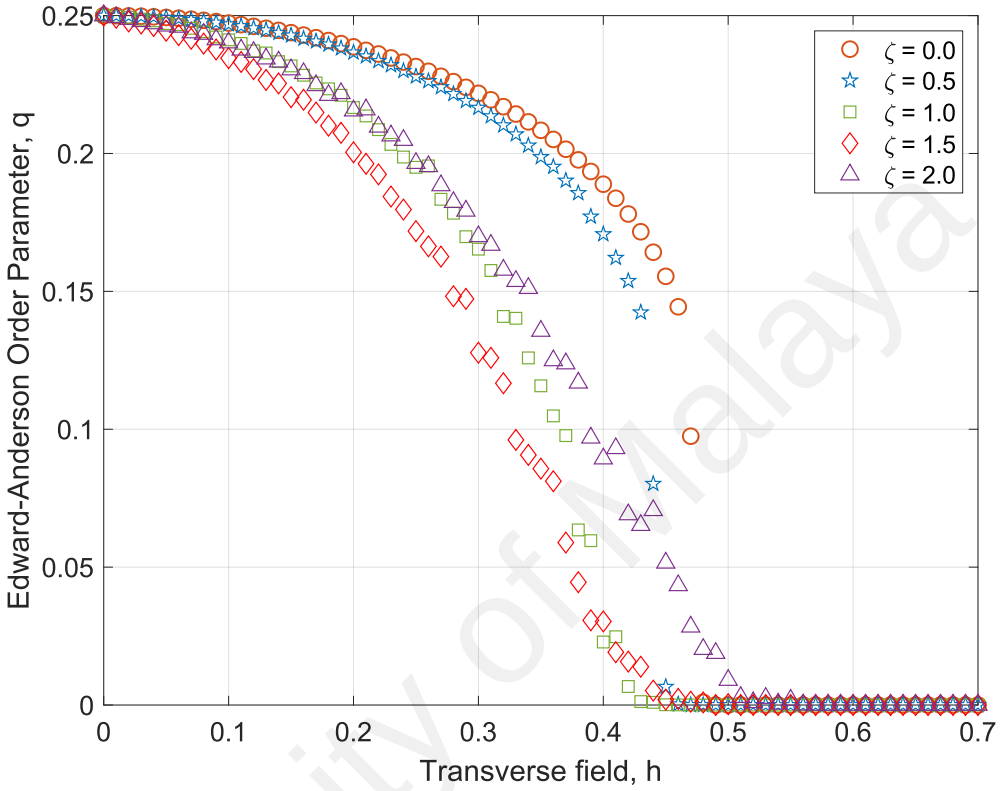

Figure 4.18: Edward-Anderson Order Parameter, q vs transverse field, h with increasing noise level.

Finally, a general conclusion can be drawn from the above observations. For noise level between $\zeta = 1.0$ and $\zeta = 1.5$, the tunnelling effects introduced by the transverse field before the critical point is amplified and assists the system towards phase transition. This suggests introducing noise with certain amplitudes to the couplings may improve the performance of quantum annealing. Future work can be done on more general graph topologies and non-uniform initial couplings.

CHAPTER 5: CONCLUSION

In this work, the one-dimensional transverse field quantum Ising model (tQIM) is simulated and studied. In order to study its thermodynamic properties, thermodynamic quantities are calculated using techniques in the tensor network formalism. The quantum wavefunction is cast in the form of Matrix Product States (MPS) and the ground state wavefunction is obtained via the Density Matrix Renormalization Group (DMRG) algorithm. The quantities of interest are obtained by tensor network contraction of the ground state Matrix Product States and corresponding quantum operators in the form of Matrix Product Operators (MPO).

5.1 Summary

Conventionally, numerical studies such as Monte Carlo simulations (Binder, 1990; Landau, 1990) and phenomenological renormalization group methods (Nightingale, 1990) studies the phase transition without directly obtaining the analytic solutions or the quantum wavefunction. Using the MPS as a variational wavefunction ansatz with built-in approximation structure, the ground state wavefunction, albeit not exact, of short-ranged interacting quantum Ising model is obtained in the MPS form. Thermodynamic quantities such as the ground state energy, transverse and longitudinal magnetizations, magnetic susceptibility and correlation function are calculated for various system sizes of 20, 40, 60, 80, 100 and 120 spins. Among these quantities, the longitudinal magnetization and its magnetic susceptibility and the correlation functions are selected to apply the finite-size scaling ansatz in order to obtain the critical exponents β, γ, and η. The values determined are $\beta/\nu = 0.1235(1)$, $\gamma/\nu = 1.7351(2)$, and $\eta = 0.249(1)$ which conform with the theoretical value from the analytic solution of 1D quantum Ising model. This also verifies that 1D quantum Ising model is in same universality class as 2D classical Ising model. They also fulfil the hyperscaling relation which is obeyed by systems below

their upper critical dimension. Given the critical exponents are independently calculated and fulfil the hyperscaling relation, the Matrix Product States formalism and finite-size scaling ansatz combined can reliably study the critical dynamics of one-dimensional quantum Ising-like models below upper critical dimension.

Next, with the addition of noise to the uniform nearest-neighbour coupling strength of the 1D tQIM, the system is found to transit from an ordered to a disordered system after a certain noise level. The study is mainly done by introducing uniformly distributed noise with amplitude ζ ranging from $\zeta = 0.5, 1.0, 1.5,$ and 2.0. The order-disorder transition happens at $\zeta \sim 1.0$ because the Hamiltonian is frustrated for $\zeta > 1.0$. In the ordered state, the thermodynamic quantities preserve the behaviour of pure tQIM albeit increasing deviation with noise. We find that for $\zeta \lesssim 1.5$ the noise assists the system towards phase transition. However, this feature is lost for $\zeta = 2.0$. For the disordered state, the quantities are highly fluctuating and do not exhibit any clear functional behaviour. In addition, we calculated the Edward-Anderson order parameter q and found it to be much less fluctuating and better characterize the system as an order parameter. In addition, no qualitative change of behaviour is observed for smaller size system and normally distributed noise. For noise level at $\zeta = 1.0$ and 1.5, the tunnelling effect introduced by the transverse field before the critical point is amplified and assists the system towards phase transition. This suggests introducing noise within a range of amplitudes to the couplings may improve the performance of quantum annealing.

5.2 Suggestion for Future Work

In the first part of the work, to obtain the critical exponents of the ideal quantum Ising model, the periodic boundary condition is imposed on the system. This eliminates the edge effects so that purely finite-size effects remain. In the future, the work can be extended to higher dimensions such as 2D or 3D. However, one needs to utilize higher-

dimensional tensor networks such as the Projected Entangled Pair States (PEPS) with different ground state searching algorithm and tensor contraction techniques. Besides the finite-size and edge effects, the corner effects can be studied on these higher dimensional systems. In the second part of the work, the effect of noise can be investigated in more realistic situations such as on general graph topologies (Rodríguez-Laguna, 2007) and non-uniform couplings.

Lastly, we propose to use the 1D tQIM and MPS formalism to study the water-ice phase transition of single-file water in nanopore. When confined to one-dimensional structure, the water molecules have effective short-ranged interactions (Köfinger & Dellago, 2010). Narrower diameter of the nanopore seems to introduce order to the water molecules to form "ice phase" (Koga et. al., 2001; Maniwa et. al., 2002). By replacing the spin variables with occupancy of water molecule in the nanopore, the 1D tQIM can study the water-ice phase transition with the transverse field inversely related to the nanopore diameter. Experimentally the nanopore diameter is not a tuneable parameter. Thus, this model can provide a theoretical study on how continuously adjusting the diameter affects the phase diagram of the transition.

REFERENCES

Affleck, I., Kennedy, T., Lieb, E. H., & Takasi, H. (1987). Rigorous results on valence-bond ground states in antiferromagnets. *Physical Review Letters*, *59*(7), 799-802.

Anderson, P. W. (1987). The resonating valence bond state in La_2CuO_4 and superconductivity. *Science*, *235*(4793), 1196-1198.

Bardeen, J., Cooper, L. & Schriffer, J. R. (1957). Theory of Superconductivity. *Physical Review*, *108*(5), 1175-1204.

Bethe, H. A. (1935). Statistical theory of superlattices. *Proceedings of the Royal Society of London. Series A, Mathematical and Physical Sciences*, *150*(871), 552-575.

Binder, K. (1990). Some recent progress in the phenomenological theory of finite size scaling and application to Monte Carlo studies of critical phenomena. In Privman, V. (Ed.) *Finite size scaling and numerical simulation of statistical systems*, (pp. 173-219). Singapore: World Scientific Publishing.

Bogoliubov, N. N. (1947). On the theory of superfluidity. *Izvestiya Akademii Nauk USSR*, *11*, 77-90. *Journal of Physics*, *11*, 23-32.

Bragg, W. L., & Williams, E. J. (1934). The effect of thermal agitation on atomic arrangement in alloys. *Proceedings of the Royal Society A: Mathematical, Physical and Engineering Sciences*, *145*(855), 699–730.

Calabrese, P., & Cardy, J. (2006). Time dependence of correlation functions following a quantum quench. *Physical Review Letter*, *96*(13), 136801, 1-4.

Chakrabarti, B. K. (1981). Critical behaviour of the Ising spin-glass models in a transverse field. *Physical Review B*, *24*(7), 4062-4064.

Cirac, J. I., Poilblanc, D., Schuch, N., & Verstraete, F. (2011). Entanglement spectrum and boundary theories with projected entangled-pair states. *Physical Review B*, *83*(24), 245134.

Davidson. E. R. (1975). The iterative calculation of a few of the lowest eigenvalues and corresponding eigenvectors of large real-symmetric matrices. *Journal of Computational Physics*, *17*(1), 87-94.

de Falco, D., & Tamascelli, D. (2011). An introduction to quantum annealing. *RAIRO-Theoretical Informatics and Applications*, *45*(1), 99-116.

De Gennes, P. G. (1963). Collective motions of hydrogen bonds. *Solid State Communications*, *1*(6), 132-137.

Demokritov, S. O., Demidov, V. E., Dzyapko, O., Melkov, G. A., Serga, A. A., Hillebrands, B., & Slavin, A. N. (2006). Bose–Einstein condensation of quasi-equilibrium magnons at room temperature under pumping. *Nature*, *443*(7110), 430-433.

Domb, C., & Hunter, D. L. (1965). On the critical behaviour of ferromagnets. *Proceedings of the Physical Society*, *86*(5), 1147-1151.

Dos Santos, R. R., dos Santos, R. Z., & Kischinhevsky, M. (1985). Transverse Ising spin-glass model. *Physical Review B*, *31*(7), 4694-4697.

Dreon, D., Sidorenkov, L. A., Bouazza, C., Maineult, W., Dalibard, J., & Nascimbene, S. (2017). Optical cooling and trapping of highly magnetic atoms: The benefits of a spontaneous spin polarization. *Journal of Physics B: Atomic, Molecular and Optical Physics*, *50*(6), 065005, 1-12.

Dutta, A., Aeppli, G., Chakrabarti, B. K., Divakaran, U., Rosenbaum, T. F., & Sen, D. (2015). *Quantum phase transitions in transverse field spin models: from statistical physics to quantum information*. Delhi, India: Cambridge University Press.

Eisert, J., Cramer, M., & Plenio, M. B. (2010). Colloquium: Area laws for the entanglement entropy. *Reviews of Modern Physics*, *82*(1), 277-306.

Elliott, R. J., Pfeuty, P., & Wood, C. (1970). Ising model with a transverse field. *Physical Review Letters*, *25*(7), 443-446.

Evenbly, G., & Vidal, G. (2013). Quantum criticality with the multi-scale entanglement renormalization ansatz. In Avella, A., & Mancini, F. (Eds.), *Strongly correlated systems* (pp. 99-130). Berlin, Heidelberg: Springer.

Farhi, E., Goldstone, J., Gutmann, S., & Sipser, M. (2000). Quantum computation by adiabatic evolution. arXiv:quant-ph/0001106. Retrieved on June 1, 2018 from https://arxiv.org/abs/quant-ph/0001106.

Farhi, E., Goldstone, J., Gutmann, S., Lapan, J., Lundgren, A., & Preda, D. (2001). A quantum adiabatic evolution algorithm applied to random instances of an NP-complete problem. *Science*, 292(5516), 472-475.

Fischer, K. H., & Hertz, J. A. (1993). *Spin glasses* (Vol. 1). Cambridge: Cambridge University Press.

Fisher, M. E. (1964). Correlation functions and the critical region of simple fluids. *Journal of Mathematical Physics*, *5*(7), 944-962.

Godoy, M., & Figueiredo, W. (2002). Critical behavior of the mixed-spin Ising model with two competing dynamics. *Physical Review E*, *65*(2), 026111, 1-8.

Gross, C., & Bloch, I. (2017). Quantum simulations with ultracold atoms in optical lattices. *Science*, *357*(6355), 995-1001.

Haegeman, J., Osborne, T. J., Verschelde, H., & Verstraete, F. (2013). Entanglement renormalization for quantum fields in real space. *Physical Review Letters*, *110*(10), 100402, 1-5.

Hasenbusch, M. (2008). The Binder cumulant at the Kosterlitz–Thouless transition. *Journal of Statistical Mechanics: Theory and Experiment*, *2008*(08), P08003, 1-21.

Inagaki, T., Haribara, Y., Igarashi, K., Sonobe, T., Tamate, S., Honjo, T., ... & Tadanaga, O. (2016). A coherent Ising machine for 2000-node optimization problems. *Science*, *354*(6312), 603-606.

Inoue, J. I. (2001). Application of the quantum spin glass theory to image restoration. *Physical Review E*, *63*(4), 046114, 1-10.

Ising, E. (1925). Report on the theory of ferromagnetism. *Zeitschrift fur Physik*, *31*, 253-258.

Jennings, D., Brockt, C., Haegeman, J., Osborne, T. J., & Verstraete, F. (2015). Continuum tensor network field states, path integral representations and spatial symmetries. *New Journal of Physics*, *17*(6), 063039, 1-22.

Jiang, H. C., Weng, Z. Y., & Xiang, T. (2008). Accurate determination of tensor network state of quantum lattice models in two dimensions. *Physical Review Letters*, *101*(9), 090603, 1-4.

Jouzdani, P., Novais, E., Tupitsyn, I. S., & Mucciolo, E. R. (2014). Fidelity threshold of the surface code beyond single-qubit error models. *Physical Review A*, *90*(4), 042315, 1-11.

Kadanoff, L. P. (1966). Scaling laws for Ising models near T_c. *Physics Physique Fizika*, *2*(6), 263-272.

Kadowaki, T., & Nishimori, H. (1998). Quantum annealing in the transverse Ising model. *Physical Review E*, *58*(5), 5355-5363.

Kaufman, B. (1949). Crystal Statistics. II. Partition function evaluated by spinor analysis. *Physical Review*, *76*(8), 1232-1243.

Kitaev, A. Y. (2003). Fault-tolerant quantum computation by anyons. *Annals of Physics*, *303*(1), 2-30.

Klaers, J., Schmitt, J., Vewinger, F., & Weitz, M. (2010). Bose–Einstein condensation of photons in an optical microcavity. *Nature*, *468*(7323), 545-548.

Köfinger, J., & Dellago, C. (2010). Single-file water as a one-dimensional Ising model. *New Journal of Physics*, *12*(9), 093044, 1-17.

Koga, K., Gao, G. T., Tanaka, H., & Zeng, X. C. (2001). Formation of ordered ice nanotubes inside carbon nanotubes. *Nature*, *412*(6849), 802-805.

Kramers, H. A., & Wannier, G. H. (1941). Statistics of the Two-Dimensional Ferromagnet. Part 1 & Part 2. *Physical Review*, *60*, 252-262, 263-276.

Kryzhanovsky, B., Malsagov, M., & Karandashev, I. (2018). Investigation of finite-size 2D Ising model with a noisy matrix of spin-spin interactions. *Entropy*, *20*(8), 585, 1-13.

La Rooij, A. L., van den Heuvell, H. V. L., & Spreeuw, R. J. C. (2019). Designs of magnetic atom-trap lattices for quantum simulation experiments. *Physical Review A*, *99*(2), 022303, 1-9.

Lanczos, C. (1950). An iteration method for the solution of the eigenvalue problem of linear differential and integral operators. *Journal of Research of the National Bureau of Standards*, *45*(4), 255-282.

Landau, D. P. (1990). Monte Carlo Studies OP Finite Size Effects at First and Second Order Phase Transitions. In Privman, V. (Ed.) *Finite size scaling and numerical simulation of statistical systems*, (pp. 223-260). Singapore: World Scientific Publishing.

Leggett, A. (1999). Superfluidity. *Reviews of Modern Physics*, *71*(2), S318–S323.

Li, Y., Hao, J., Liu, H., Li, Y., & Ma, Y. (2014). The metallization and superconductivity of dense hydrogen sulfide. *The Journal of Chemical Physics*, *140*(17), 174712, 1-7.

Lieb, E., Schultz, T., & Mattis, D. (1961). Two soluble models of an antiferromagnetic chain. *Annals of Physics*, *16*(3), 407-466.

Linder, J., & Robinson, J. W. A. (2015). Superconducting spintronics. *Nature Physics*, *11*(4), 307–315.

Maniwa, Y., Kataura, H., Abe, M., Suzuki, S., Achiba, Y., Kira, H., & Matsuda, K. (2002). Phase transition in confined water inside carbon nanotubes. *Journal of the Physical Society of Japan*, *71*(12), 2863-2866.

McMahon, P. L., Marandi, A., Haribara, Y., Hamerly, R., Langrock, C., Tamate, S., ... & Byer, R. L. (2016). A fully programmable 100-spin coherent Ising machine with all-to-all connections. *Science*, *354*(6312), 614-617.

Merdan, Z., & Erdem, R. (2004). The finite-size scaling study of the specific heat and the Binder parameter for the six-dimensional Ising model. *Physics Letters A*, *330*(6), 403-407.

Misguich, G., & Lhuillier, C. (2005). *Frustrated Spin Systems* (Diep, H.T., Ed.). Singapore, Hackensack, N.J.: World Scientific.

Newell, F. G., & Montroll, W. E. (1953). On the theory of the Ising model of ferromagnetism. *Reviews of Modern Physics*, *25*(2), 353-389.

Nightingale, M. P. (1990). Transfer matrices, phase transitions, and critical phenomena: Numerical methods and applications. In Privman, V. (Ed.) *Finite size scaling and numerical simulation of statistical systems*, (pp. 287-351). Singapore: World Scientific Publishing.

Onsager, L. (1944). Crystal Statistics. I. A Two-Dimensional Model with an Order-Disorder Transition. *Physical Review*, *65*(3-4), 117-149.

Ornstein, L. S., & Zernike, F. (1914). Integral equation in liquid state theory. *Proceedings of the Royal Netherlands Academy of Arts and Sciences, Amsterdam*, *17*, 793-806.

Orús, R. (2014). A practical introduction to tensor networks: Matrix product states and projected entangled pair states. *Annals of Physics*, *349*, 117-158.

Orús, R. (2019). Tensor networks for complex quantum systems. *Nature Reviews Physics*, 1-13.

Paige, C. C. (1971). *The computation of eigenvalues and eigenvectors of very large sparse matrices* (Doctoral dissertation, University of London). Retrieved on June 1, 2018 from https://pdfs.semanticscholar.org/48ed/e1ea2ad4a079c3d7386e97b6635c58544170.pdf

Paige, C. C. (1972). Computational Variants of the Lanczos Method for the Eigenproblem. *IMA Journal of Applied Mathematics*, *10*(3), 373–381.

Peierls, R. (1936). On Ising's model of ferromagnetism. *Mathematical Proceedings of the Cambridge Philosophical Society*, *32*(3), 477-481.

Pfeuty, P. (1970). The one-dimensional Ising model with a transverse field. *Annals of Physics*, *57*(1), 79-90.

Rodríguez-Laguna, J. (2007). Density matrix renormalization on random graphs and the quantum spin-glass transition. *Journal of Physics A: Mathematical and Theoretical*, *40*(40), 12043-12054.

Rossini, D., Silva, A., Mussardo, G., & Santoro, G.E. (2009). Effective thermal dynamics following a quantum quench in a spin chain. *Physical Review Letter*, *102*(12), 127204, 1-4.

Sachdev, S. (2011). *Quantum phase transitions*. New York: Cambridge University Press.

Savary, L., & Balents, L. (2017). Quantum spin liquids: A review. *Reports on Progress in Physics*, *80*(1), 016502, 1-55.

Schollwöck, U. (2005). The density-matrix renormalization group. *Reviews of Modern Physics*, *77*(1), 259-315.

Schollwöck, U. (2011). The density-matrix renormalization group in the age of matrix product states. *Annals of Physics*, *326*(1), 96-192.

Schuch, N., Wolf, M. M., Verstraete, F., & Cirac, J. I. (2007). Computational complexity of projected entangled pair states. *Physical Review Letters*, *98*(14), 140506, 1-4.

Sengupta, K., Powell, S., & Sachdev, S. (2004). Quench dynamics across quantum critical points. *Physical Review A*, *69*(5), 053616, 1-10.

Senthil, T., Balents, L., Sachdev, S., Vishwanath, A., & Fisher, M. P. A. (2004). Quantum criticality beyond the Landau-Ginzburg-Wilson paradigm. *Physical Review B*, *70*(14), 144407, 1-33.

Senthil, T., Vishwanath, A., Balents, L., Sachdev, S., & Fisher, M. P. A. (2004). Deconfined quantum critical points. *Science*, *303*(5663), 1490-1494.

Shi, Y. Y., Duan, L. M., & Vidal, G. (2006). Classical simulation of quantum many-body systems with a tree tensor network. *Physical Review A*, *74*(2), 022320, 1-4.

Silvi, P., Giovannetti, V., Montangero, S., Rizzi, M., Cirac, J. I., & Fazio, R. (2010). Homogeneous binary trees as ground states of quantum critical Hamiltonians. *Physical Review A*, *81*(6), 062335, 1-6.

Sondhi, S. L., Girvin, S. M., Carini, J. P., & Shahar, D. (1997). Continuous quantum phase transitions. *Reviews of Modern Physics*, *69*(1), 315-333.

Srednicki, M. (1993). Entropy and area. *Physical Review Letters*, *71*(5), 666-669.

Stanley, H. E. (1971). Exponent Inequalities. In *Introduction to phase transitions and critical phenomena*, (pp. 53-66). Oxford: Oxford University Press.

Strecka, J., & Jascur, M. (2015). A brief account of the Ising and Ising-like models: Mean-field, effective-field and exact results. *Acta Physica Solvaca*, *65*(4), 235-367.

Suzuki, S., Inoue, J. I., & Chakrabarti, B. K. (2012). *Quantum Ising phases and transitions in transverse Ising models* (Vol. 862) (2nd ed.). Berlin, Heidelberg: Springer-Verlag.

Swingle, B. (2012). Entanglement renormalization and holography. *Physical Review D*, *86*(6), 065007, 1-8.

Tagliacozzo, L., Evenbly, G., & Vidal, G. (2009). Simulation of two-dimensional quantum systems using a tree tensor network that exploits the entropic area law. *Physical Review B*, *80*(23), 235127, 1-17.

Venturelli, D., Mandra, S., Knysh, S., O'Gorman, B., Biswas, R., & Smelyanskiy, V. (2015). Quantum optimization of fully connected spin glasses. *Physical Review X*, *5*(3), 031040, 1-8.

White, S. R., & Noack, R. M. (1992). Real-space quantum renormalization groups. *Physical Review Letters*, *68*(24), 3487-3490.

White, S. R. (1992). Density matrix formulation for quantum renormalization groups. *Physical Review Letters*, *69*(19), 2863-2866.

White, S. R. (1993). Density-matrix algorithms for quantum renormalization groups. *Physical Review B*, *48*(14), 10345-10356.

Widom, B. (1965). Surface tension and molecular correlations near the critical point. *The Journal of Chemical Physics*, *43*(11), 3892-3897.

Widom, B. (1965). Equation of state in the neighborhood of the critical point. *The Journal of Chemical Physics*, *43*(11), 3898-3905.

Williams, E. J. (1935). The effect of thermal agitation on atomic arrangement in alloys. III. *Proceedings of the Royal Society A: Mathematical, Physical and Engineering Sciences*, *152*(875), 231–252.

Wilson, K. G. (1971). Renormalization group and critical phenomena. I. Renormalization group and the Kadanoff scaling picture. *Physical Review B*, *4*(9), 3174-3183.

Wilson, K. G. (1975). The renormalization group: Critical phenomena and the Kondo problem. *Reviews of Modern Physics*, *47*(4), 773-840.

Verstraete, F., & Cirac, J. I. (2006). Matrix product states represent ground states faithfully. *Physical Review B*, *73*(9), 094423, 1-8.

Verstraete, F., Wolf, M. M., Perez-Garcia, D., & Cirac, J. I. (2006). Criticality, the area law, and the computational power of projected entangled pair states. *Physical Review Letters*, *96*(22), 220601, 1-4.

Verstraete, F., & Cirac, J. I. (2010). Continuous matrix product states for quantum fields. *Physical Review Letters*, *104*(19), 190405, 1-4.

Vidal, G., Latorre, J. I., Rico, E., & Kitaev, A. (2003). Entanglement in quantum critical phenomena. *Physical Review Letters*, *90*(22), 227902, 1-4.

Vidal, G. (2007). Entanglement renormalization. *Physical Review Letters*, *99*(22), 220405, 1-4.

Wen, X. G. (2004). *Quantum field theory of many-body systems: from the origin of sound to an origin of light and electrons*. New York: Oxford University Press.

Young, A. P. (1990). Simulations of Spin Glass Systems. In Privman, V. (Ed.) *Finite size scaling and numerical simulation of statistical systems*, (pp. 466-488). Singapore: World Scientific Publishing.

Zhang, X., Hu, G., Zhang, Y., Li, X., & Chen, X. (2018). Finite-size scaling of correlation functions in finite systems. *Science China Physics, Mechanics & Astronomy*, *61*(12), 120511, 1-7.

LIST OF PUBLICATIONS

1. **Pang, S. Y.**, Muniandy, S. V., & Kamali, M. Z. M. (2019). Critical dynamics of transverse-field quantum Ising model using finite-size scaling and matrix product states. *International Journal of Theoretical Physics*, *58*(12), 4139-4151.

2. **Pang, S. Y.**, Muniandy, S. V., & Kamali, M. Z. M. (2020). Effect of fluctuation in the coupling strength on critical dynamics of 1D transverse field quantum Ising model. *International Journal of Theoretical Physics*, *59*(1), 250-260.